UC Berkeley
UC Berkeley Electronic Theses and Dissertations

Title
Bandgap Engineering of Zinc Oxide Sulfide and Gallium Oxide Sulfide Highly Mismatched Alloys

Permalink
https://escholarship.org/uc/item/8x6221jw

Author
Jaquez-Nunez, Maribel

Publication Date
2019

Peer reviewed|Thesis/dissertation

eScholarship.org Powered by the California Digital Library
University of California

Bandgap Engineering of Zinc Oxide Sulfide and Gallium Oxide Sulfide Highly Mismatched Alloys

By

Maribel Jaquez-Nunez

A dissertation submitted in partial satisfaction of the

requirements for the degree of

Doctor of Philosophy

in

Engineering– Mechanical Engineering

in the

Graduate Division

of the

University of California, Berkeley

Committee in charge:

Professor Chris Dames, Co-Chair
Dr. Wladyslaw Walukiewicz, Co-Chair
Professor Oscar D. Dubon
Professor Liwei Lin

Summer 2019

Bandgap Engineering of Zinc Oxide Sulfide and Gallium Oxide Sulfide Highly Mismatched Alloys

Copyright 2019
by
Maribel Jaquez-Nunez

Abstract

Bandgap Engineering of Zinc Oxide Sulfide and Gallium Oxide Sulfide Highly Mismatched Alloys
by

Maribel Jaquez-Nunez

Doctor of Philosophy in Mechanical Engineering

University of California, Berkeley

Professor Chris Dames, Co-Chair
Dr. Wladyslaw Walukiewicz, Co-Chair

Binary oxide materials exhibit a wide range of technologically relevant behaviors (i.e. magnetism, superconductivity, and ferroelectricity). For this reason, there is much interest in oxides due to their potential in applications ranging from batteries and solar cells to power electronics and more. Unfortunately, oxide materials are hindered by experimental and physical challenges such as sample growth, control of the bandgap, and doping —processes that are well understood and realized in traditional semiconductors (i.e., Si, Ge). Band structure engineering is one method that modifies semiconductor properties providing a means to control the performance of a wide range of electronic materials to meet device requirements.

Highly mismatched alloys are semiconductor alloys formed through isoelectronic substitution of anions with very different ion size and electronegativity, which allows drastic band structure modification with dilute alloy content. In this work, ZnO and Ga_2O_3 were alloyed with S to study the drastic band structure modification with alloy content.

Alloys from ZnO and ZnS were synthesized by radio-frequency magnetron sputtering and pulsed-laser deposition over the entire alloying range. Sputtering is a favorable deposition technique for an industrial production line due to better process integration with currently used methods. Pulsed-laser deposition is suitable for the growth of materials with large miscibility gaps arising from the large differences in atomic size and electronegativity due to the potential for both stoichiometric transfer of target materials to the substrate and the use of non-equilibrium growth conditions. Using X-ray diffraction, the $ZnO_{1-x}S_x$ films were found to be highly textured with a columnar-like structure that remains throughout the entire composition range (determined by transmission electron microscopy). The optical absorption edge of these alloys decreases rapidly with small amount of added sulfur ($x \sim 0.02$) and continues to red shift to a minimum of 2.6eV at $x=0.45$. At higher sulfur concentrations ($x > 0.45$), the absorption edge shows a continuous blue shift. The strong reduction in the bandgap for O-rich alloys is the result of the upward shift of the valence-band edge with x as observed by X-ray photoelectron spectroscopy. As a result, the room temperature bandgap of $ZnO_{1-x}S_x$ alloys can be tuned from 3.7 eV to 2.6 eV. The observed large bowing in the composition dependence of the energy bandgap arises from the anticrossing interactions between (1) the valence-band of ZnO and the localized sulfur level at 0.30 eV above

the ZnO valence-band maximum for O-rich alloys and (2) the conduction-band of ZnS and the localized oxygen level at 0.20 eV below the ZnS conduction-band minimum for the S-rich alloys. The ability to tune the bandgap and knowledge of the location of the valence and conduction-band can be advantageous in applications, such as heterojunction solar cells, where band alignment is crucial.

Stoichiometric gallium oxide sulfide $Ga_2(O_{1-x}S_x)_3$ thin-film alloys were synthesized by pulsed-laser deposition with $x \leq 0.35$. One challenge has been synthesizing $Ga_2(O,S)_3$ crystalline films, as these samples have been determined to be amorphous through X-ray diffraction and transmission electron microscopy measurements. Despite the amorphous structure, the films have a well-defined, room-temperature optical bandgap tunable from 5.0 eV down to 3.0 eV. Similar to the amorphous $GaN_{1-x}As_x$ system, the band structure behavior of amorphous $Ga_2(O,S)_3$ alloys is in agreement with the predictions of the band anticrossing model. In the case for amorphous $Ga_2(O,S)_3$ alloys, the addition of sulfur at a merely 0.013 ratio shows a reduction in bandgap of about 1 eV suggesting that the localized sulfur level is located roughly 1 eV above the valence band of Ga_2O_3, a value that is comparable to the sulfur level location found in $ZnO_{1-x}S_x$ alloys. The optical absorption data are interpreted using a modified valence-band anticrossing model that is applicable for highly mismatched alloys. The model provides a quantitative method to more accurately determine the bandgap as well as insight to how the band edges are changing with composition.

To My Parents

For their continued encouragement and support.

Table of Contents

Abstract.....1
Table of Contents ii
List of Figures.....iv
List of Tables vii
Acknowledgments..... viii
1 Introduction 1
1.1 Band Structure Engineering Through Alloying 2
1.2 Highly Mismatched Alloys 5
1.2.1 The Conduction Band Anticrossing Model 5
1.2.2 The Valence Band Anticrossing Model 6
1.3 Structure of the Dissertation.....8
2 $ZnO_{1-x}S_x$ Material Synthesis and Structural Analysis.....9
2.1 Sputtering Overview 10
2.1.1 RF Magnetron Sputtering Experimental Setup and Growth Parameters.....11
2.2 PLD Overview.....15
2.2.1 PLD Experimental Setup and Growth Parameters.....16
2.3 Thickness and Composition Characterization.....17
2.4 Structural Characterization.....18
2.4.1 X-Ray Diffraction 18
2.4.2 Transmission Electron Microscopy and Energy Dispersive X-Ray Spectroscopy 22
3 Optical and Electronic Properties of $ZnO_{1-x}S_x$ Films.....25
3.1 Optical Absorption Spectroscopy of $ZnO_{1-x}S_x$ Films.....25
3.1.1 Optical Absorption Properties of $ZnO_{1-x}S_x$.....26
3.2 Photomodulated Reflectance (PR) Spectroscopy 29
3.3 X-Ray Photoelectron Spectroscopy 31
3.3.1 Composition Calculation Using XPS 32
3.3.2 XPS of $ZnO_{1-x}S_x$ Films 33
3.4 Band Anticrossing in $ZnO_{1-x}S_x$.....37
3.4.1 Valence Band Anticrossing of $ZnO_{1-x}S_x$ Dilute Sulfur Films 38
3.4.2 Conduction Band Anticrossing of $ZnO_{1-x}S_x$ Dilute Oxygen Films.....40
3.4.3 Bandgap Dependence on Composition 42

3.5 $ZnO_{1-x}S_s$ as a Buffer Layer in CdTe Thin Film Solar Cells 45
3.5.1 Cell with $ZnO_{0.95}S_{0.05}$ Buffer Layer 48
3.5.2 Cell with $ZnO_{0.82}S_{0.18}$ Buffer Layer 49
3.5.3 Cell with $ZnO_{0.25}S_{0.75}$ Buffer Layer 50
3.5.4 Cell with $ZnO_{0.05}S_{0.90}$ Buffer Layer 51
3.5.5 Overall Cell Comparison 52
4 $Ga_2(O,S)_3$ Material Synthesis 54
4.1 Growth of β-Ga_2O_3 55
4.2 Growth of $Ga_2(O,S)_3$ 57
4.3 Band Anticrossing in $Ga_2(O_{1-x}S_x)_3$ 61
5 Conclusion and Future Work 69
5.1 $ZnO_{1-x}S$ Conclusions 69
5.1.1 Future Work 69
5.2 $Ga(O,S)_3$ Conclusions 70
5.2.1 Future Work 70
5.3 Overall Conclusions 71
Appendix A 72
A.1 Band Offsets of Various Semiconductors 72
References 74

List of Figures

Figure 1.1: (Left) CIGS thin film photovoltaic layer structure adopted from [6] and (Right) Flexible CIGS solar cell [7]. 2
Figure 1.2: Schematic dispersion relation of a direct versus that of an indirect bandgap semiconductor. 3
Figure 1.3: The conduction-band and valence-band edge locations relative to vacuum for ZnO, ZnS, Ga_2O_3 and Ga_2S_3 4
Figure 1.4: Bandgap of dilute As-rich and N-rich $GaN_{1-x}As_x$ alloys as a function of x. The solid line is the calculated bandgap of dilute $GaN_{1-x}As_x$ alloys based on the BAC model interpolated over the entire composition range. Bandgaps by VCA and by a forced quadratic fitting to the experimental gap energies using a single bowing parameter of b=16.2 eV are also shown. Adopted from [11]. 7
Figure 1.5: Bandgap dependence of $GaN_{1-x}As_x$ alloys with the BAC model [10]. 8
Figure 2.1: Simple DC sputtering geometry 11
Figure 2.2: Simple schematic of RF magnetron co-sputtering setup used to deposit $ZnO_{1-x}S_x$ alloys. 12
Figure 2.3: Image of RF magnetron co-sputtering setup used in this work. 13
Figure 2.4: Sample calibration plot that shows how to control the sulfur composition by modifying the ZnO target power during growth. The ZnO target-substrate distance was kept at 4cm, the ZnS target-substrate distance was kept at 4cm, the Ar flow rate was kept at 10 SCCM, the background growth pressure was kept at 5 mTorr, and the ZnS power was kept at 100W for all runs shown. 14
Figure 2.5: Sample calibration plot that shows how to control the sulfur composition by modifying the ZnS target power during growth. The ZnO target-substrate was kept at 4cm, the ZnS target-substrate was kept at 6cm, the Ar flow rate was kept at 10 SCCM, the background growth pressure was kept at 5 mTorr, and the ZnO power was kept at 120W for all runs shown. 15
Figure 2.6: Schematic of PLD deposition 16
Figure 2.7: RBS spectra with the SIMNRA simulation for sample R489 with 31%S. The red line is the RBS data and the blue line is the simulated fit using SIMNRA. 18
Figure 2.8: Gaussian fit of XRD 2 θ scan for sample R490 with 37%S. 19
Figure 2.9: Normalized XRD (0002) diffraction peak of $ZnO_{1-x}S_x$ alloys over nearly the entire composition range (x from 0 to 0.99). The composition listed on the diffraction peaks was found using Vegard's law. 20
Figure 2.10: Comparison between RBS and XRD calculated concentration of sulfur. 21
Figure 2.11: Pairs of Bright- and Dark-Field micrographs of the samples 1 to 4. (a)–(b) correspond to the sample with x=0.04 S content, (c)–(d) to the sample with x=0.44 S content, (e)–(f) to the sample with x=0.76 S content (g)–(h) to the sample with x=0.98 S content. A columnar-like structure is observed for the whole range of composition x of the synthesized $ZnO_{1-x}S_x$

layers with a considerable increasing of column size for the sample with an intermediate composition x = 0.44. Bar scales are 20 nm for (a)–(b) and 40 nm for (c)–(h). 23
Figure 2.12: EDX element mapping for the detected 3 elements, Zn, O, and S, respectively, columns 2 to 4, alongside with simultaneously acquired HAADF survey image. (a) correspond to the sample with x=0.04 S content, (b) to the sample with x=0.44 S content, (c) to the sample with x=0.76 S content, and (d) to the sample with x=0.98 S content. 24
Figure 3.1: Sample plot with linear extrapolation of $\alpha^2(E)$ used to determine the bandgap of a sample with x=0.87. 27
Figure 3.2: (a) Absorption spectra for select films with dilute sulfur in a ZnO matrix. The arrow indicates the direction the absorption edge shifts with the increase in sulfur content. (b) Absorption spectra for select films with dilute oxygen in a ZnS matrix. The arrow indicates the direction the absorption edge shifts with an increase in oxygen content. The compositions listed were found through RBS. These films were grown by rf magnetron sputtering. 28
Figure 3.3: PR results for $ZnO_{1-x}S_x$ films grown on ZnSe substates grown by RF magnetron sputtering. 30
Figure 3.4: Bandgap determined from PR measurements versus sulfur content determined by RBS. 31
Figure 3.5: Schematic of XPS showing how the sample and detector are connected in order to measure the binding energy of states in a sample.....32
Figure 3.6: (a) XPS Zn2p spectra of several films with labeled sulfur content, (b) XPS S2p spectra of several films with labeled sulfur content. The composition listed is the surface composition found using the Zn2p and S2p XPS spectra. 34
Figure 3.7: XPS valence band spectra for $x \leq 0.27$, the compositions listed were found through RBS. The arrow indicates the monoatomic upward shift in the valence band as sulfur content increases. 35
Figure 3.8: Sample plot with linear extrapolation of XPS valence band spectra edge used to determine the binding energy a sample with x=0.16. 36
Figure 3.9: The VBE positions determined from linearly extrapolating the XPS valence band spectra. The VBE positions are plotted with respect to vacuum level.....37
Figure 3.10: Measured absorption spectra for 0.04 sulfur film (determined by RBS) and the calculated theoretical fit using the VBAC model. The separate absorption contributions are also shown. The sulfur level is 0.30 eV above the ZnO valence band and the coupling parameter, CVB, is 0.60eV. 39
Figure 3.11: Calculated band structure for the 0.04 sulfur film. 40
Figure 3.12: Measured absorption spectra for 0.10 oxygen film (determined by RBS) and the calculated total absorption using the CBAC model. The separate absorption contributions are also shown. The coupling parameter, C_{CB}, is 1.5 eV. 41
Figure 3.13: Calculated band structure for the 0.10 oxygen film (x=0.9).....42
Figure 3.14: (a) Calculated conduction band and valence band edges. (b) Composition dependence of the bandgap of $ZnO_{1-x}S_x$ alloys. BAC line was determined by subtracting the calculated valence band edge from the calculated conduction band edge shown in (a). The experimental bandgaps found using the absorption fittings are plotted alongside the experimental data of Meyer et al [44]. 44
Figure 3.15: Superstrate configuration for the fabricated solar cells.....46

Figure 3.16: Visual representation of a current-voltage curve for a solar cell. At zero voltage the current is equal to J_{SC}. At zero current the voltage is equal to V_{OC}. The FF is defined as the ratio of the maximum power of the cell over the product of V_{OC} and J_{SC}.....47
Figure 3.17: J-V (left) and Q.E. (right) results for solar cell with a $ZnO_{0.95}S_{0.05}$ layer.....48
Figure 3.18: J-V (left) and Q.E. (right) results for solar cell with a $ZnO_{0.82}S_{0.18}$ layer.....49
Figure 3.19: J-V (left) and Q.E. (right) results for solar cell with a $ZnO_{0.25}S_{0.75}$ layer.....50
Figure 3.20: J-V (left) and Q.E. (right) results for solar cell with a $ZnO_{0.05}S_{0.90}$ layer.....51
Figure 3.21: Overall J-V (left) and Q.E.(right) results. Using the best cell from every condition. 52
Figure 4.1: θ–2θ X-ray diffraction of Ga_2O_3 films grown at different substrate temperatures. Films at 650C were shown to be (-2 0 1) β-Ga_2O_3 films. All unlabeled peaks correspond to sapphire. 56
Figure 4.2: The sulfur ratio of films grown at varying substrate temperatures. As the substrate temperature increases the sulfur ratio decreases due to outgassing.....58
Figure 4.3: Shows the ([S]+[O])/[Ga] ratio is close to 1.5 indicating stoichiometric films. S, O and Ga quantities determined by RBS.....58
Figure 4.4: θ–2θ X-ray diffraction patterns of a (-2 0 1) β-Ga_2O_3 film compared to two $Ga_2(O_{1-x}S_x)_3$ films shown to be amorphous via XRD.....59
Figure 4.5: a) HR-TEM image of a $Ga_2(O_{1-x}S_x)_3$ film with x= 0.013 and a thickness of 65 nm. Three layers are indicated in the image. b) Fast Fourier Transform (FFT) that shows a diffused ring pattern of the $Ga_2(O_{1-x}S_x)_3$ layer indicating that film is indeed amorphous. The red lines indicate dots in the FFT that are from adjacent crystalline layers.....60
Figure 4.6: Absorption coefficient for various $Ga_2(O_{1-x}S_x)_3$ with x<0.35.....61
Figure 4.7: (a) Measured and calculated absorption coefficient for $Ga_2(O_{1-x}S_x)_3$ with x=0.067. The calculations were performed using the VBAC model. (b) Contributions of different optical transitions to the total calculated absorption coefficient (dashed line) using the VBAC. The sulfur level is located 1 eV above the Ga_2O_3 valence band and the coupling parameter, $C_S(x=0)$, is 1.8 eV.....64
Figure 4.8: Band edges of ZnO, ZnS, Ga_2O_3 [92]and Ga_2S_3 [93]relative to vacuum with the sulfur level found to be consistent with previous $ZnO_{1-x}S_x$ work [18].....65
Figure 4.9: (a) Calculated BAC electronic band structure of a $Ga_2(O_{1-x}S_x)_3$ film with x=0.067 sulfur ratio. It shows the various valence bands that resulted from the interaction of the S states with the matrix valence band. (b) The (a) zoomed in to illustrate the details of valence band structure.....66
Figure 4.10: Composition dependence of the bandgap of $Ga_2(O_{1-x}S_x)_3$ alloys. BAC bandgap was determined by subtracting the calculated valence band edge from the calculated conduction band edge shown in (b).....67
Figure A.1: Band offsets of various semiconductors along with the position of cation d levels. Compiled from Refs. [96]-[99]……...73

List of Tables

Table 2.1: Sulfur content measured through RBS for the four samples studied using TEM.....22
Table 3.1: List of sulfur content and thickness for the solar cells that were fabricated.....46
Table 3.2: The Open Circuit Voltage (V_{OC}), fill factor (FF) and short circuit current (J_{SC}) results for a CdTe solar cell with a $ZnO_{0.95}S_{0.05}$ layer.....48
Table 3.3: The Open Circuit Voltage (V_{OC}), fill factor (FF) and short circuit current (J_{SC}) results for a CdTe solar cell with a $ZnO_{0.82}S_{0.18}$ layer with 18% sulfur.....49
Table 3.4: The Open Circuit Voltage (V_{OC}), fill factor (FF) and short circuit current (J_{SC}) results for a CdTe solar cell with a $ZnO_{0.25}S_{0.75}$ layer.....50
Table 3.5: The Open Circuit Voltage (V_{OC}), fill factor (FF) and short circuit current (J_{SC}) results for a CdTe solar cell with a $ZnO_{0.05}S_{0.90}$ layer.....51
Table 3.6: Overall cell comparison of cells fabricated in this work compared to the record CdTe, CZTS and CIGS cells [58].....53

Acknowledgments

I thank all the people who have in some shape or form made this dissertation possible through their mentorship, support, encouragement and friendship throughout my years as a graduate student.

I thank my one of many research advisors, Professor Oscar Dubon, for genuinely caring for the well-being of his students. I recall many times when he would ask how I was doing and would encourage me to take personal time when I would go through periods of high stress (and numerous migraine headaches). Thank you for being accommodating, patient and for not giving up on me. I have had the opportunity to work with Dr. Wladek Walukiewicz, the guru of defects in semiconductors. Thank you for always having an open door and for all of the great discussions we had regarding semiconductor physics. Thank you for welcoming me into your group and enabling me to produce this work. I am also grateful for being able to work with Professor Kin Man Yu. His insight and experimental knowledge regarding propelled the work in this dissertation. Thank you for training me and teaching me how to interpret data and continuing to collaborate on projects after your move to Hong Kong.

I would like to thank Prof. Chris Dames, for having served as a co-chair on my dissertation committee. Thanks for supporting me as my ME advisor and providing me with important advice and suggestions. I would also like to thank Professor Liwei Lin for being part of my dissertation committee and serving as the chair in my qualifying exam committee. I would also like to thank the rest of my qualifying exam committee: Professor Junqiao Wu, Professor Kyriakos Komvopoulos, and Professor Samuel Mao.

I am indebted to Dr. Ting Ming for being a great officemate the first 4 years of my graduate studies and for providing great advice and encouragement. Thanks to Rafael Quevedo for his invaluable contributions on the initial growth of gallium oxide sulfide films. I would like to thank all of the Dubon, EMAT group members and visiting researchers with whom I have worked with, including: Edy Cardona, Dr. Chris Francis, Dr. Jose Fonseca Vega, Dr. Kyle Tom, Dr. Alex Luce, Dr. Doug Detert, Dr. Paul Rogge, Dr. Monika Welna, Dr. Natalie Segercrantz, Dr. Yeonbae Lee, Raj Kumar, Dr. Mark Hettick, Dr. Weiwei Gao, Dr. Kevin Wang, Dr. Matthew Beres. An enormous thank you also goes to my collaborators, Dr. Juan F. Sánchez Royo, Professor Chris Ferekides, and Professor Ali Javey, who pushed the progress of my projects forward with their insight and/or experimental contributions. Additionally, I would like to thank Dr. Petra Specht and Dr. Roberto dos Reis for conducting the electron microscopy work presented in this dissertation. I would also like to thank Dr. Andre Anders and Joe Wallig for supporting and maintaining the RBS system after Kin left. Thank you Jeff Beeman for helping with issues regarding the vacuum systems.

I also want to thank Diana Lizarraga, for directing several diversity STEM programs at UC Berkeley under the Cal NERDS name. As an undergraduate student, I had the opportunity to conduct research as a visiting scholar. Di welcomed me to the Berkeley campus with open arms. My experience as a visiting scholar was a major factor in my decision to pursue graduate studies

at UC Berkeley. Thank you for always inviting me to Cal NERDS events such as: serving on graduate student panels, leading workshops, lunches and end of the year banquets.

I also thank Professor Oscar Dubon for championing the first ever Bay Area Graduate Pathways to STEM (GPS) graduate outreach event to inspire diverse talent to become the next generation of innovative leaders through advance engineering degrees. I thank Melton Erol and the 2015 graduate student committee (Dr. Hector Perez, Dr. William Tarpeh, Regan Patterson, Christina Fuentes, Raj Kumar, Dr. Allan Ogwang and Karina Chavarria) for volunteering and dedicating their time to make this event a reality.

This work wouldn't have been possible without the financial support I received from the National Science Foundation Bridge to the Doctorate Fellowship, the Robert N. Noyce Memorial Fellowship in Microelectronics, the Chang Li-Tien Fellowship, the Coca-Cola Company and Ray & Carmela Mellado. The work presented here is also part of the Electronic Materials Program at LBNL and were supported by the Director, Office of Science, Office of Basic Energy Sciences, Materials Sciences and Engineering Division, of the U.S. Department of Energy under Contract No. DE-AC02-05-CH1123.

I have been very lucky to have met my significant other, Hector Perez, during my time as a graduate student. Thank you for inspiring, challenging and reminding me to have solutions instead of excuses. In the five years that I have known you, I have achieved more than what I thought possible through your guidance, support and motivation.

This wouldn't have been possible without my parents Diego and Beatriz Jaquez. Even though I was 9 hrs away from them, they always found a way to show me their unconditional love by calling me (almost every day), sending me care packages, and supporting my decision to stay in school for so long. I dedicate this dissertation to them, for choosing to immigrate to the U.S. so I could take advantage of opportunities they were unable to pursue.

Chapter 1

1 Introduction

Semiconductor materials are everywhere, e.g., smartphones, computers, cars. We are moving towards an even more connected world where objects embedded with electronic devices collect and exchange data while being connected to the internet –Internet of Things (IoT). The number of IoT connections is expected to reach 125 billion by 2030 [1]. At the same time, as the population and economy grows, so does the energy demand. The U.S. Energy Information Administration projects that world energy consumption will grow by 28% between 2015 and 2040 [2]. Therefore, it is crucial that devices utilize energy and other resources efficiently while decreasing in cost. This development would be unimaginable without the invention of the transistor in 1947 at Bell Labs. In 1965, Gordon Moore, co-founder of Intel Corporation, predicted that the number of transistors on a piece of silicon would double every couple of years [3]. His insight later coined "Moore's Law" became the golden rule for the electronics industry which has driven advancements in technology for over 50 years and continues to have a significant impact. Today's chips can perform more complicated tasks while getting smaller, enabling their use in devices that improve our lives.

Germanium (Ge) and silicon (Si) are traditional elemental semiconductors that have been heavily studied since the invention of the transistor. For Si and Ge, the sample growth, control of the bandgap, and doping processes are well understood and realized [4]. Silicon has been the go-to material for microelectronics and semiconductor technologies due to its large abundancy (~28 percent of the Earth's crust is Si) and low cost [5]. Unfortunately, Si and Ge are not the best materials for all applications. Compound semiconductors consisting of two or more elements are widely used in high speed applications and in devices that require the absorption or emission of light. The III-V materials have dominated compound semiconductor research resulting in successful implementation in optoelectronic applications. For example, gallium arsenide (GaAs) and gallium nitride (GaN) are commonly found in light emitting diodes (LEDs) for energy-efficient lighting. In addition, GaAs-based and indium phosphide (InP)-based materials are used in high-speed circuits due to high electron mobilities. In addition, ternary and quaternary III-V materials have found applications in photovoltaic technologies due to the ability to tune the electronic properties.

Research in compound semiconductors has also been focused on the development of II-VI technologies, two dimensional (2-D) materials (*e.g.* molybdenum disulfide (MoS_2), tungsten diselenide (WSe_2) and more complex semiconductor compounds (*e.g.* hybrid organic-inorganic perovskites, copper indium gallium diselenide). Despite the increase in research on novel semiconductor materials, we are currently only using a small portion of available semiconducting

materials. In order for novel materials to be commercially viable, it is important to understand their structural, electrical and chemical properties. Doing so will aid in the ability to design materials for specific applications such as high power electronics and photovoltaics (Figure 1.1).

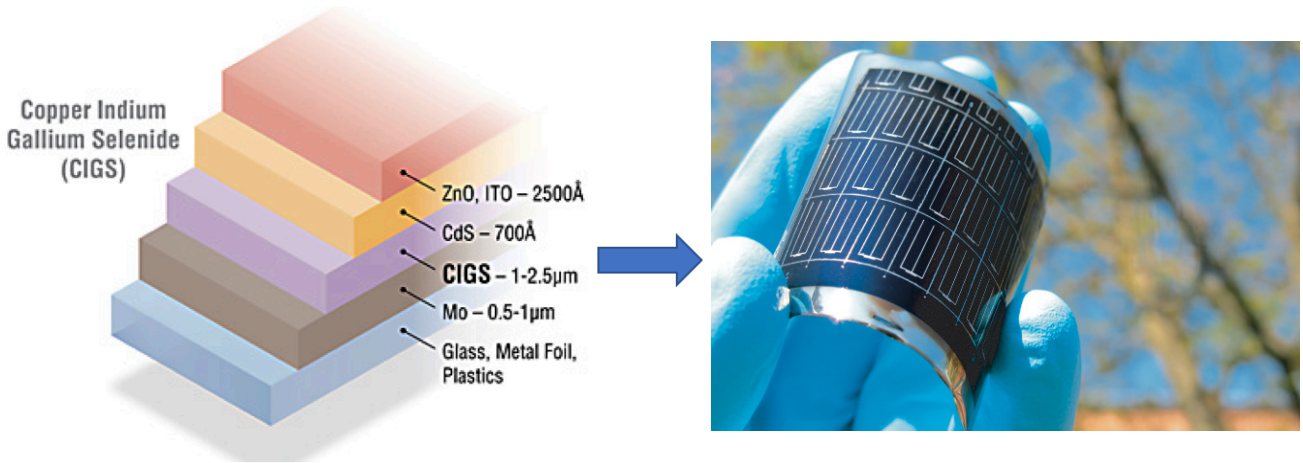

Figure 1.1: (Left) CIGS thin film photovoltaic layer structure adopted from [6] and (Right) Flexible CIGS solar cell [7].

1.1 Band Structure Engineering Through Alloying

Band structure engineering through the alloying of two or more semiconductor compounds is one method that modifies semiconductor properties providing a means to control the properties of a wide range of electronic materials to meet device requirements. It does this by modifying the bandgap (E_g), lattice constants, and the location of the band edges (conduction band and valence band edges) relative to vacuum for the material.

The electronic bandgap is defined as the minimum energy required to excite (relax) an electron from a bound (free) state to a free (bound) state. In semiconductors this is the difference between the conduction band minimum and the valence band maximum (Figure 1.2). Direct semiconductors have the location of the conduction band minimum and the valence band maximum at the same k-vector (conservation of momentum) which involves the absorption or emission of a photon. On the other hand, in indirect semiconductors the conduction band minimum and the valence band maximum are at different k-vectors. Therefore, in indirect bandgap semiconductors, the optical transitions between the valence and conduction band must also involve the absorption or emission of a phonon in addition to the absorption or emission of a photon.

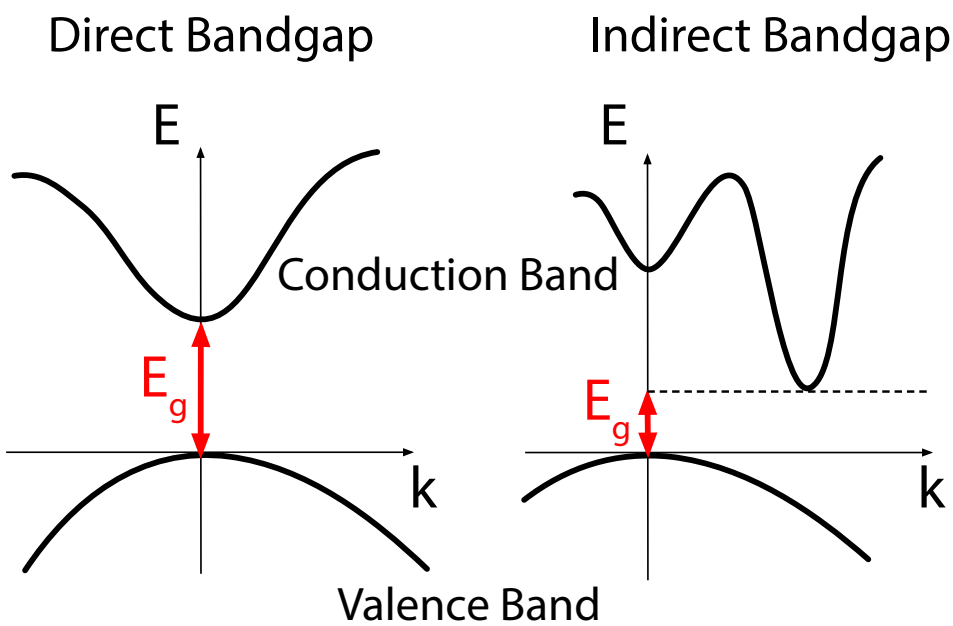

Figure 1.2: Schematic dispersion relation of a direct versus that of an indirect bandgap semiconductor.

The E_g is important as it determines the color of light that is emitted in light-emitting diodes (and lasers) and the onset of absorption in photovoltaic devices. The lattice constants are important because they provide information on the structure of the semiconductor material and the system of materials that can be grown to form heterojunction-based devices. The conduction-band and valence-band edge locations relative to vacuum are important for understanding the electronic behavior at the interface that will form with other insulating, semiconducting or metallic materials. Discontinuities between the valence-band maximum or the conduction-band minimum between two semiconductors—also known as band offsets—can act as a barrier for charge transfer across the interface. Therefore, the band offsets are an important property that determines the feasibility and performance of heterostructure devices with respect to efficiency. Band offsets for a few semiconductors can be seen in Figure 1.3 and in Figure A.1.

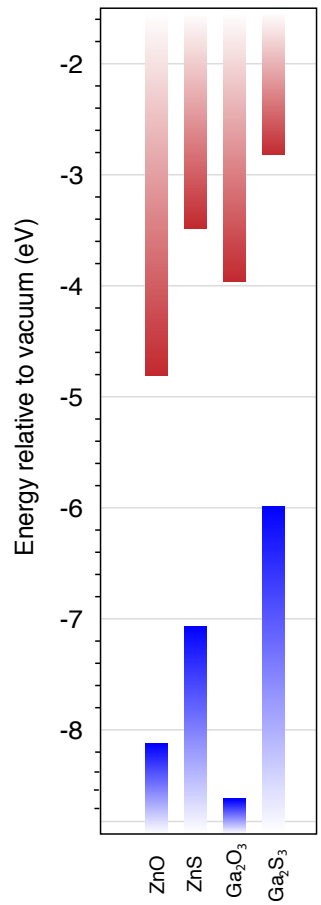

Figure 1.3: The conduction-band and valence-band edge locations relative to vacuum for ZnO, ZnS, Ga_2O_3 and Ga_2S_3.

The simplest way to predict these properties is to assume that they vary linearly between the endpoint compounds. This approach works well to predict the lattice parameters of semiconductor alloys – known as Vegard's law [8]. A simplified approach used to predict the electronic band edges and bandgap of a randomly distributed alloy is known as the virtual crystal approximation (VCA). The VCA assumes that the alloy is randomly distributed throughout and it replaces the crystal potential that the valence electrons experience with the linear interpolation of the crystal potential of the end compounds at each composition. This approach predicts little deviation from the linear interpolation of the bandgap and band edges from those of the end compounds [9]. Unfortunately, the VCA approach is too simplistic, and most alloys deviate from it. For this reason, an empirical quadratic term known as the bowing parameter has been used to fit the bandgap dependence as a function of composition to describe how much it deviates from VCA. Thus for the alloy of $A_{1-x}B_x$ of two semiconductors A and B, the bandgap is given by

$$E_g^{AB}(x) = E_g^A \cdot (1-x) + E_g^B \cdot x - b \cdot x \cdot (1-x). \qquad (1.1)$$

Where b is the bowing parameter, x is the composition, E_g^A and E_g^B are the bandgaps of the end point compounds, and $E_g^{AB}(x)$ is bandgap of the alloy at a specified composition. Semiconductor alloys that consist of isoelectronic elements that are well-matched with regard to atom size,

electronegativity and ionicity (*e.g.* AlGaAs, ZnSeS) tend to have little or no deviation from the linear interpolation of the end point compounds as predicted by the VCA model [3]. On the other hand, semiconductor alloys that consist of isoelectronic elements that are not well-matched with regard to atom size, electronegativity and iconicity, are not well described with the VCA or with the bowing parameter model [10], [11].

1.2 Highly Mismatched Alloys

The semiconductor alloys of interest in this research are highly mismatched alloys (HMA), a class of semiconductors alloys that contain isovalent anions of considerably different size and/or electronegativity which result in a restructuring of the electronic band structure. Due to the high mismatch, the bandgap of these materials cannot be easily predicted with the VCA model or modified VCA models [12]. The bandgap of HMA drastically decreases by the substitution of a small fraction (few percent) of anions with an isovalent element [12]-[18]. It is possible to preferentially tune the conduction band or valence band of an HMA by properly selecting the alloying anion in a semiconductor matrix. This is advantageous in applications, such as heterojunction solar cells and photoelectrodes for photoelectrochemical water splitting, where band alignment is crucial for efficient operation of the device.

There have been numerous theoretical investigations focused on understanding the unusual reduction in bandgap [19], [20]. A phenomenological model, called the conduction band anticrossing (BAC) model was proposed to explain the experimental observations of the splitting of the conduction band in $Ga_{1-x}In_xN_{1-y}As_y$ alloys with dilute-As content [13].

1.2.1 The Conduction Band Anticrossing Model

For the dilute-N $Ga_{1-x}In_xN_{1-y}As_y$ alloys, the conduction BAC model considers a repulsive interaction between the highly electronegative localized states of the dilute element (in this case nitrogen) and the extended states of the semiconductor matrix (GaInAs) conduction band. It was assumed that the interaction of these two states can be treated as a perturbation, therefore, it becomes the following eigenvalue problem:

$$\begin{vmatrix} E_k^c - E(k) & C\sqrt{x} \\ C\sqrt{x} & E^d + i\Gamma^d - E(k) \end{vmatrix} = 0 \qquad (1.2)$$

where E_k^c is the conduction band energy of the matrix material, $E(k)$ is the dispersion relation of the band, Γ^d is a broadening parameter, x is the anion alloy composition, $C\sqrt{x}$ describes the interaction between the localized states and the extended states, and E^d is the energy of the localized level. If broadening can be neglected, we can take $\Gamma^d = 0$, therefore, equation 1.2 reduces to the standard BAC Hamiltonian.

$$\begin{vmatrix} E_k^c - E(k) & C\sqrt{x} \\ C\sqrt{x} & E^d - E(k) \end{vmatrix} = 0 \qquad (1.3)$$

The result of this interaction leads to a splitting of the conduction band into two subbands labelled as $E_-(k)$ and $E_+(k)$ given by solving equation 1.4.

$$E_\pm(k) = \frac{1}{2}\left[(E^d + E(k)) \pm \sqrt{(E(k) - E^d)^2 + 4C^2x}\right] \qquad (1.4)$$

where $E_+(k)$ is the matrix-like conduction band since it is composed of mostly delocalized states, and $E_-(k)$ is the mostly localized band derived state. The $E_-(k)$ and $E_+(k)$ subbands have been confirmed experimentally through photomodulated reflectance measurements [13].

The conduction band anticrossing model is only valid when

1. The localized states (dilute anion element) are much more electronegative than the matrix anion element;
2. The alloying anion element's concentration << 1, therefore only valid in the dilute region.

In instances where the dilute anion element is much more electronegative than the matrix anion element, it acts as a weak acceptor and localizes electrons at s-like states. According to Koster-Slater theory, these localized electron states tend to lie near the conduction band of the matrix semiconductor material [21], [22]. For the case of dilute-N $Ga_{1-x}In_xN_{1-y}As_y$, the dilute anion element is nitrogen and the matrix anion element is As. Since N is much more electronegative than As, the N localized states lie near the conduction band of GaInAs.

1.2.2 The Valence Band Anticrossing Model

The most well-known and studied HMA is the $GaN_{1-x}As_x$ system. In the As-rich region, incorporating 0.10 of N (x=0.9) decreases the bandgap of GaAs from 1.42 eV down to ~0.95 eV; while in the N-rich region with x=0.01 there's an abrupt reduction in the bandgap from 3.4 eV to ~2.8 eV (Figure 1.4). Applying equation 1.1 to these results, a bowing parameter of 16.2 eV would be needed, predicting a negative bandgap in a wide range of compositions as seen in Figure 1.4.

As more studies were performed on $GaN_{1-x}As_x$ throughout the composition range, it was found that in the dilute N region the bandgap dependence could be explained with the conduction BAC model (Figure 1.5). In addition, in the As-rich region the bandgap dependence suggested that the band anticrossing phenomena was also applicable to dilute concentration of less electronegative anions compared to the matrix anion. Due to the lower electronegativity, the dilute anions act as donors and localize holes at p-like states. Therefore, the dilute anion states tend to lie near the valence band of the semiconductor matrix. Therefore, an anticrossing interaction will also induce a restructuring of the valence band similar to the conduction band anticrossing case. Due to the p-like nature of the localized states near the 3 top valance bands (heavy hole, light hole and spin-orbit split off band), the interaction results in a 12x12 Hamiltonian matrix [23]. Fortunately, further

studies were able to show that the 12x12 Hamiltonian could be approximated using a single valance band and a single localized level [24].

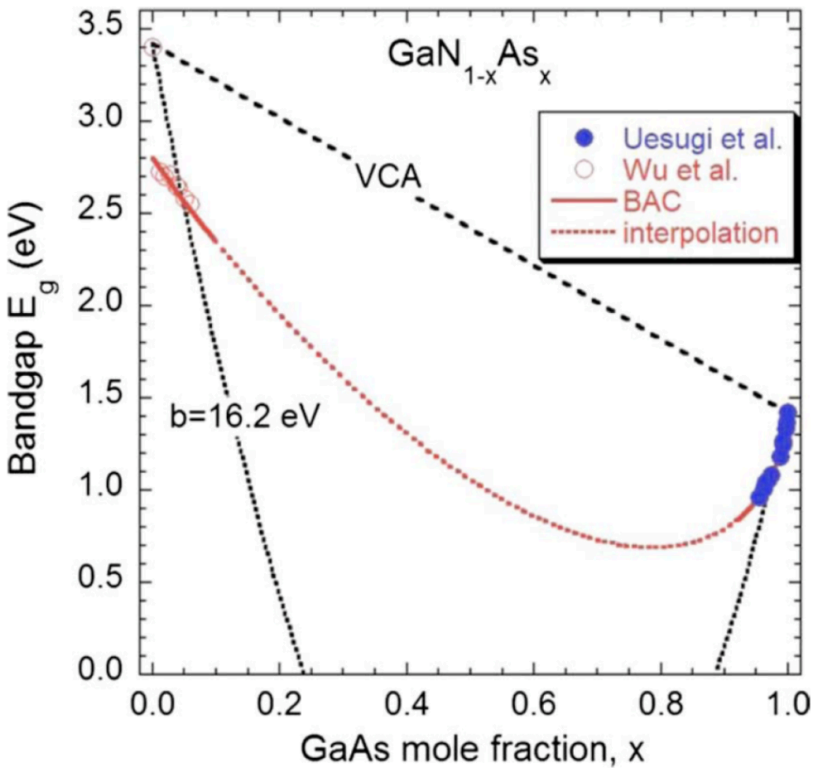

Figure 1.4: Bandgap of dilute As-rich and N-rich $GaN_{1-x}As_x$ alloys as a function of x. The solid line is the calculated bandgap of dilute $GaN_{1-x}As_x$ alloys based on the BAC model interpolated over the entire composition range. Bandgaps by VCA and by a forced quadratic fitting to the experimental gap energies using a single bowing parameter of b=16.2 eV are also shown. Adopted from [11].

The observed large bowing in the composition dependence of the energy bandgap arises from the anticrossing interactions between (1) the valence-band of GaN and the localized As-level close to the GaN valence-band maximum for N-rich alloys (valence BAC) and (2) the conduction-band of GaAs and the localized N-level close to the GaAs conduction band minimum for the As-rich alloys (conduction BAC). The BAC model has been successful in explaining the restructuring of the electronic band structure of numerous HMA in the dilute regions (e.g., $GaN_{1-x}Sb_x$, $ZnO_{1-x}Se_x$, $ZnO_{1-x}Te_x$, $ZnTe_{1-x}S_x$ alloys) [12], [13], [24]-[26].

In most cases, the growth of HMA are difficult, a major challenge that has limited the ability to obtain good quality crystalline materials, typically only achieved in the dilute alloy limit due to solubility limits. Therefore, the deposition technique and growth temperature are important for the growth of these types of alloys. In the case for the $GaN_{1-x}As_x$ system, a linear interpolation between the valence BAC and conduction BAC was used to estimate the bandgap across the entire

composition range. $GaN_{1-x}As_x$ alloys in the mid-range region are amorphous, and although the BAC model was not intended to apply to amorphous semiconductor alloys due to the lack of long-range order, there seems to be qualitative agreement between the BAC model and experimental results as seen in Figure 1.5 [10].

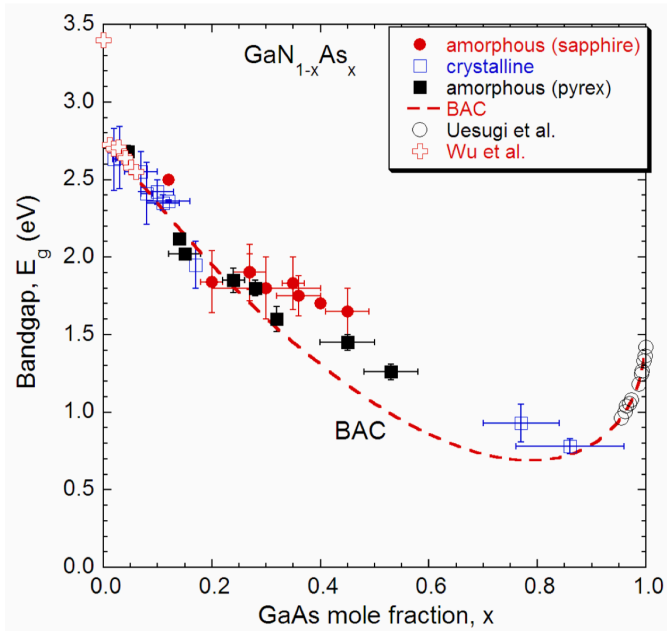

Figure 1.5: Bandgap dependence of $GaN_{1-x}As_x$ alloys with the BAC model [10].

1.3 Structure of the Dissertation

In this dissertation there are five chapters. The first chapter was an introduction that discusses the importance of semiconductor materials and why it is important to continue studying novel semiconductor materials for emerging technologies. In addition, it provided an introduction to HMA materials and the BAC model vital to the work presented in the remaining chapters.

Chapters 2 and 3 are dedicated to the $ZnO_{1-x}S_x$ material system. Chapter 2 describes two growth methods, PLD and RF magnetron sputtering, and how the growth conditions affect the structural properties. Chapter 3 discusses the optical properties and the electronic band structure of $ZnO_{1-x}S_x$ alloys.

Chapter 4 is dedicated to the Ga_2O_3-Ga_2S_3 material system. This chapter describes the material synthesis and its structural, optical and electronic band structure properties of Ga_2O_3-Ga_2S_3 alloys. Chapter 5 is the conclusion and future work.

Chapter 2

2 $ZnO_{1-x}S_x$ Material Synthesis and Structural Analysis

The high demand and need for renewable energy have triggered a vast exploration of potential materials for energy applications. As Si solar cells reach their theoretical efficiency limit, researchers have focused on developing alternative technologies. These efforts have allowed for new solar cells technologies to enter the market such as copper indium gallium diselenide (CIGS) and CdTe thin film solar cells. Unfortunately, CIGS utilizes indium (In), a relatively rare element that due to the success of indium tin oxide (ITO) as a transparent conducting oxide (ITO) in high demand for applications such as solar cells and flat panel displays, increase the price and demand for indium. On the other hand, CdTe technology utilizes cadmium (Cd), a toxic material that is known to cause cancer [27].

Other materials of interest for solar cell technologies include copper zinc tin sulfide (CZTS), hybrid organic-inorganic perovskites as absorber materials, zinc oxide (ZnO) and zinc sulfide (ZnS) as buffer layers. CZTS-based solar cells are of interest because they utilize more abundant and cheap elements, yet progress in improving solar cell efficiency has been slow [28]. Hybrid organic-inorganic perovskites solar cells have garnered the interest of researchers as the efficiency of these cells have increased from 3.9% to more than 22% since 2009 [29] [30], yet they face challenges with material stability, the use of lead, and experience hysteresis effects [31]-[36].

Zinc oxide is a material of great interest because it is non-toxic, earth abundant, and relatively inexpensive [37]. ZnO has great potential for high-power electronics, ultra violet optical devices, and transparent conductors for photovoltaic applications due to its wide bandgap of 3.37 eV[38]. There have been challenges to the development of oxide-based devices, especially the inability to obtain reliable p-type conductivity in ZnO has led to studies focused on understanding how its electronic structure, native defects, and unintentional impurities affect its electrical behavior. In addition, oxide-based alloy studies have also emerged (*e.g.* $ZnO_{1-x}Te_x$, $ZnO_{1-x}Se_x$, $Cd_{1-x}Zn_xO$, $Mg_{1-x}Zn_xO$), but there remains much to be learned, especially since the alloy properties are drastically affected by the growth conditions. It is important to study the materials synthesis of alloys throughout various compositions in order to enable the operation of oxide optoelectronics over a broad spectrum of wavelengths [39]. In the case for $ZnO_{1-x}Se_x$ and $ZnO_{1-x}Te_x$ alloys, the difficulty in synthesizing them was overcome by lower growth temperatures and non-equilibrium growth conditions[16], [17], [40], [41].

Zinc sulfide is another wide bandgap semiconductor with a bandgap of 3.6–3.8 eV that is currently used in optoelectronic devices such as blue light-emitting diodes and n- window layers for thin-film solar cells [42]. It has been found that alloying ZnO with ZnS allows the room-temperature bandgap of ZnO to be modified [38], [43], [44], making it useful as a material for solar applications [18], [45]-[47]. $ZnO_{1-x}S_x$ alloys have been synthesized using rf magnetron sputtering [38], [44], PLD[48], chemical bath deposition, ALD [49], aerosol assisted chemical vapor deposition (AACVD) [50]. Despite various reports on the growth of $ZnO_{1-x}S_x$ alloys, only limited information is known about their electronic structures [18].

This chapter presents the growth of $ZnO_{1-x}S_x$ using RF magnetron sputtering and PLD. Section 2.1 provides an overview of sputtering. Section 2.1.1 focuses on the RF magnetron setup and growth parameters used in this work. Section 2.2 provides an overview of PLD. Section 2.2.1 focuses on the PLD setup and growth parameters used in this work. Section 2.3 discusses the thickness and composition characterization results obtained from Rutherford backscattering spectrometry (RBS). Section 2.4 discusses structural characterization through X-ray diffraction (XRD) and transmission electron microscopy (TEM).

2.1 Sputtering Overview

Sputtering is a physical vapor deposition (PVD) method in which atoms are ejected or sputtered from a target by bombarding the surface with energetic ions [51]. The sputtering process can be divided into four major categories: direct current (DC), alternating current (AC) –though primarily radio frequency (RF), reactive and magnetron sputtering. Hybrids between categories (e.g. RF magnetron sputtering) also exist. A simple DC sputtering geometry is shown in Figure 2.1 in which the anode is the substrate (which can be grounded, biased positively or negatively) and the cathode is the target (connected to the negative terminal of a DC power supply). After evacuating the chamber to an appropriate pressure (i.e. $<10^{-5}$ torr), a gas (typically argon (Ar)) is introduced to a few to a hundred millitorr to initiate and sustain a plasma (visible glow) between the anode and the cathode. A plasma in this context is a weakly ionized gas consisting of electrons, ions, and neutral atomic and molecular species. The creation of a plasma begins with a stray electron close to the cathode being accelerated to the anode by the applied electric field. After gaining enough energy, the accelerating electron collides with a neutral Ar gas atom which transforms it into an Ar^+ ion while also releasing two electrons. The two electrons then go on to form additional ions which release more electrons thus sustaining a plasma. Positive Ar^+ ions in the plasma strike the cathode ejecting/sputtering target atoms through momentum transfer. The sputtered target atoms pass through the plasma eventually reaching and depositing on the substrate.

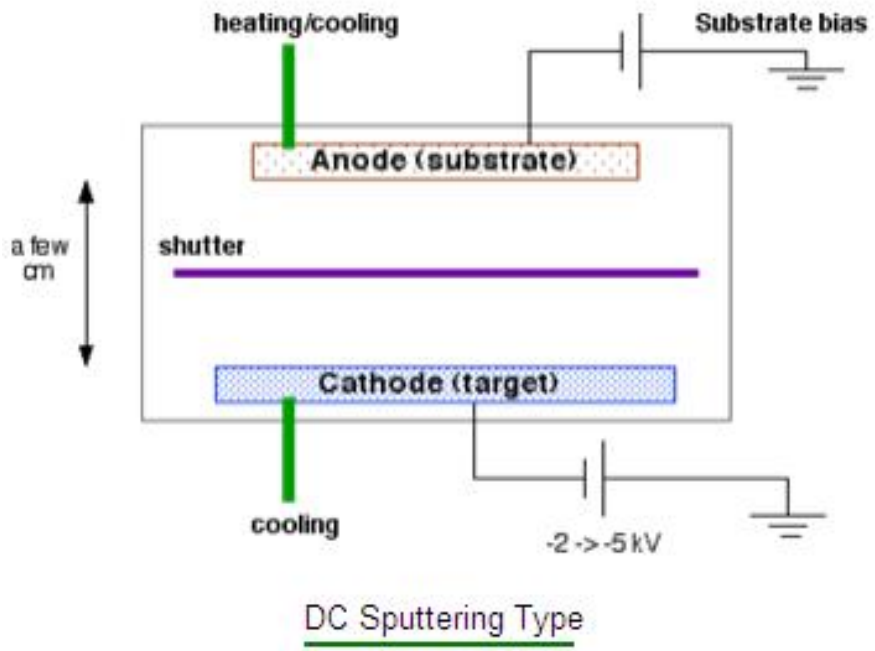

Figure 2.1: Simple DC sputtering geometry

2.1.1 RF Magnetron Sputtering Experimental Setup and Growth Parameters

RF magnetron sputtering was utilized for this work because it is a technique that allows for the synthesis of materials from highly resistive targets and non-equilibrium growth conditions. RF sputtering alternates the electrical potential which prevents charge accumulation on the surface of the target since the impendence of capacitors drop with increasing frequency [51]. In RF magnetron sputtering, magnets are placed behind the target to help keep electrons close to the target, allowing for faster deposition rates in addition to preventing electrons from bombarding the substrate surface. The setup used in this study had two sputtering guns enabling co-sputtering from two different targets. Figure 2.2 is a schematic and Figure 2.3 is an image of the RF magnetron co-sputtering setup used to deposit $ZnO_{1-x}S_x$ alloys located at Lawrence Berkeley National Laboratory.

In this work, undoped $ZnO_{1-x}S_x$ thin films were deposited on glass, double-side polished c-plane sapphire, ZnSe and silicon substrates using RF magnetron co-sputtering. Adjusting the sputtering power and target-substrate distance for two separate ZnO and ZnS targets controlled the alloy compositions of the films. Figure 2.4 is a sample calibration plot that shows how the sulfur composition was controlled by modifying the ZnO power while keeping the ZnS power, the Ar flow rate, chamber background pressure, substrate temperature, and both ZnO and ZnS target-substrate distance unchanged. Figure 2.5 is a sample calibration plot that shows how the sulfur composition was controlled by modifying the ZnS power while keeping all other growth parameters unchanged throughout the runs. The base vacuum pressure of the tool ~10^{-6} torr was

achieved through a turbomolecular pump. Argon flow into the growth chamber was controlled using a mass flow controller set to a flow rate of 10 SCCM. Igniting the Ar plasma was achieved by partially closing the gate valve on the turbo pump to reach a chamber pressure of ~20 mTorr. Once the plasma was ignited, the background pressure was then modified to 5 mTorr and maintained at that pressure during growth. The substrate was heated to the desired temperature and was allowed to stabilize at the desired temperature for ~ 30 min prior to any film deposition. The substrate temperature was measured through a thermocouple embedded in the chamber and is therefore, an estimate to the temperature at the surface of the substrate. The substrate was rotated throughout the film growth.

The growth conditions for these $ZnO_{1-x}S_x$ thin films were optimized to yield stoichiometric and crystalline films. Crystallinity was of concern due to a few results found in the literature reporting a miscibility gap in $ZnO_{1-x}S_x$ films where they could not be grown crystalline throughout the entire composition range or had an intermediate phase between the two materials [38], [48].

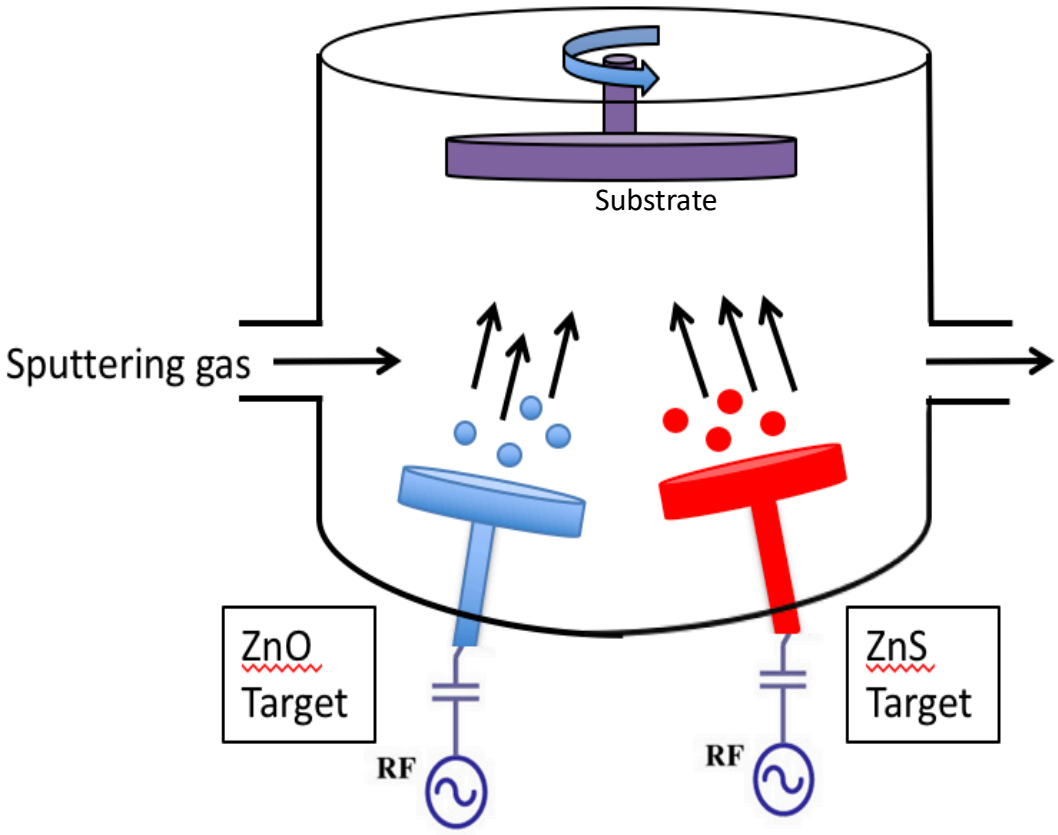

Figure 2.2: Simple schematic of RF magnetron co-sputtering setup used to deposit $ZnO_{1-x}S_x$ alloys.

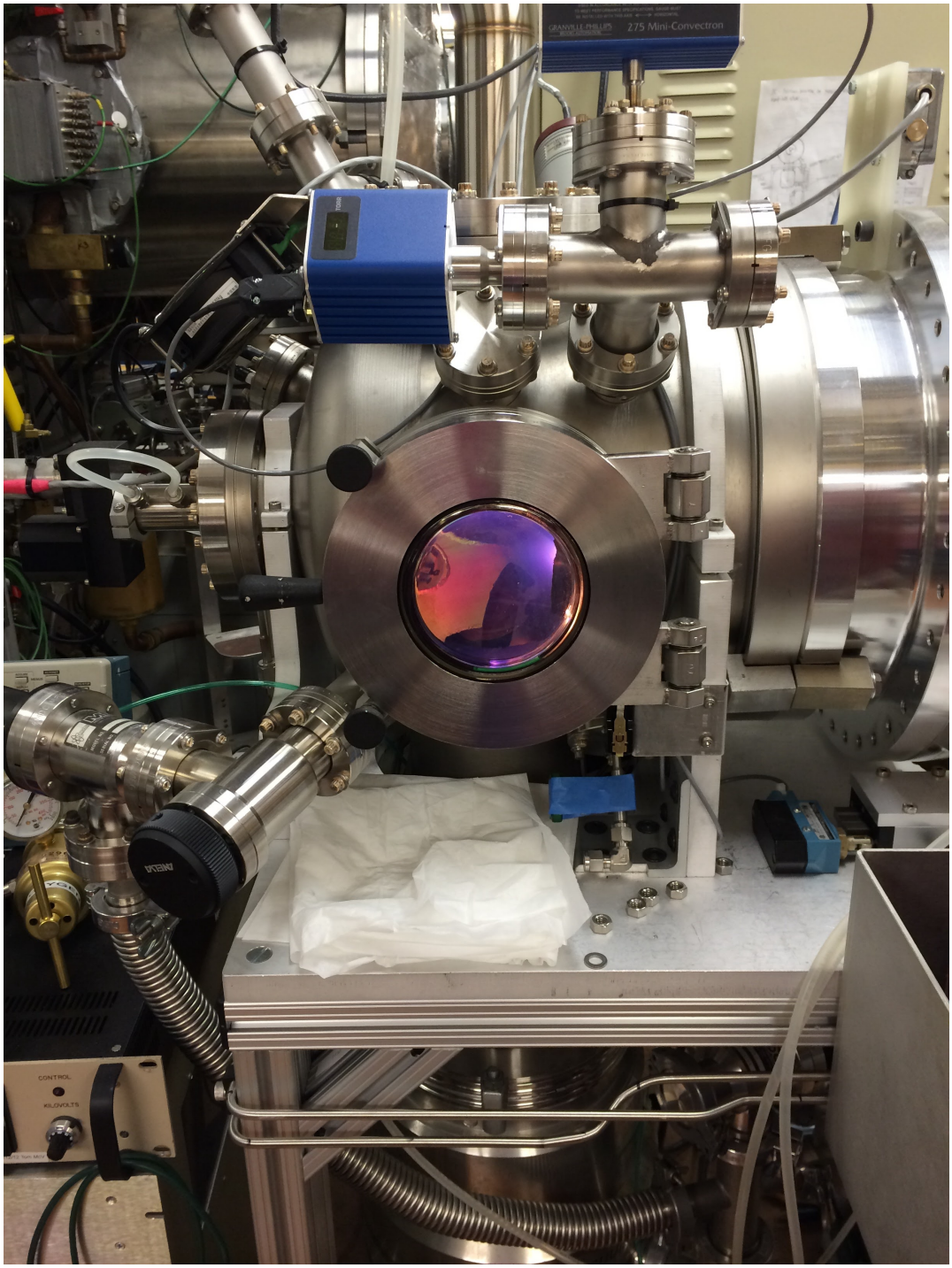

Figure 2.3: Image of RF magnetron co-sputtering setup used in this work.

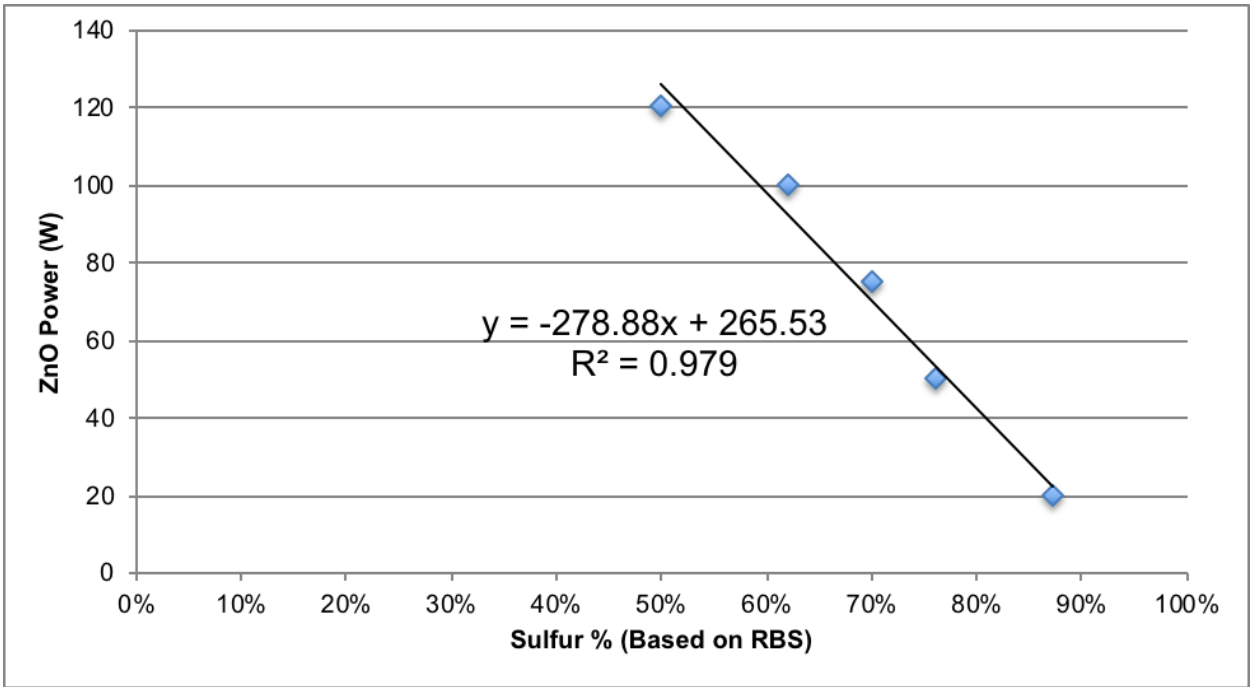

Figure 2.4: Sample calibration plot that shows how to control the sulfur composition by modifying the ZnO target power during growth. The ZnO target-substrate distance was kept at 4cm, the ZnS target-substrate distance was kept at 4cm, the Ar flow rate was kept at 10 SCCM, the background growth pressure was kept at 5 mTorr, and the ZnS power was kept at 100W for all runs shown.

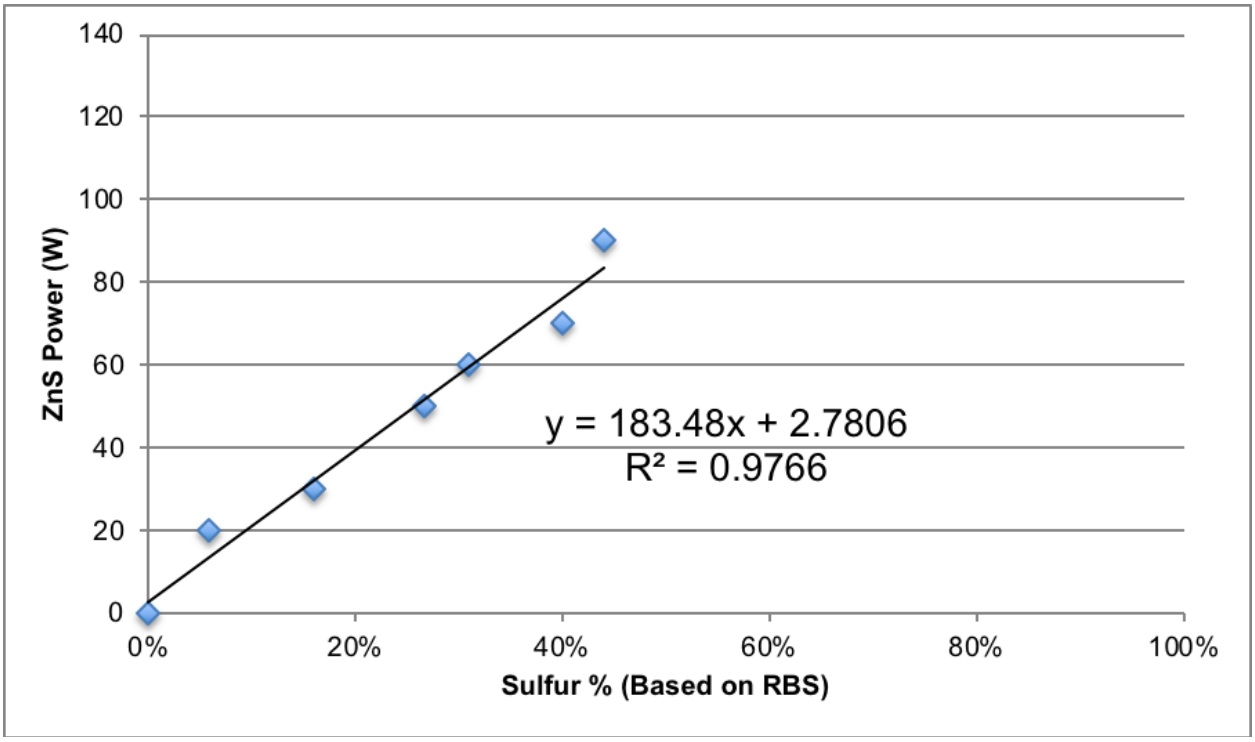

Figure 2.5: Sample calibration plot that shows how to control the sulfur composition by modifying the ZnS target power during growth. The ZnO target-substrate was kept at 4cm, the ZnS target-substrate was kept at 6cm, the Ar flow rate was kept at 10 SCCM, the background growth pressure was kept at 5 mTorr, and the ZnO power was kept at 120W for all runs shown.

2.2 PLD Overview

The pulsed laser deposition process is another physical vapor deposition (PVD) method that focuses a pulsed laser inside a vacuum chamber to strike onto a target surface that serves as the evaporation source. Most nonmetallic materials that are evaporated tend to have strong absorption in the ultraviolet spectral range reducing the penetration depths. Once the pulsed laser strikes the target surface, the absorbed beam energy is converted into thermal, chemical, and mechanical energy, causing electronic excitation of target atoms, ablation of the surface, and plasma (plume) formation [51]. The plume is highly directional onto the substrate where it forms a film. Background gases such as O_2, Ar, and N_2, are often introduced during deposition to help maintain film stoichiometry or aid in surface reactions.

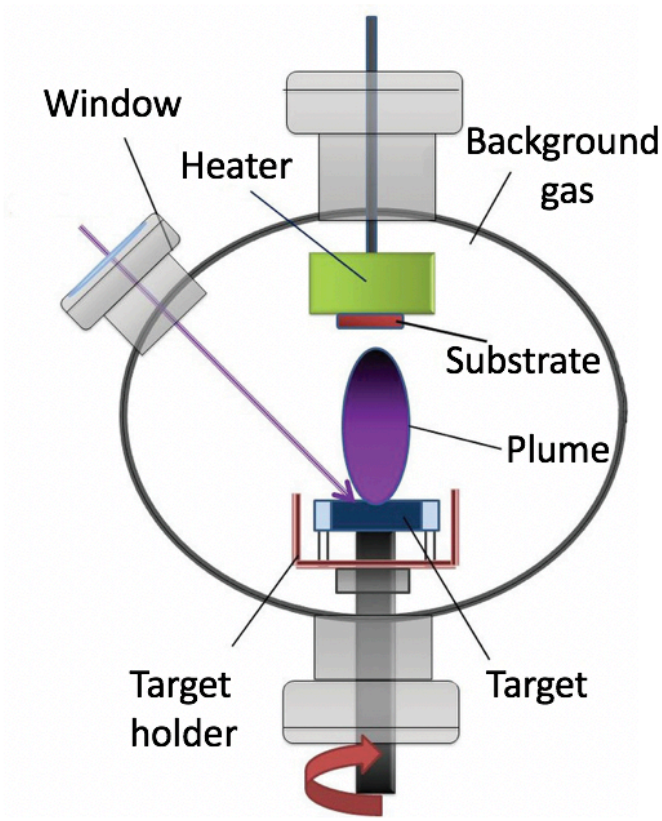

Figure 2.6: Schematic of PLD deposition

2.2.1 PLD Experimental Setup and Growth Parameters

In addition to RF magnetron sputtering, $ZnO_{1-x}S_x$ alloy samples were also grown by PLD on glass and double-side polished c-plane sapphire. PLD is another technique suitable for the growth of HMA oxide materials due to the potential for both stoichiometric transfer of target materials to the substrate and being able to deposit using non-equilibrium growth conditions [52]. A schematic of a PLD growth system is shown in Figure 2.6.

The SVTA PLD system used in this work is maintained by the Electronic Materials Group (EMAT) at Lawrence Berkeley National Laboratory. The PLD system was designed with a load-lock chamber separated from the growth chamber by a gate valve. The growth and load-lock chambers in this system are individually evacuated (< 10^{-4} Torr) with a roughing pump followed by a turbomolecular pump which pumps them down to ~10^{-7} Torr. The load-lock chamber design allows one to load a substrate without having to break vacuum in the main growth chamber. Venting the growth chamber can take up to an hour and pumping down the chamber to a background pressure of ~10^{-7} Torr takes ~8 hrs (compared to 15 minutes to vent and 40 min to pump the load-lock to ~10^{-7} Torr).

A high-energy pulsed laser, in this case a 248 nm KrF excimer laser with a 20ns laser pulse duration, is directed by two UV mirrors, focused through a lens, passing through a chamber port window and a sacrificial window to finally strike onto a pressed powder target. A Molectron Energy Max 400 laser energy meter was used to measure the laser intensity that reaches the pressed powder target location. It was found that ~75% of the output laser power actually reaches the target due to energy losses at the mirrors, lens, and windows. The laser energies presented in this work reflect the laser energy setpoint of the laser, representing the laser output of the laser and not what actually reaches the target. The laser spot area was measured to be 0.06 cm^2.

This PLD system has a wide parameter space to deposit thin film materials. The substrate temperature can be adjusted from room temperature (RT) to 800°C. The laser energy can be adjusted from 60 mJ to 700 mJ. The laser repetition rate can be adjusted from 0.25 to 50 Hz. The substrate to target distance can be modified from 5 to 9 cm. This system has the following background gas options: O_2, N_2, Ar, Ar/O_2, Ar/N_2 with an adjustable background pressure from the growth chamber base pressure ~10^{-7} to about 75 mTorr.

For the growth of $ZnO_{1-x}S_x$, cold-pressed powder targets with varying compositions of ZnO and ZnS were used. Samples were grown from a 10% (atomic percent) ZnS with 90% ZnO target, and a pure ZnO target. It is also important to note that the surface of the target affects the final composition of the films. Ablation during growth alters the composition of the target surface. To maintain target composition, PLD targets were sanded to remove damage.

2.3 Thickness and Composition Characterization

Rutherford backscattering spectrometry (RBS) is a non-destructive technique, also known as high-energy ion scattering, that can be used to determine the thickness and composition of thin film samples. It detects the energy of the backscattered ions with a solid-state detector (Si surface barrier detector) positioned at a backscattering angle relative to the incident ion beam. The amount of backscattered ions measured from an element is proportional its concentration in the sample. For these $ZnO_{1-x}S_x$ thin films, the film thickness and compositions were determined by RBS with a 3.04 MeV He^+ beam at a backscattering angle of 168° and using the SIMNRA simulation package to model the data [26].

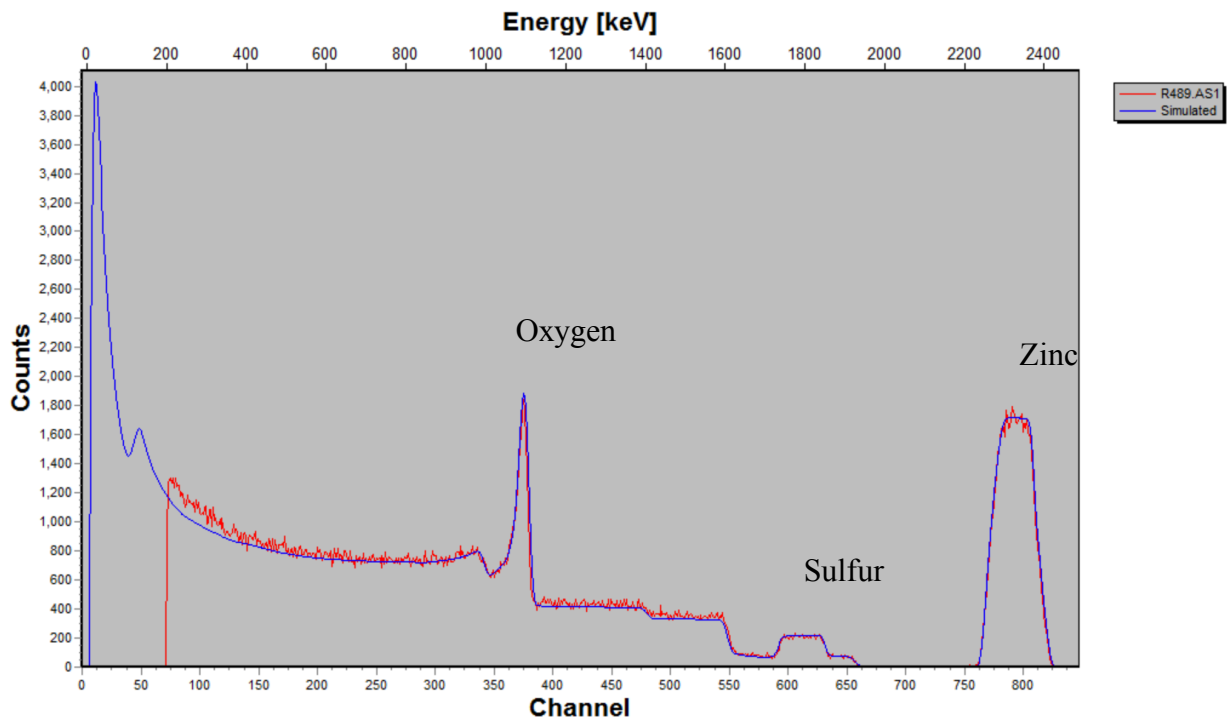

Figure 2.7: RBS spectra with the SIMNRA simulation for sample R489 with 31%S. The red line is the RBS data and the blue line is the simulated fit using SIMNRA.

Figure 2.7 shows an RBS spectrum with the SIMNRA simulation. From the SIMNRA simulation it is possible to extract the areal density (atom/cm^2) and composition of the films in atomic percent (at%). SIMNRA simulates the RBS spectrum based on the experimental conditions of the incident He-ion beam and spectrometer.

2.4 Structural Characterization

2.4.1 X-Ray Diffraction

The structural properties of $ZnO_{1-x}S_x$ thin films were investigated using standard powder X-ray diffraction techniques with Cu K_α radiation. This setup provides the ability to probe the phase, lattice constant, and texture of films, especially for polycrystalline thin-film samples. All films grown on glass were textured along the c axis and only the (0002) diffraction peak is visible in the XRD patterns. The XRD (0002) peaks were fitted using a Gaussian to obtain the 2θ angle as shown in Figure 2.8. Figure 2.9 shows XRD (0002) diffraction peaks for select $ZnO_{1-x}S_x$ films across the composition range. We note that ZnS exists in both zinc-blende and wurtzite structures. The structure of the S-rich films was not determined since the $(111)_{zincblende}$ peak coincides with the $(0002)_{wurtzite}$ peak of ZnS. Using grazing incidence phi scans, Meyer et al. [44] reported a wurtzite structure for $ZnO_{1-x}S_x$ films throughout the composition range. Because our $ZnO_{1-x}S_x$ films were synthesized using a similar method, they likely crystallize in the wurtzite structure as well. The XRD results show a monotonic shift of the $(0002)_{wurtzite}$ ZnO reflection towards smaller 2θ with increasing sulfur content. This indicates an increase of the lattice parameter of $ZnO_{1-x}S_x$ as

expected due to the substitution of larger S atoms with O. Using Vegard's law, the composition of the alloy can be determined.

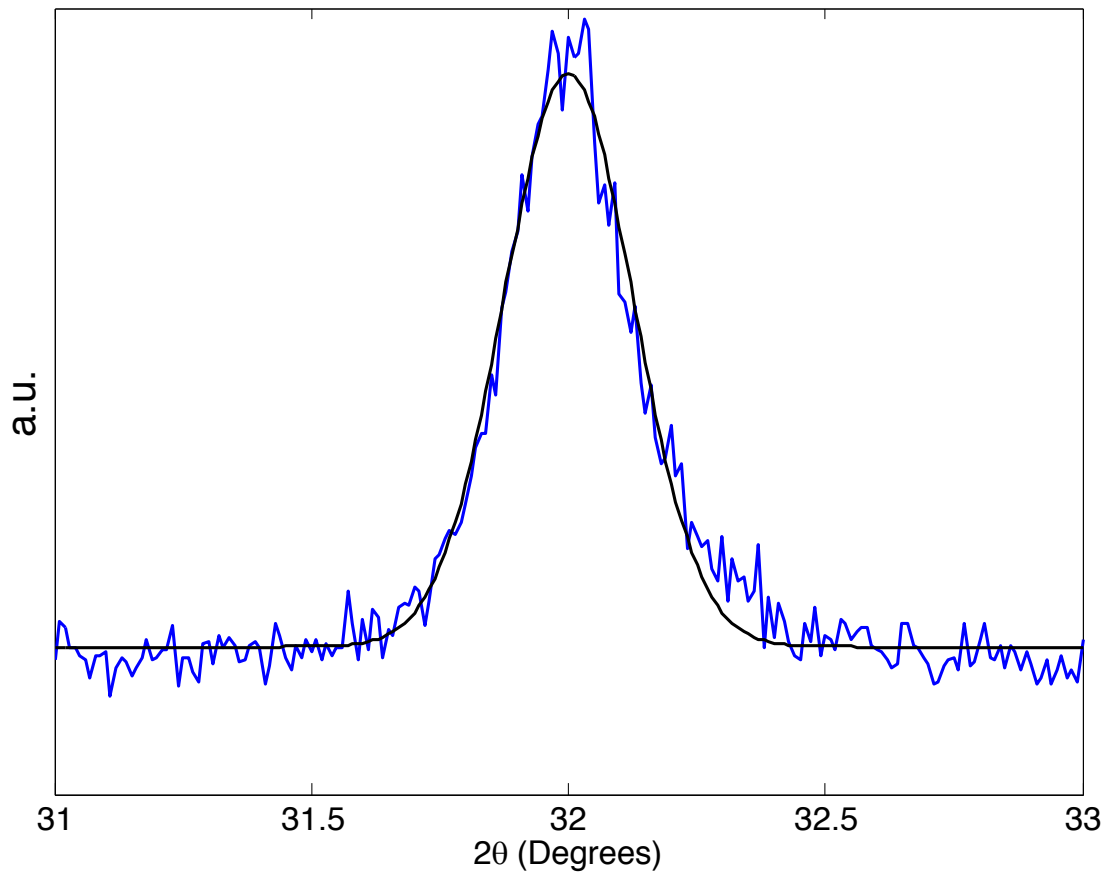

Figure 2.8: Gaussian fit of XRD 2θ scan for sample R490 with 37%S.

Using Bragg's law, the d-spacing was calculated:

$$n\lambda = 2dsin\theta. \tag{2.1}$$

The lattice parameter, c, was found using the d-spacing relation for hexagonal structures.

$$\frac{1}{d^2} = \frac{4}{3}\left(\frac{h^2+hk+k^2}{a^2}\right) + \frac{l^2}{c^2} \tag{2.2}$$

Since all of the $ZnO_{1-x}S_X$ samples were textured along (0002), Equation 2.2 simplifies to

$$\frac{1}{d^2} = \frac{l^2}{c^2} \,. \tag{2.3}$$

The concentration of substitutional sulfur in ZnO (or O in ZnS) was calculated from shifts in the XRD (0002) peak using a linear extrapolation of the lattice parameter between that of wurtzite ZnO (c=0.52 nm) and ZnS (c=0.626 nm) known as Vegard's law (Equation 2.4). Note that this may be different from RBS concentration which measures the total elemental composition in the films.

$$c_{ZnOS} = c_{ZnS}x + c_{ZnO}(1 - x) \tag{2.4}$$

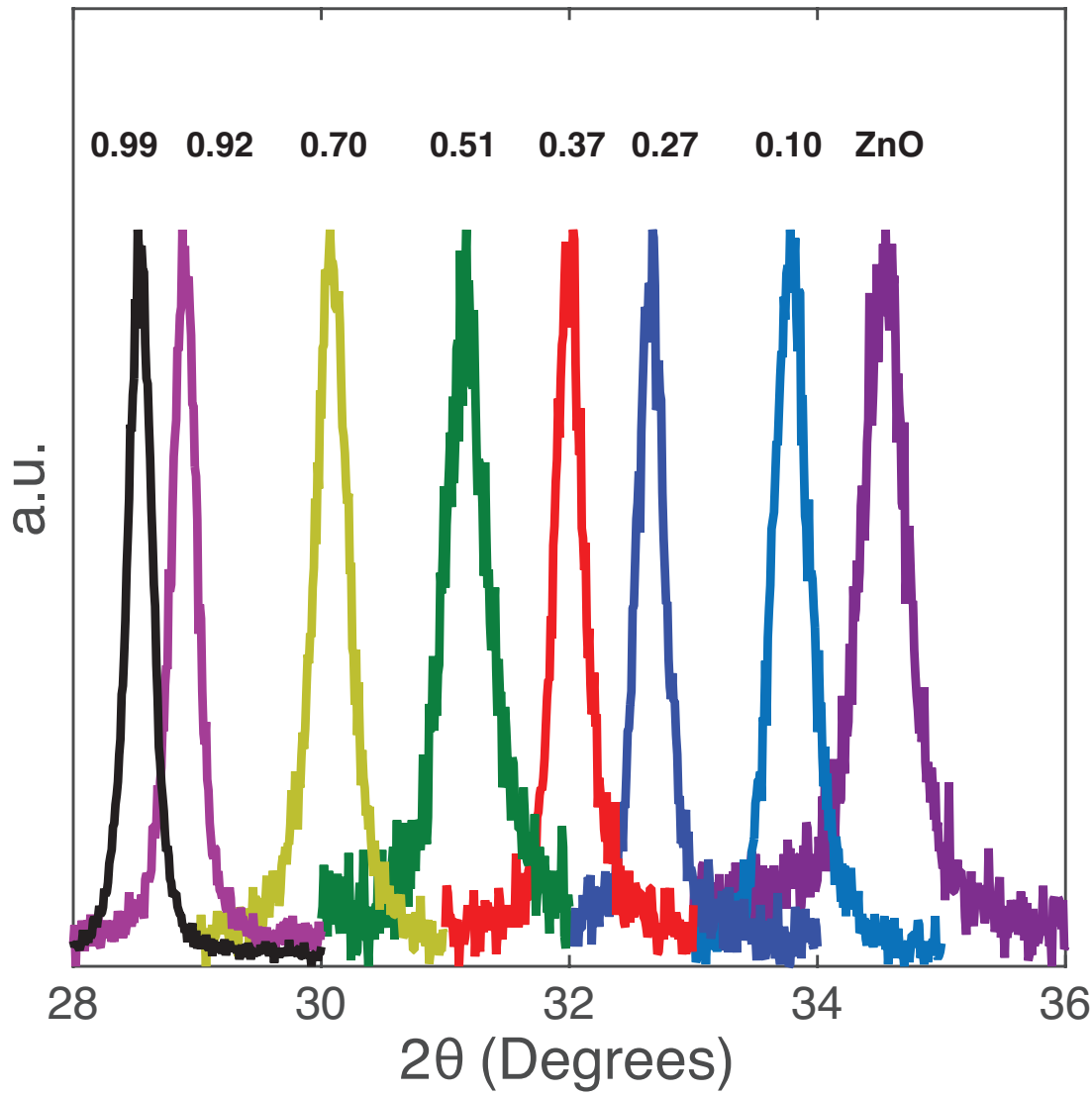

Figure 2.9: Normalized XRD (0002) diffraction peak of $ZnO_{1-x}S_x$ alloys over nearly the entire composition range (x from 0 to 0.99). The composition listed on the diffraction peaks was found using Vegard's law.

The concentration of sulfur determined through RBS and XRD using Vegard's law are compared in Figure 2.10. The good agreement of alloy composition measured by XRD and RBS suggests that all the samples are, indeed, random alloys with S and O in the group VI sublattice.

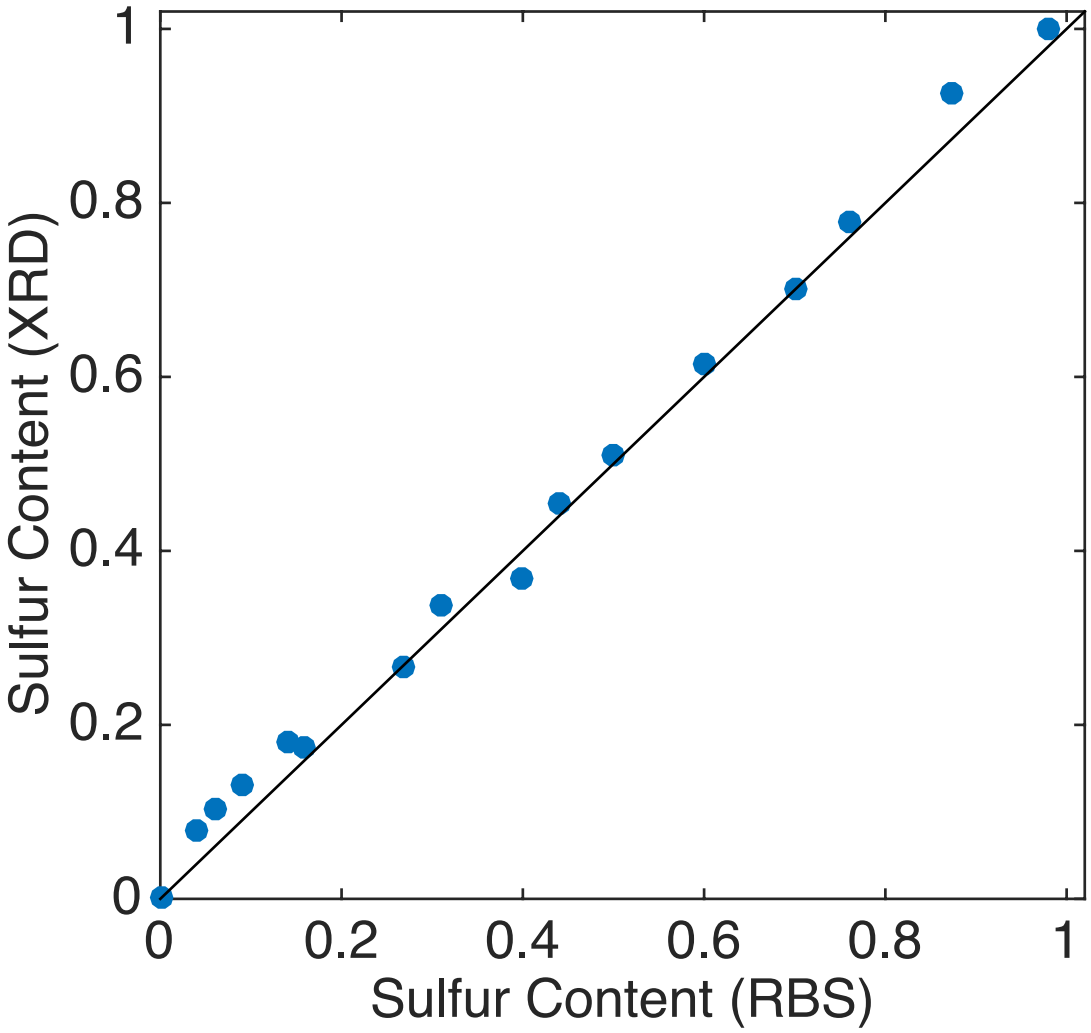

Figure 2.10: Comparison between RBS and XRD calculated concentration of sulfur.

2.4.2 Transmission Electron Microscopy and Energy Dispersive X-Ray Spectroscopy

Transmission electron microscopy and scanning TEM experiments were performed on four samples listed in Table 2.1 using an FEI Titan microscope operating at 300 kV. Standard cross-section thin foils were prepared by mechanical thinning and dimpling followed by Ar^+ ion polish at 6°. A final polish using 0.5 keV at 2° was performed before the samples were analyzed. Conventional TEM Micrographs were acquired with a Gatan UltraScan 1000 camera, while Selected Area diffraction patterns were recorded using a Gatan Orius 830. SAD patterns were analyzed using MATLAB custom codes for STEM images. The scattered electrons were captured by a Fischione Model 3000 ADF detector. Energy dispersive X-ray (EDX) spectra were collected using an FEI SuperX quad windowless detector based on silicon drift technology with a solid angle of 0.7 steradians for about 10 min. EDX data processing was performed by using elemental K_α-lines applying Cliff-Lorimer approach within the Bruker ESPRIT® software. This method is based on the intensities of measured peaks of L-lines relative to calculated or measured intensities of standards.

Table 2.1: Sulfur content measured through RBS for the four samples studied using TEM

Sample	x (sulfur content)
1	0.04
2	0.44
3	0.76
4	0.98

Transmission electron microscopy reveals a crystalline film with a columnar-like structure that remains throughout the entire composition range. A size reduction of the column together with an increase of planar defects is observed as the S content increases (Fig. 2.11). Energy dispersive X-ray spectroscopy shows atomic species uniformly distributed through the layers, consistent with the XRD and RBS results that all the samples are, indeed, random alloys with S and O in the group VI sublattice (Fig. 2.12).

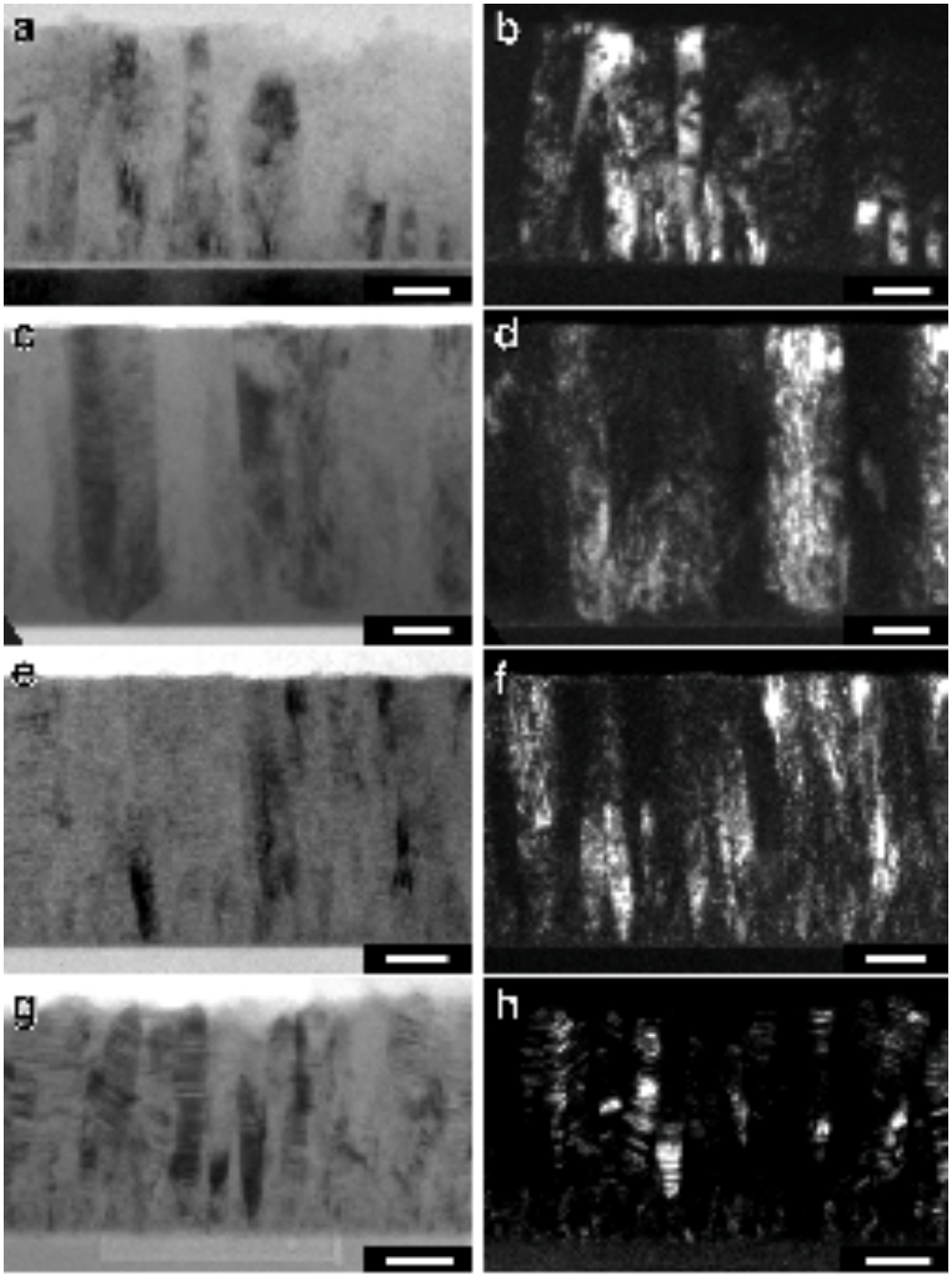

Figure 2.11: Pairs of Bright- and Dark-Field micrographs of the samples 1 to 4. (a)–(b) correspond to the sample with x=0.04 S content, (c)–(d) to the sample with x=0.44 S content, (e)–(f) to the sample with x=0.76 S content (g)–(h) to the sample with x=0.98 S content. A columnar-like structure is observed for the whole range of composition x of the synthesized $ZnO_{1-x}S_x$ layers with a considerable increasing of column size for the sample with an intermediate composition x = 0.44. Bar scales are 20 nm for (a)–(b) and 40 nm for (c)–(h).

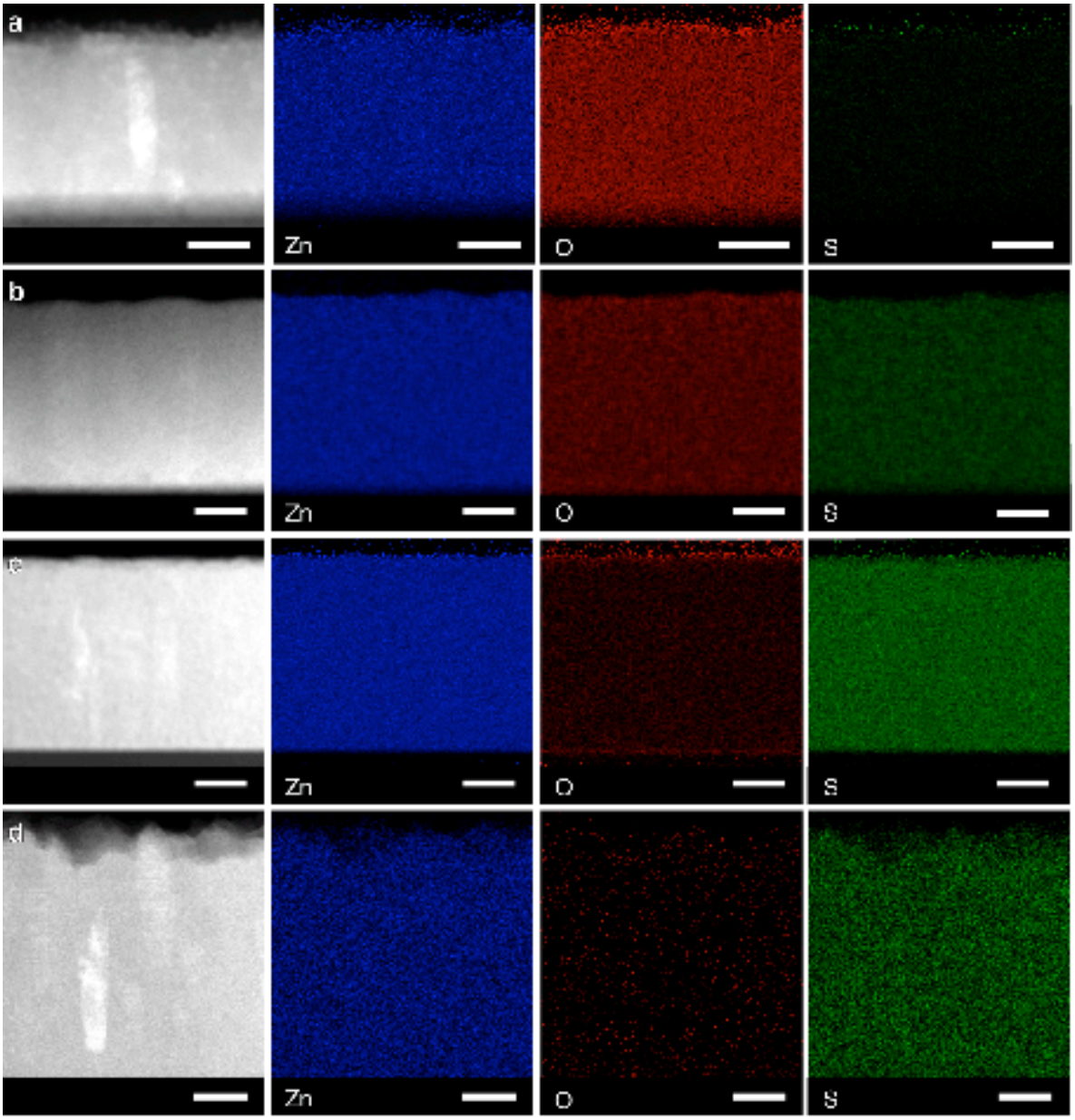

Figure 2.12: EDX element mapping for the detected 3 elements, Zn, O, and S, respectively, columns 2 to 4, alongside with simultaneously acquired HAADF survey image. (a) correspond to the sample with x=0.04 S content, (b) to the sample with x=0.44 S content, (c) to the sample with x=0.76 S content, and (d) to the sample with x=0.98 S content.

Chapter 3

3 Optical and Electronic Properties of $ZnO_{1-x}S_x$ Films

This chapter presents the optical and electronic properties of $ZnO_{1-x}S_x$ films grown through PLD and RF magnetron sputtering as discussed in Chapter 2. Optical absorption (Section 3.1) and photoreflectance spectroscopy (Section 3.2) are used to characterize the optical properties of the alloys. Shifts in the valence band were probed with X-ray Photoelectron Spectroscopy (XPS) in Section 3.3. Section 3.4 combines the results of the optical characterization with the band anticrossing model to determine the band structure of the $ZnO_{1-x}S_x$ alloys. Finally, Section 3.5 tests the performance of CdTe thin film solar cells with $ZnO_{1-x}S_x$ buffer layers.

A better understanding of the band structure and offsets with other semiconductors is essential for device applications using these $ZnO_{1-x}S_x$ alloys. One potential application for these $ZnO_{1-x}S_x$ alloys is replacing the toxic cadmium sulfide (CdS) buffer layer in copper indium gallium selenide (CIGS) and copper zinc tin sulfide (CZTS) solar cells. Various reports have replaced the CdS layer with $ZnO_{1-x}S_x$ alloys, but not knowing the position of the conduction band has made it difficult to choose a composition for the best conduction band alignment [53].

3.1 Optical Absorption Spectroscopy of $ZnO_{1-x}S_x$ Films

When a photon strikes a material, one of three processes occurs: 1) reflection: the photon is returned when it hits a surface or while it passes through the material 2) transmission: the photon passes through the material, 3) absorption: the photon is transformed to another form of energy by interacting with the material. One point to note: both reflection and transmission can be accompanied by scattering, the process of deflecting a unidirectional beam into many directions.

In semiconducting materials, the energy-dependent absorption coefficient is sensitive to optical transitions allowed between energy states. These allowed optical transitions can be due to direct and indirect interband transitions from filled valence bands and unfilled conductions bands. Therefore, in semiconductors photons with energies smaller than the bandgap (light with longer wavelengths) are transmitted through because they do not provide enough energy for the electrons in the valence band to reach the unoccupied states at the bottom of the conduction band.

For a semiconductor with parabolic bands which occur in most IV, II-VI and III-V semiconductors, and direct optically-allowed interband transitions, the absorption coefficient, $\alpha\ (E)$, is proportional to the square root of the photon energy, E :

$$\alpha\,(E) \;\propto\; \sqrt{E - E_g^{dir}}\,. \qquad (3.1)$$

Therefore, for simple cases, it is customary to estimate the direct bandgap, E_g^{dir}, of a material by linearly fitting the absorption coefficient squared $\alpha^2\,(E)$ vs. energy.

On the other hand, for some indirect semiconductors, the absorption coefficient is proportional to the photon energy squared:

$$\alpha\,(E) \;\propto\; \left[E - E_g^{indirect}\right]^2. \qquad (3.2)$$

For simple cases it is possible to estimate the indirect bandgap, $E_g^{indirect}$, by linearly fitting the square root of the absorption coefficient $\sqrt{\alpha\,(E)}$ vs. energy. There are instances when intermediate states in the bandgap (typically due to defects) lead to optical transitions that are less in energy than the optical bandgap of the semiconductor.

Being able to calculate the absorption coefficient can provide insight into direct, indirect and intermediate optical transitions in semiconductor materials. Assuming that the intensity of reflected, transmitted and absorbed light add up to the incident intensity, normalized to $I_0 = 1$; the absorption is calculated as:

$$\alpha(E) = 1 - T(E) - R(E)\,. \qquad (3.3)$$

Back-reflection from the film-substrate interface is not considered here. Since these films were grown on transparent substrates and the film thickness d << substrate thickness it was possible to treat the substrate as an infinite substrate. Modeling the system as a single layer that absorbs, the absorption coefficient of the film can be calculated using the following relation

$$T(E) = [1 - R(E)]\exp\,(-\alpha(E)\,d). \qquad (3.4)$$

Solving for $\alpha(E)$ leads to:

$$\alpha(E) = -\frac{1}{d}\,ln\left[\frac{T(E)}{1-R(E)}\right]\,. \qquad (3.5)$$

3.1.1 Optical Absorption Properties of $ZnO_{1-x}S_x$

From Equation 3.5, the absorption coefficients $\alpha(E)$ of the alloy films were obtained using transmission and reflection spectra taken from a Perkin-Elmer Lambda 950 Spectrophotometer in the spectral range of 250nm-2500nm. Reflectance data was collected at 8° from the direction of the surface normal.

Bandgaps of alloys with compositions in the range of 0.16<x<0.9 were estimated by the extrapolation of the square of $\alpha(E)$ assuming parabolic dispersion relations. One example plot with the linear extrapolation of $\alpha^2(E)$ is shown in Figure 3.1 to determine the bandgap for a sample with x=0.87. The absorption spectra for samples grown by RF magnetron sputtering with sulfur <0.27 or oxygen <0.11 films are shown in Fig. 3.2. The incorporation of sulfur into the ZnO matrix results in a shift of the absorption edge from ultraviolet into the visible spectrum in Fig. 3.2(a) and is indicated by the arrow. On the other hand, incorporation of O into ZnS matrix leads to a red shift in the absorption edge in Fig. 3.2(b) also indicated by the arrow. The bandgaps of the dilute sulfur (oxygen) samples were determined by fitting the absorption coefficient spectra using the valence BAC [24] and the conduction BAC [54] model, respectively.

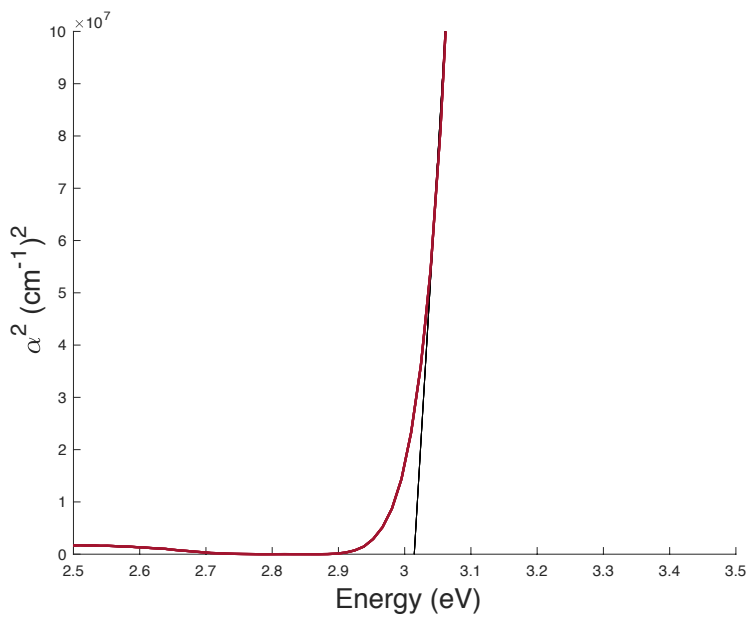

Figure 3.1: Sample plot with linear extrapolation of $\alpha^2(E)$ used to determine the bandgap of a sample with x=0.87.

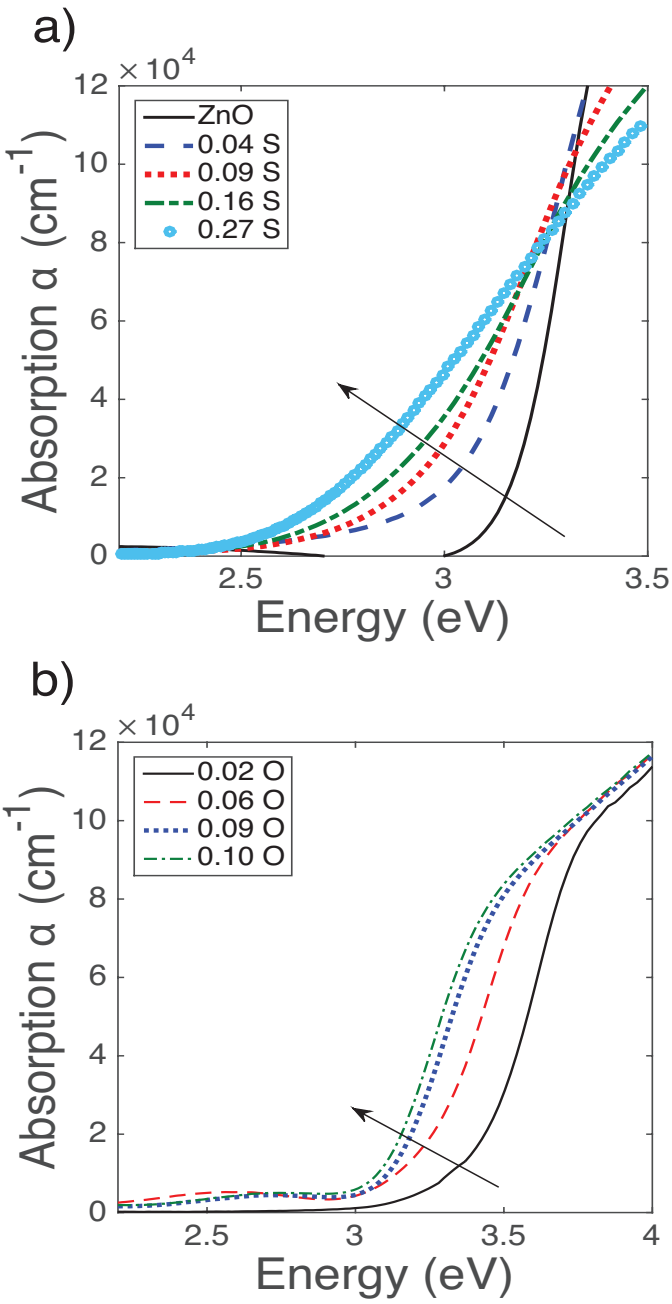

Figure 3.2: (a) Absorption spectra for select films with dilute sulfur in a ZnO matrix. The arrow indicates the direction the absorption edge shifts with the increase in sulfur content. (b) Absorption spectra for select films with dilute oxygen in a ZnS matrix. The arrow indicates the direction the absorption edge shifts with an increase in oxygen content. The compositions listed were found through RBS. These films were grown by rf magnetron sputtering.

3.2 Photomodulated Reflectance (PR) Spectroscopy

In the method of photomodulated reflectance (PR) spectroscopy, modulation of the electric field of the sample is caused by photo-injection of electron-hole pairs. In order to create electron-hole pairs, the energy of photons in the pump beam must exceed the bandgap of the material. PR spectroscopy provides a direct measure of interband transitions in semiconductors. PR has been instrumental in providing evidence for the BAC model by being able to measure both E_+ and E_- transitions [55].

The PR spectra are shown in Figure 3.3 for the $ZnO_{1-x}S_x$ films. The $ZnO_{1-x}S_x$ films that were measured with PR were grown on ZnSe substrates by RF magnetron sputtering to minimize the refractive index contrast at the film and substrate interface and thus reduce Fabry–Perot oscillations. Large Fabry–Perot oscillations were observed on $ZnO_{1-x}S_x$ films grown on glass and sapphire substrates, therefore PR signals were not visible.

PR spectra were measured at T=10 K (black line) and at T=300 K (purple line). All possible spectra have been fitted (see red line in Figure 3.3) using Aspnes' critical point (CP) model described in ref [55], [56] given by equation

$$\frac{\Delta R}{R} = Re\left[Ce^{i\theta}\left(E - E_g + i\Gamma\right)^{-n}\right]. \qquad (3.6)$$

Where $\frac{\Delta R}{R}$ is the energy dependence of the PR signal, C and θ are the amplitude and phase of the resonance which determine the amplitude and asymmetry of the line shape, and E_g and Γ are the energy and the broadening parameter of the optical transition. The term n depends on the nature of the optical transition, specifically the type of critical point: for an excitonic transition n = 2, for a three-dimensional one electron transition, n = 5/2, and for a two-dimensional one electron transition m = 3 [56]. For the fits shown in Figure 3.3, n is assumed to be n = 2.5 as it corresponds to the band-to-band transition [55].

In the 10 K spectra, signal from the ZnSe substrate can be observed. For two samples with composition of x=0.62 and x=0.8) measured at 10 K, signal from the film layer could not been resolved due to overlap with the strong signal from the ZnSe substrate (grey line 2.8 eV at 10 K). Also for two samples with x=0.44 and x=0.98) measured at 300 K, signal related to an interband transition could not been observed. All measurements were performed with a laser excitation line of 266nm.

There is a clear redshift in the transition energy with increased sulfur alloying up to x=0.44 as show in Figure 3.4. For sulfur contents of x>0.44 there is a clear blue shift in the interband transition energy. This is in agreement with the absorption coefficient results shown in Figure 3.2. From the interband transitions measured from PR as a function of sulfur content in Figure 3.4, it can be seen that there is noticeable bowing.

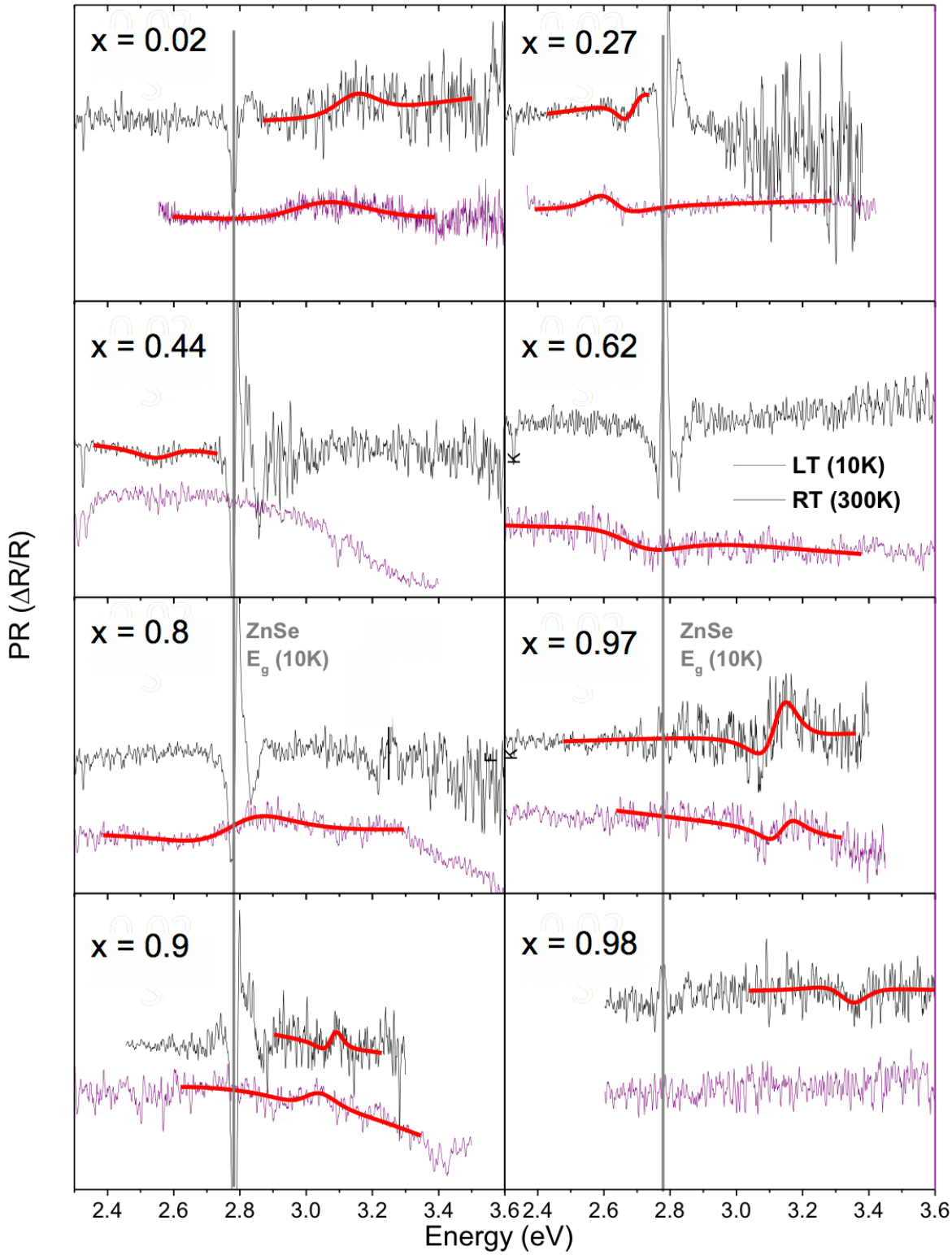

Figure 3.3: PR results for $ZnO_{1-x}S_x$ films grown on ZnSe substates grown by RF magnetron sputtering.

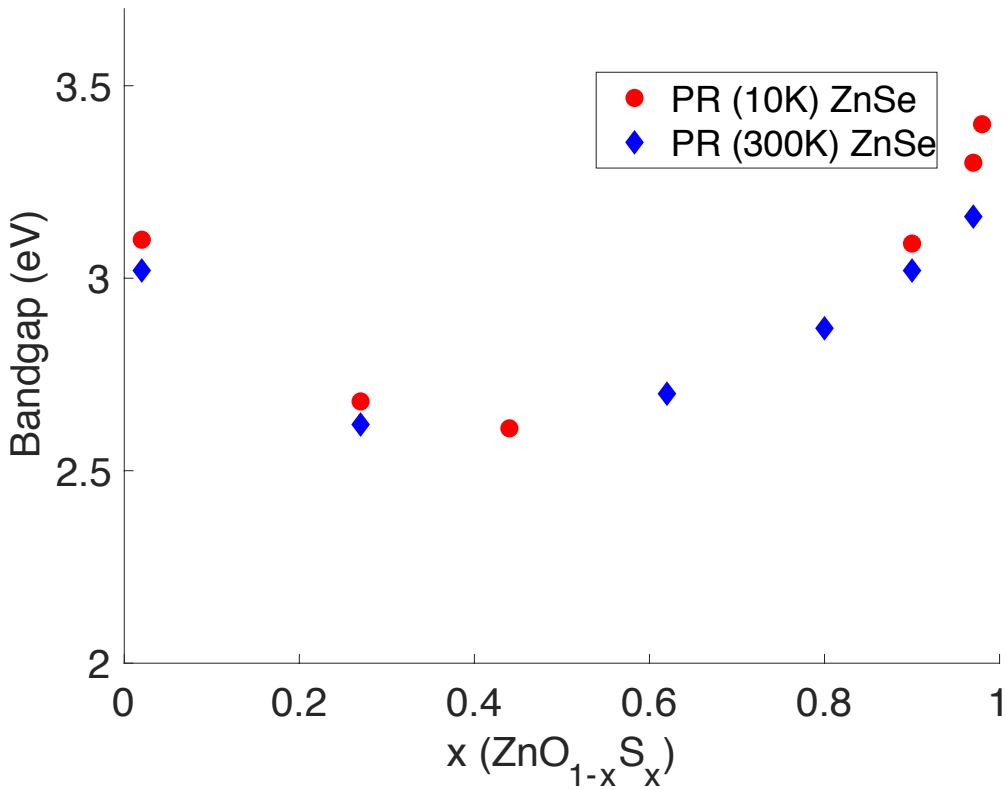

Figure 3.4: Bandgap determined from PR measurements versus sulfur content determined by RBS.

3.3 X-Ray Photoelectron Spectroscopy

X-ray photoelectron spectroscopy (XPS) is a surface sensitive technique that measures the photo- induced ejection of electrons to probe the filled electronic states of a material. It does this by irradiating the sample surface with low energy X-rays. The x-rays excite the electrons of the sample and if the binding energy is lower than the X-ray energy, the electrons will be ejected as a photoelectron. Only photoelectrons at the surface can escape the surface of the sample (typically 10-100 Angstroms), therefore making this technique surface sensitive. The XPS measurements taken on the $ZnO_{1-x}S_x$ samples were used to probe the elemental core levels (O1s, Zn2p, and S2p) and changes in the valence band structure.

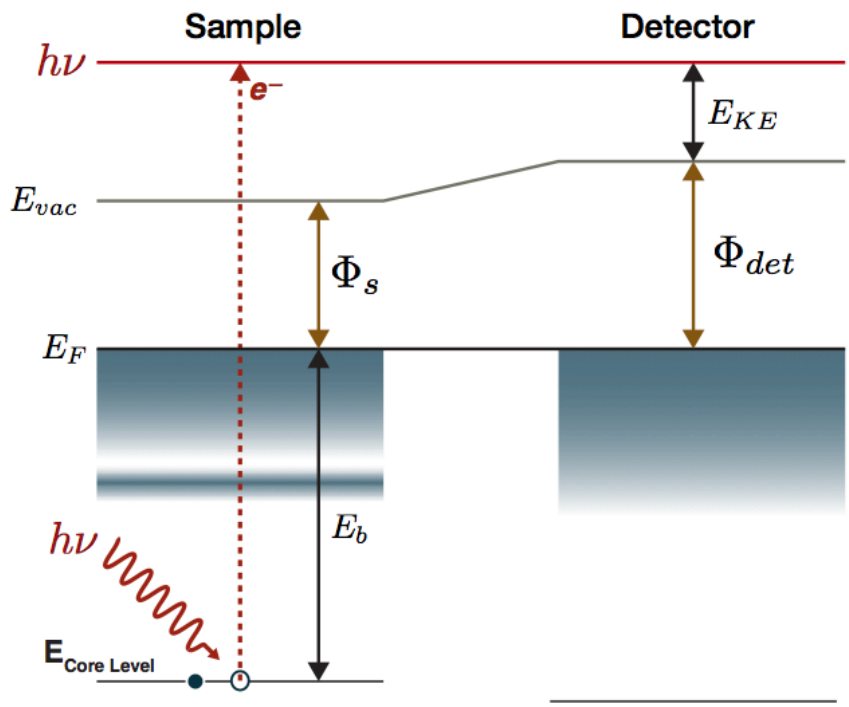

Figure 3.5: Schematic of XPS showing how the sample and detector are connected in order to measure the binding energy of states in a sample.

In standard XPS measurements, the sample and detector are in electrical contact with each other, causing a constant E_F (Figure 3.5). The binding energy is calculated with the following relation

$$E_b = h\nu - (E_{KE} + \Phi_{det}), \qquad (3.7)$$

where hν is the incident X-ray photon energy, E_{KE} is the measured kinetic energy of the ejected photoelectrons, and Φ_{det} is the detector work function ($\Phi_{det} = E_{vac} - E_F$).

3.3.1 Composition Calculation Using XPS

To calculate the surface composition using XPS, the Zn2p3/2 and the S 2p3/2 photoemission intensity peaks were normalized with atomic cross sections using the following relation

$$\frac{N_S}{N_{Zn}} = \frac{I_{s(s2p3/2)}\sigma_{Zn2p3/2}}{\sigma_{s2p3/2}I_{Zn(Zn2p3/2)}} = x, \qquad (3.8)$$

where $I_{s(s2p3/2)}$ is the peak area of the s2p3/2 peak, $\sigma_{s2p3/2}$ is the atomic cross section for sulfur, $I_{Zn(Zn2p3/2)}$ is the peak area of the Zn2p3/2 peak and $\sigma_{Zn2p3/2}$ is the atomic cross section for zinc.

3.3.2 XPS of $ZnO_{1-x}S_x$ Films

A few samples with $x \leq 0.27$ grown by RF magnetron sputtering were examined by XPS in order to verify shifts in the valence-band maximum and to estimate the sulfur composition with the relative intensities between the Zn2p and S2p peaks. XPS spectra were measured using a monochromated Al K_α X-ray source ($h\nu$ = 1486.6 eV) with a Kratos Axis Ultra DLD hemispherical electron analyzer. XPS spectra were charge corrected to the adventitious C1s spectral component binding energy set to 284.8 eV [57].

In order to characterize the effects of sulfur incorporation on the electronic structure of the $ZnO_{x-1}S_x$ alloys, valence-band spectra were collected by XPS for a range of compositions from pure ZnO to 0.27 sulfur as measured by RBS (see Fig. 3.7). The pure ZnO material has the top of the valence band composed of O2p states. The introduction of sulfur in the alloys causes a shift of the valence band closer to the Fermi level with increasing S concentration as well as a depression in the slope of the band edge. Comparing the spectra measured for ZnO and the alloy films in Fig. 3.6(b), one sees that S incorporation into the ZnO lattice increases the intensity of the S 2p peaks without any appreciable energy shift. The Zn2p peaks in Fig. 3.6(a) do not broaden or shift in energy for the samples measured, indicating that the upward shifting of the valence band is due to the incorporation of S and not defects [21].Therefore, as the sulfur concentration increases, the density of states increases above the valence band of ZnO [22]. The surface sensitivity of XPS allows to relate the observed shifts to a common energy reference since the Fermi level at the surface of each sample is located at the Fermi Level stabilization energy (E_{FS}), ~4.9 eV below vacuum level in all semiconductors [39]. Since the conduction band minimum of ZnO is located close to $E_{FS,}$ the binding energy measured through XPS is close to the bandgap of ZnO. The relative VBE position is taken from linearly extrapolating the XPS valence band spectra edge from Figure 3.7 and a sample fit is shown in Figure 3.8.

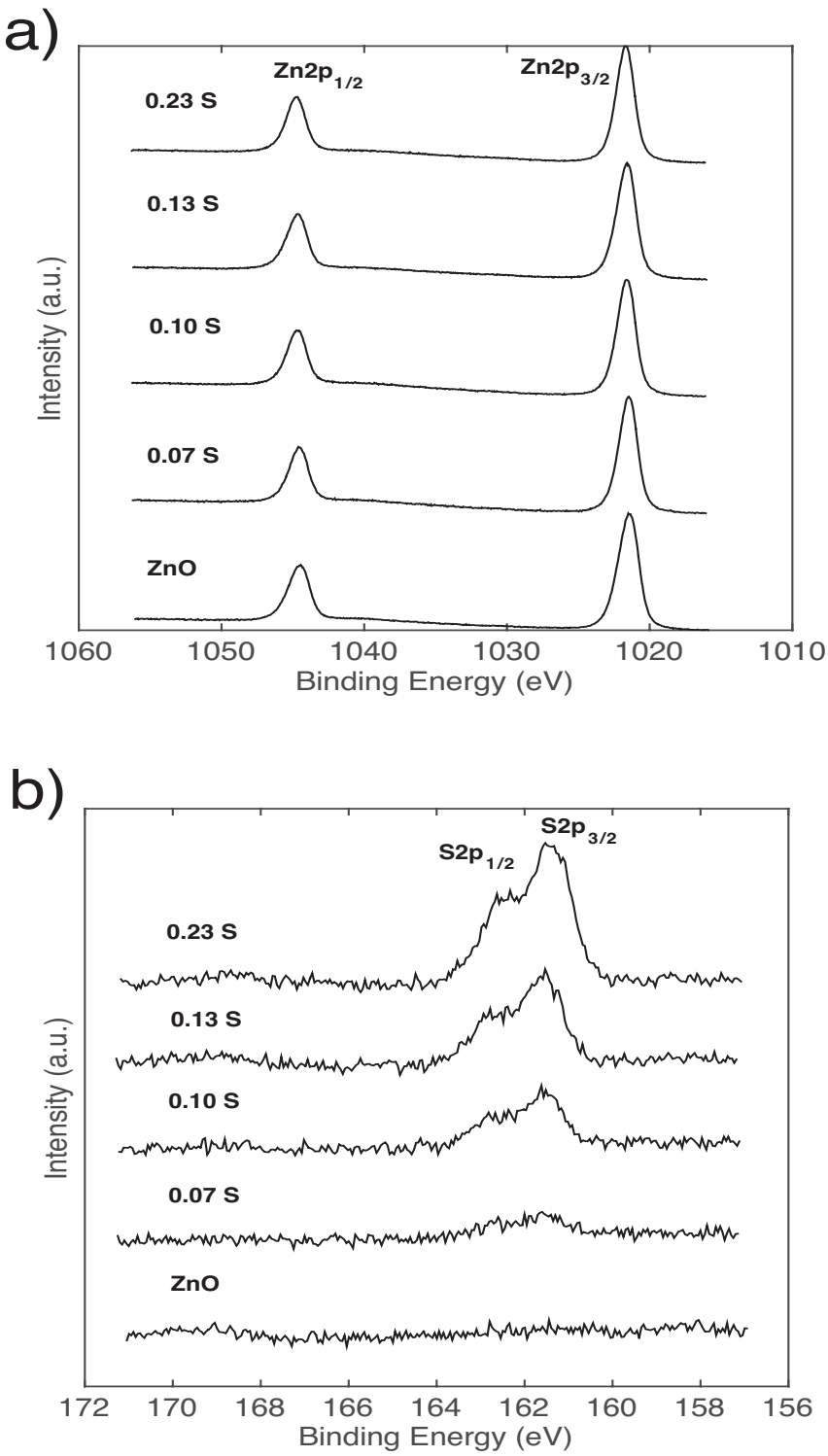

Figure 3.6: (a) XPS Zn2p spectra of several films with labeled sulfur content, (b) XPS S2p spectra of several films with labeled sulfur content. The composition listed is the surface composition found using the Zn2p and S2p XPS spectra.

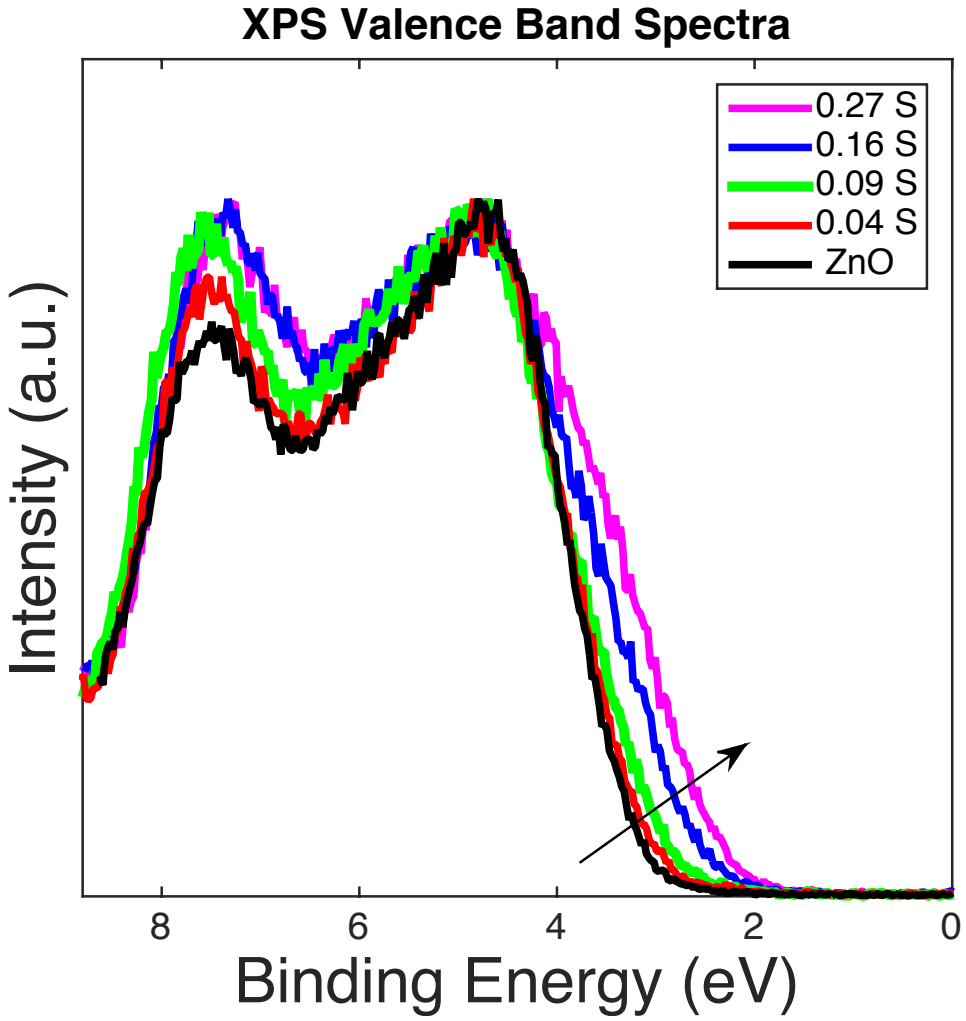

Figure 3.7: XPS valence band spectra for x ≤ 0.27, the compositions listed were found through RBS. The arrow indicates the monoatomic upward shift in the valence band as sulfur content increases.

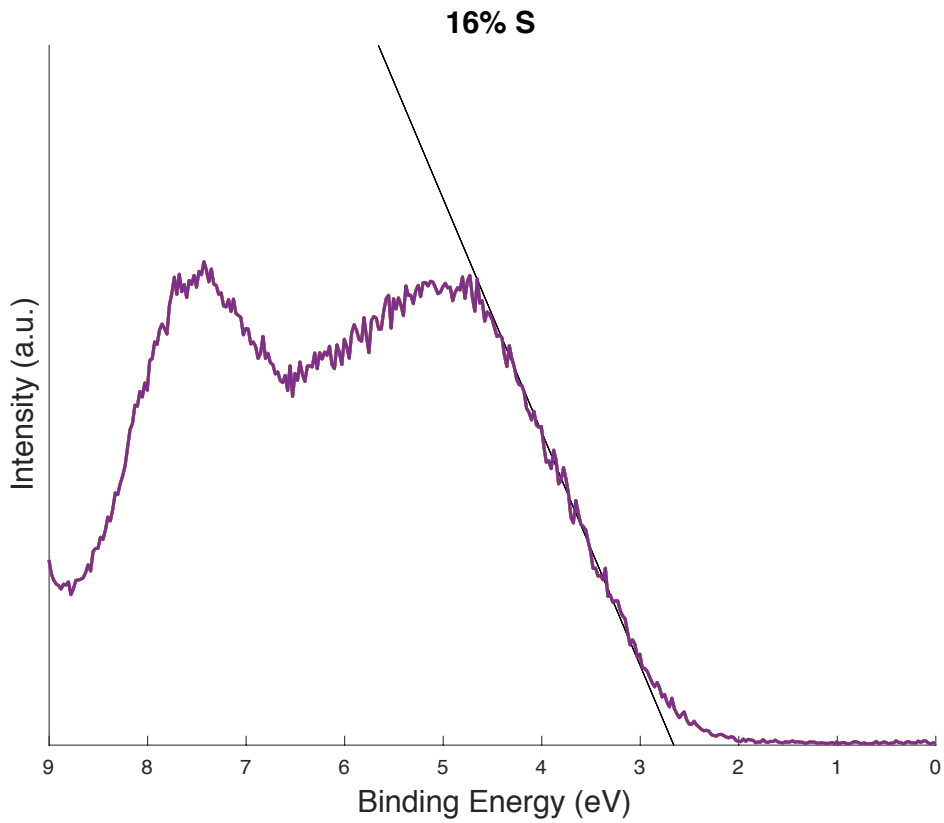

Figure 3.8: Sample plot with linear extrapolation of XPS valence band spectra edge used to determine the binding energy a sample with x=0.16.

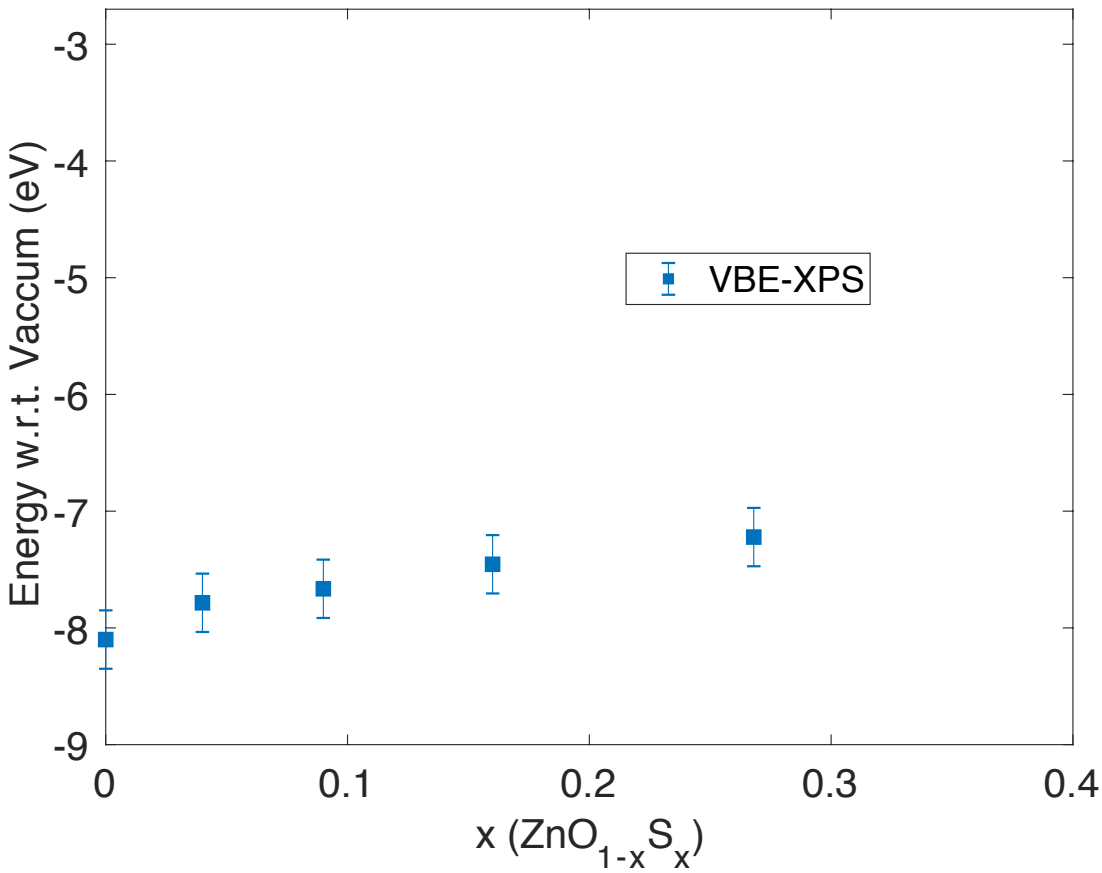

Figure 3.9: The VBE positions determined from linearly extrapolating the XPS valence band spectra. The VBE positions are plotted with respect to vacuum level.

Taking the relative VBE positions from linearly extrapolating the XPS valence band spectra, it was possible to plot them with respect to the vacuum level. The valence band position was assumed to be ~ -8.1 eV as found in the collected band offsets of various semiconductors (found in Appendix A).

3.4 Band Anticrossing in $ZnO_{1-x}S_x$

The absorption spectra for samples with sulfur <0.27 or oxygen <0.11 films are shown in Fig. 3.2. The incorporation of sulfur into the ZnO matrix results in a shift of the absorption edge from ultraviolet into the visible spectrum (Fig. 3.2(a)). Substituting S into the O sublattice in ZnO introduces a localized level close to the valence band edge of ZnO. The interaction of the localized S level with the extended valence-band states of ZnO results in valence BAC (VBAC) effect when a significant amount of S atoms are incorporated into the lattice. When this occurs, the valence band splits into two subbands ($E_+$and E_-). On the other hand, the incorporation of O into ZnS matrix leads to a red shift in the absorption edge (Fig. 3.2(b)). In this case, oxygen forms a localized level at ~0.2eV below the conduction band of ZnS [23], resulting in conduction BAC (CBAC),

splitting the conduction band into two subbands (E_+ and E_-). These anticrossing effects at the dilute sulfur (dilute oxygen) compositions produce narrow, non-parabolic S (O) derived bands with the total number of states dependent on the S (O) content. Hence, estimating the bandgap of these alloys using the conventional method of extrapolating α^2 to zero will result in significant error. Here, we adopt the procedure based on the BAC model previously used to fit absorption curves in $ZnO_{1-x}Se_x$ and $ZnO_{1-x}Te_x$ HMA [16], [24].

3.4.1 Valence Band Anticrossing of $ZnO_{1-x}S_x$ Dilute Sulfur Films

As mentioned previously, the valence BAC effect occurs when sulfur substitutes oxygen in the ZnO rich side. We adopt the simplified version of the valence BAC [24] that represents the BAC model given by equation (1.4). In this case, E_d is the energy of the localized S level above the ZnO valence band edge, $E(k)=E_V(k)$ is the ZnO matrix valence band dispersion, $C=C_{VB}$ is the coupling parameter, and x is the S composition. We take into consideration optical transitions from 3-fold degenerate valence bands including the spin orbit split off band to the conduction band with the spin orbit splitting energy of S [25]. Therefore to calculate the absorption coefficient, we consider three optical transitions: the S derived band to conduction band [$E_+(k)$], the S spin orbit split band to conduction band [$E_{+SO}(k)$], and the heavy and light hole derived bands of the ZnO matrix to conduction band [$E_-(k)$].

The optical joint-density of states (JDOS) were convolved with a Gaussian function at each wave vector, k, an approach used in [17] to account for the broadening in the bands. Therefore, the optical absorption coefficient from a single valence band (VB), e.g. $[E_+(k)]$, can be written as an integral of the JDOS with respect to k:

$$g_+(\hbar\omega) = \int_{-\frac{\pi}{a}}^{\frac{\pi}{a}} \left[-\sin\left(\frac{\theta(k)}{2}\right)\right]^2 \frac{1}{\Delta_+\sqrt{2\pi}} \exp\left(-\frac{(\hbar\omega-[E_C(k)-E_+(k)])^2}{2\Delta^2}\right) k^2 dk, \qquad (3.9)$$

where $g_+(\hbar\omega)$ is in terms of the number of states per unit volume per unit frequency, $E_C(k)$ is the conduction band (CB) dispersion, the first term under the integral represents the fraction of the contribution of the delocalized states to the optical transition, where

$$\theta(k) = \tan^{-1}\left(\frac{2C\sqrt{x}}{E_d-E_V(k)}\right), \qquad (3.10)$$

and Δ_+ is the broadening parameter. The limits of integration are from $\frac{\pi}{a}$ to $-\frac{\pi}{a}$ (in units of cm^{-1}), which represents the first Brillouin zone, where a is the lattice constant. The expression for the calculated total absorption coefficient includes the three transitions discussed above, with each transition weighted by their degeneracy factor:

$$\alpha(\hbar\omega) = \alpha_0\left[\frac{2}{3}g_+(\hbar\omega) + \frac{1}{3}g_{+,so}(\hbar\omega) + g_-(\hbar\omega)\right], \qquad (3.11)$$

where α_0 is an overall scaling constant. The coupling parameter, C_{VB}, scaling constant, α_0, and E_S were found by fitting the absorption curve of the sample with the lowest sulfur content. This approach was used, since the highest anti-crossing interaction is expected at low sulfur content.

These three values were kept constant for the remaining samples to find the broadening parameters for each transition (Δ_+, Δ_-, Δ_{+SO}). The best-fit broadening parameters were found by minimizing the root mean square error between the experimental absorption curve and the calculated absorption.

Figure 3.10 shows the experimental result and the fitting of the absorption coefficient using the VBAC for the 0.04 sulfur film, which also shows the three optical transition contributions. These fittings were done for all the dilute sulfur samples and it was possible to extract the sulfur level, E_S, of 0.30 eV above the valence band edge of ZnO and the coupling parameter, C_{VB} of 0.60 eV. These values are consistent with previous reports on $ZnO_{1-x}Se_x$ where the selenium level was found to be 0.90 eV above the ZnO valence band edge, and the coupling parameter was found to be 1.2eV [24]. Since the difference in electronegativity and ion size is smaller between sulfur and oxygen than the difference between selenium and oxygen, a smaller coupling parameter is expected. Using the coupling parameter, and the sulfur level, it was possible to calculate the band structure (Fig. 3.11) and determine the bandgap of the $ZnO_{1-x}S_x$ alloys from the maximum of the E_+ subband to the conduction band minimum. The observed upward shift of the VB edge is in a good agreement with the XPS data of Fig. 3.7 that clearly shows an appearance of additional density of states above the VB edge of ZnO. This method for calculating the bandgap was used for samples with sulfur content less than 0.14.

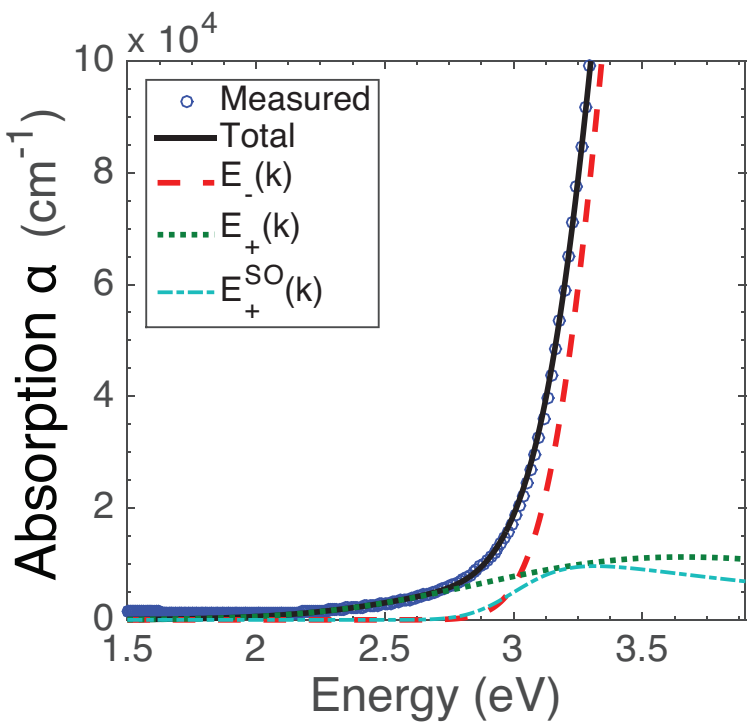

Figure 3.10: Measured absorption spectra for 0.04 sulfur film (determined by RBS) and the calculated theoretical fit using the VBAC model. The separate absorption contributions are also

shown. The sulfur level is 0.30 eV above the ZnO valence band and the coupling parameter, CVB, is 0.60eV.

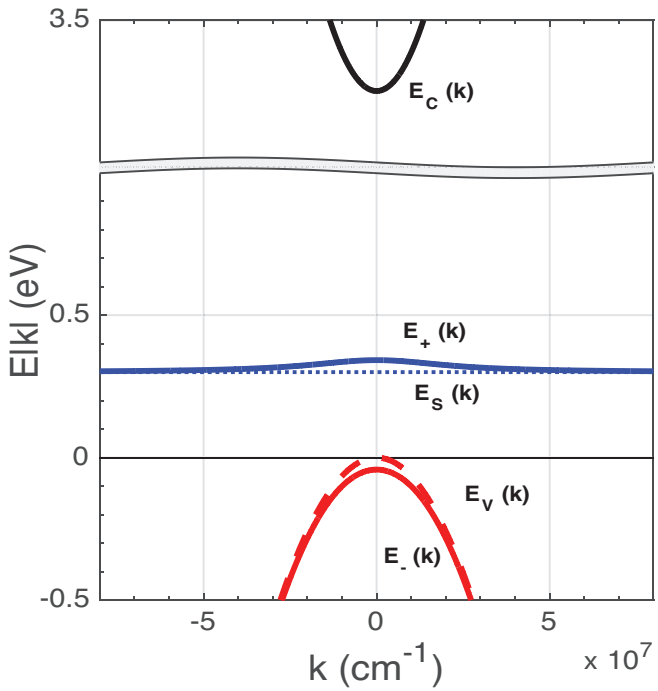

Figure 3.11: Calculated band structure for the 0.04 sulfur film.

3.4.2 Conduction Band Anticrossing of $ZnO_{1-x}S_x$ Dilute Oxygen Films

The CBAC effect was used to obtain the composition dependence of the bandgap for $ZnO_{1-x}S_x$ samples with dilute amount of O substituting S. In this case, E_d in Equation (1.4) is the energy of localized O level E_O, $E(k)=E_c(k)$ is the ZnS matrix conduction band dispersion, $C=C_{CB}$ is the coupling parameter, and x is the O composition. Here we consider only two optical transitions: the valence band to the O derived band [$E_-(k)$], and the valence band to the ZnS matrix derived band [$E_+(k)$]. Therefore, the expression for the calculated total absorption coefficient includes the two transitions discussed above, with each transition weighted by their degeneracy factor:

$$\alpha(\hbar\omega) = \alpha_0[g_+(\hbar\omega) + g_-(\hbar\omega)], \qquad (3.12)$$

where α_0 is an overall scaling constant. By fitting the experimental absorption coefficient, a coupling parameter, C_{CB} of 1.50 eV was obtained. Note that the coupling parameter reported here is 10% larger than the value of C_{CB}=1.35 eV reported previously for dilute oxygen $ZnO_{1-x}S_x$ alloys [27]. The location of the localized O level was fixed to E_O=3.5eV above the ZnS valence band as previously found in [23]. Figure 3.12 shows the experimental result and the fitting of the absorption

coefficient using the conduction BAC for the 0.02 oxygen film (0.98 sulfur), which also shows the two optical transition contributions. Figure 3.13 shows the calculated band structure that was used to determine the bandgap of the $ZnO_{1-x}S_x$ alloys from the maximum of the E_+ subband to the conduction band minimum. This method for calculating the bandgap was used for samples with oxygen content less than 0.10 (sulfur content more than 0.90).

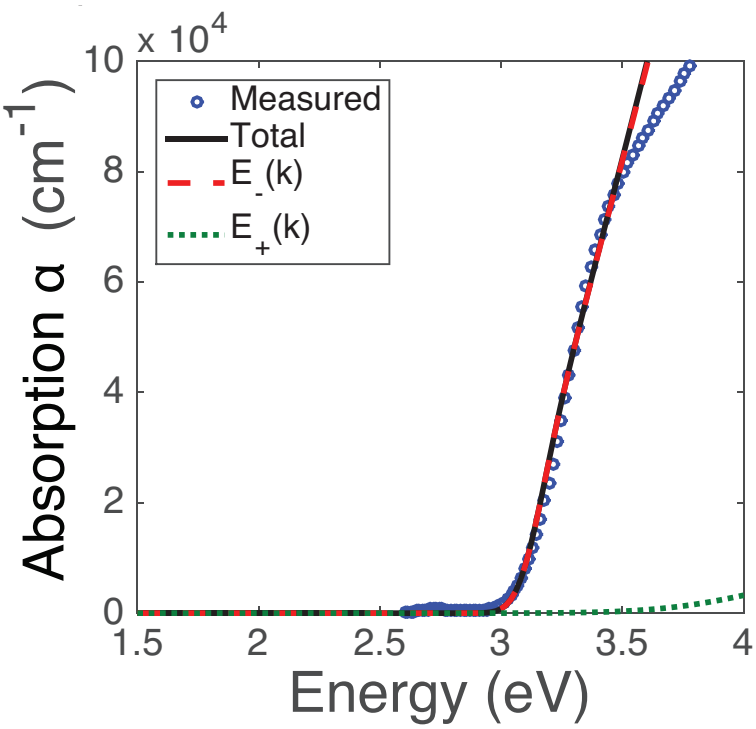

Figure 3.12: Measured absorption spectra for 0.10 oxygen film (determined by RBS) and the calculated total absorption using the CBAC model. The separate absorption contributions are also shown. The coupling parameter, C_{CB}, is 1.5 eV.

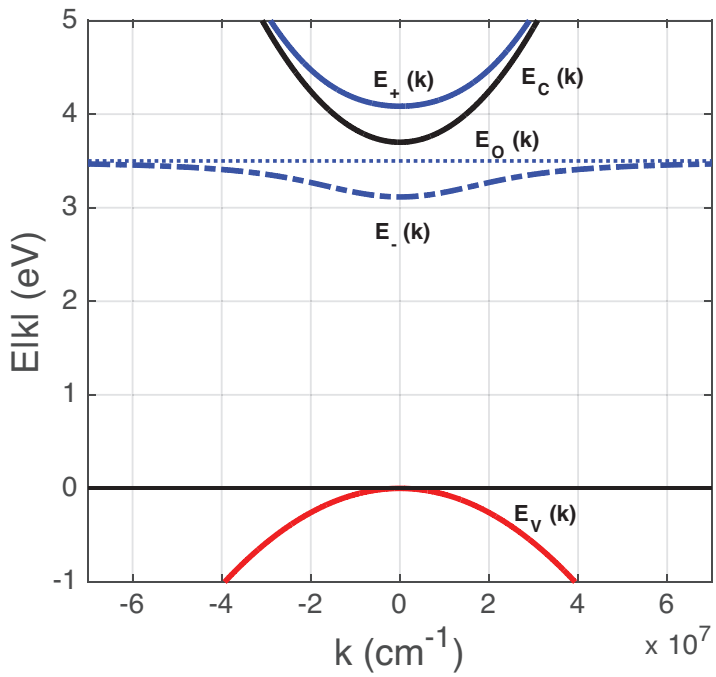

Figure 3.13: Calculated band structure for the 0.10 oxygen film (x=0.9).

3.4.3 Bandgap Dependence on Composition

Using the values of E_S, C_{VB}, and C_{CB} obtained in this work and the known E_O value, we also calculated the dependence of the conduction band and valence band edges of the $ZnO_{1-x}S_x$ alloys across the whole composition range. These calculations were performed using the compositional weighting method proposed in [28] and the results are shown in Fig. 3.14.

The BAC calculations show that the reduction in the bandgap of O-rich and S-rich $ZnO_{1-x}S_x$ films is due to the upward movement of the valence band and the downward movement of the conduction band, respectively. In Fig. 3.14(b), the bandgaps in this work are calculated from:

1) the absorption fitting using valence BAC for samples with sulfur x< 0.16 (blue filled circles).
2) linear extrapolation of the square of absorption coefficient (α^2) for samples with 0.16>x<0.90 sulfur (blue open circles)
3) the absorption fitting using conduction BAC for samples with x>0.90 sulfur (blue filled circles)
4) the PR results from Section 3.2 (green filled diamonds (10 K) and green unfilled diamonds (100 K))

The compositional weighting method is labeled as BAC since it utilizes the values E_S, C_{VB}, E_O, C_{CB}, determined through the absorption fittings described earlier. The bandgaps found in this work

are plotted alongside the experimental data found in [44] labeled as open black squares. It can be noted that in the dilute S region, the bandgaps reported in [44] deviate from the calculated BAC bandgap and the absorption fitting bandgaps. This indicates that using the standard method to determine the bandgap from the extrapolation of α^2 leads to significant error due to the non-parabolic dispersion of the S-derived at dilute S contents. In the middle region it is assumed that at higher sulfur content the S-derived band becomes more delocalized thus becoming more parabolic, making the standard method (α^2) valid in this region. There is good agreement between the BAC, α^2, and the values reported in [44].

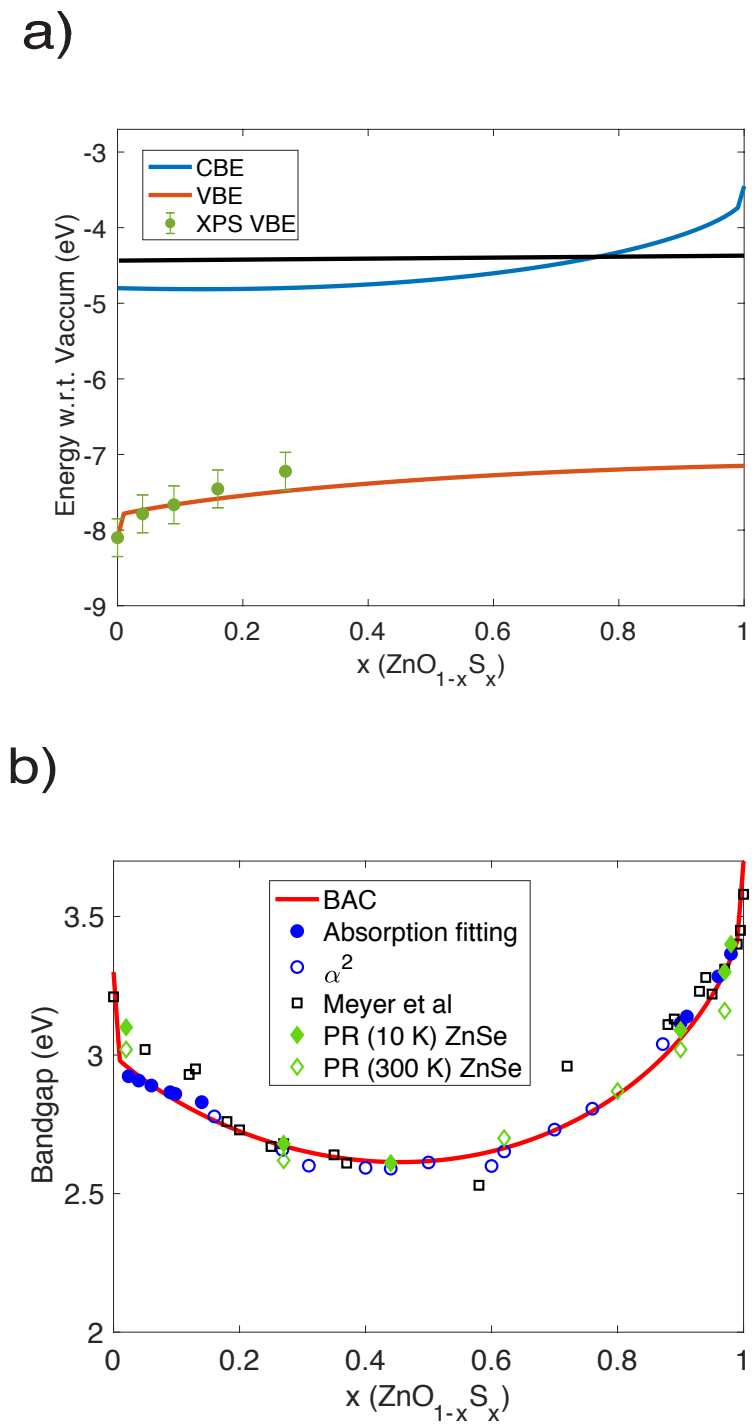

Figure 3.14: (a) Calculated conduction band and valence band edges. (b) Composition dependence of the bandgap of $ZnO_{1-x}S_x$ alloys. BAC line was determined by subtracting the calculated valence band edge from the calculated conduction band edge shown in (a). The experimental bandgaps found using the absorption fittings are plotted alongside the experimental data of Meyer et al [44].

3.5 $ZnO_{1-x}S_s$ as a Buffer Layer in CdTe Thin Film Solar Cells

These $ZnO_{1-x}S_x$ alloys are of interest as they offer a possibility to tune not only the bandgap but also more importantly the valence band and conduction band edges, specifically through alloying. In Fig. 3.14(a) the conduction-band edge of CdS is illustrated showing that it lies between the conduction-band edge of ZnO and ZnS. Therefore, with alloying, it is possible to align the conduction band edge of a $ZnO_{1-x}S_x$ alloy to that of CdS. From the calculated valence-band and conduction-band edges in Fig. 3.14(a), we have determined that the composition of $ZnO_{1-x}S_x$ for which its conduction-band edge aligns to that of CdS is x~0.75. $ZnO_{0.25}S_{0.75}$ has a bandgap of ~2.8eV, the larger bandgap of this alloy compared to CdS (2.4 eV) will allow more light to penetrate the absorber layer that can lead to an increase in efficiency as more light energy can be converted into electricity. Replacing CdS in thin film solar cells is of interest due to the toxicity of cadmium, since cadmium is one of the most toxic metals. Cadmium containing solar cells currently have stringent recycling procedures for this matter [29].

The goal of this section is to test the performance of CdTe thin film solar cells with a $ZnO_{1-x}S_x$ buffer layer. I collaborated with the Ferekides group at the University of South Florida that focuses on studying and developing thin film photovoltaic technologies. The group was interested in replacing the CdS layer in thin film PV technologies with a $ZnO_{1-x}S_x$ layer. A $ZnO_{1-x}S_x$ sample with x~0.75 sulfur has a bandgap of 2.8 eV, and from the BAC model calculations its conduction band edge is aligned to that of CdS. The $ZnO_{0.25}S_{0.75}$ layer can potentially help make thin film solar cells more efficient due to the larger bandgap that will allow more light to reach the absorber layer underneath to generate more electricity and the proper band alignment that can aid in better charge transfer.

Together we fabricated 8 Cadmium Telluride (CdTe) solar cells with 4 varying sulfur content $ZnO_{1-x}S_x$ layers to see how the fill factor, current-voltage (J-V) characteristics and quantum efficiency (QE) changed with varying sulfur composition. The CdTe solar cells were fabricated in the superstrate configuration, meaning that the substrate is transparent, typically glass and the active layers are deposited above. Therefore, during operation, light passes through the substrate down through the active layers (Figure 3.15). The cell configuration consisted of an EAGLE^{2000TM} glass substrate, an indium tin oxide (ITO) layer, a $ZnO_{1-x}S_x$ layer, the CdTe active layer, and copper doped graphite as a back contact.

Table 3.1 lists the thickness and sulfur composition for the varying ZnOS layers. Two substrates were loaded at each condition to yield 8 samples all together. After depositing the ZnOS layers on the ITO coated EAGLE$^{2000\ TM}$ glass substrate, the samples were sent to the Ferekides group to finish the processing steps and test the solar cells.

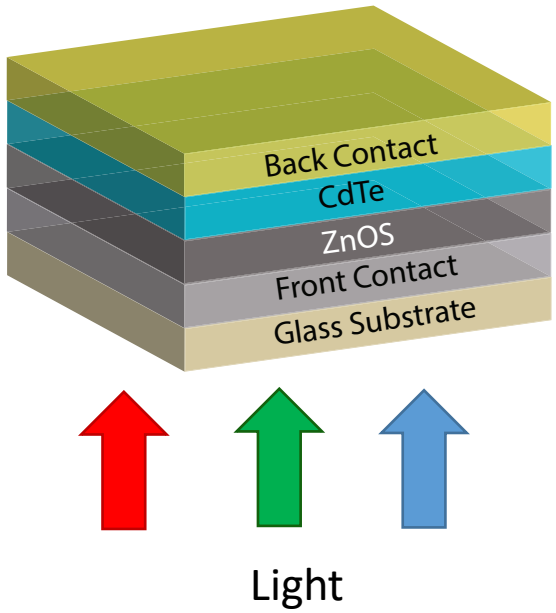

Figure 3.15: Superstrate configuration for the fabricated solar cells.

Table 3.1: List of sulfur content and thickness for the solar cells that were fabricated

Sample ID		Composition (%S)	Thickness (nm)
R1151	5-22-2B	5	134
R1152	5-19-1B	18	139
R1153	5-19-1D	75	142
R1150	5-22-2D	90	145

The short-circuit current (J_{SC}) is the current that flows through the solar cell when the voltage across the solar cell is zero. It is an important parameter as it represents the largest current that can be drawn from the solar cell. The J_{SC} is dependent on the optical properties of the material, minority carrier lifetimes, the incident light intensity and spectrum. The open circuit voltage is the maximum voltage in a solar cell and occurs when the net current is equal to zero. The V_{OC} is dependent on the bandgap of the material, and is also limited by recombination. The fill factor (FF) is a measure of the squareness of the J-V curve for solar cells (Figure 3.16). Quantum efficiency (QE) is a measure of the ratio of the number of carriers collected by the solar cell to the

number of photons incident on the solar cell at a given energy. Therefore, if all the incident photons at a specific energy are absorbed and all of the carriers are collected, then the QE at that energy will be equal to 100%. The open-circuit voltage, short-circuit current, fill factor and quantum efficiency are key performance measurements for solar cells. Understanding the mechanisms that limit these measurements in real devices is critical to their optimization.

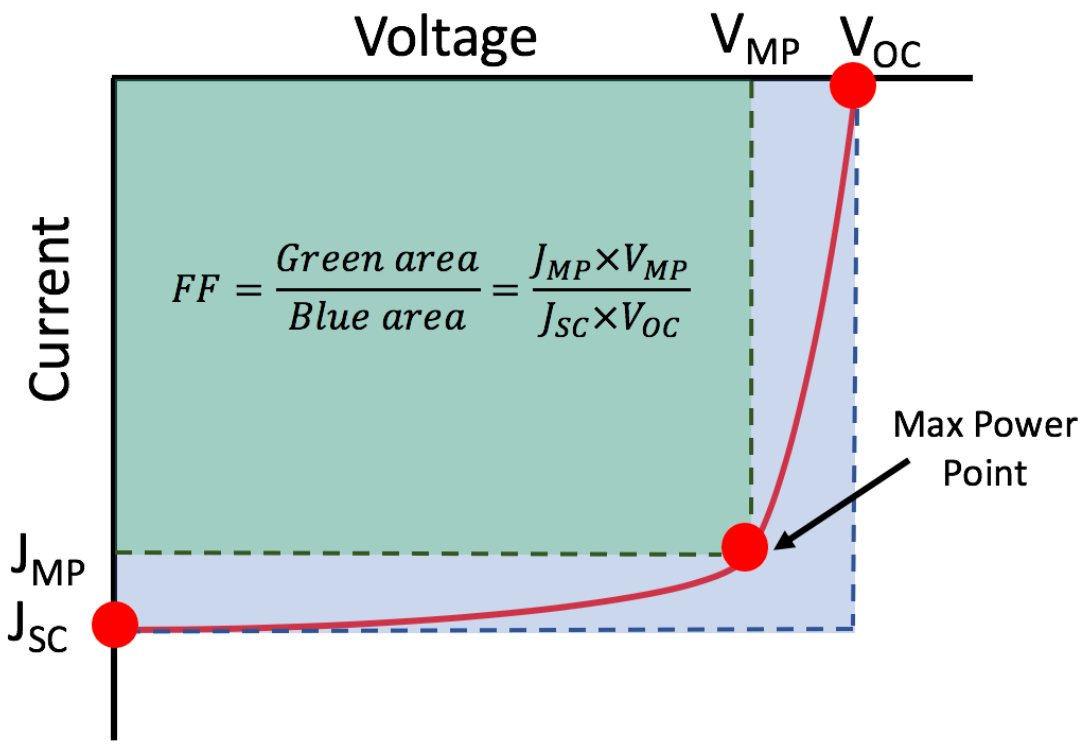

Figure 3.16: Visual representation of a current-voltage curve for a solar cell. At zero voltage the current is equal to J_{SC}. At zero current the voltage is equal to V_{OC}. The FF is defined as the ratio of the maximum power of the cell over the product of V_{OC} and J_{SC}.

3.5.1 Cell with $ZnO_{0.95}S_{0.05}$ Buffer Layer

Table 3.2: The Open Circuit Voltage (V_{OC}), fill factor (FF) and short circuit current (J_{SC}) results for a CdTe solar cell with a $ZnO_{0.95}S_{0.05}$ layer.

Sample ID		V_{OC} (mV)	FF (%)	J_{SC} (mA/cm^2)
R1151	5-22-2B-2	650	46.90%	22.73
	5-22-2B-3	650	47.00%	23.05

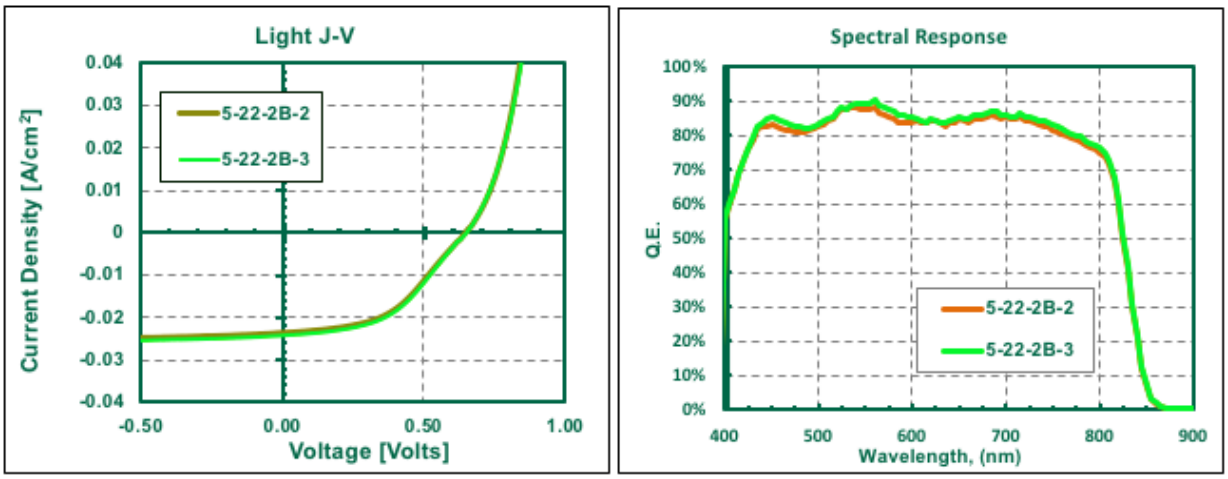

Figure 3.17: J-V (left) and Q.E. (right) results for solar cell with a $ZnO_{0.95}S_{0.05}$ layer.

For the two CdTe cells with a $ZnO_{0.95}S_{0.05}$ layer, the V_{OC}, J_{SC}, FF and QE were found to be similar indicating the stability and reproducibility of these layers (Table 3.2 and Figure 3.17). The reduction of QE can be attributed to reflection and recombination (surface, interface and low diffusion lengths).

3.5.2 Cell with $ZnO_{0.82}S_{0.18}$ Buffer Layer

Table 3.3: The Open Circuit Voltage (V_{OC}), fill factor (FF) and short circuit current (J_{SC}) results for a CdTe solar cell with a $ZnO_{0.82}S_{0.18}$ layer with 18% sulfur.

Sample ID		V_{OC} (mV)	FF (%)	J_{SC} (mA/cm^2)
R1152	5-19-1B-2	500	50.30%	23.09
	5-19-1B-3	450	54.00%	22.16

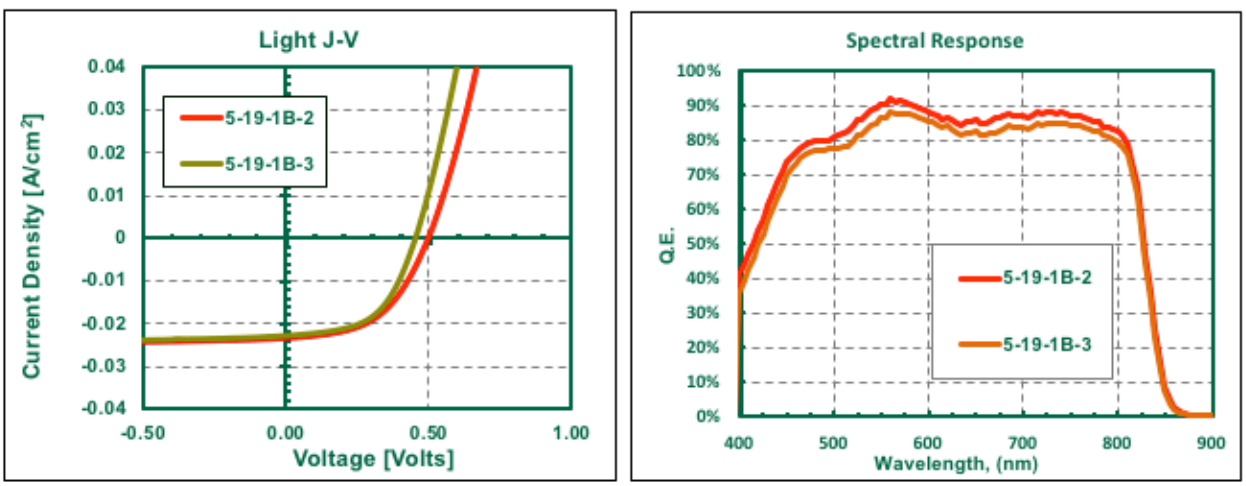

Figure 3.18: J-V (left) and Q.E. (right) results for solar cell with a $ZnO_{0.82}S_{0.18}$ layer.

For the two CdTe cells with a $ZnO_{0.82}S_{0.18}$ layer, the V_{OC}, J_{SC}, FF and QE were found to differ slightly indicating some variability in the cells with the $ZnO_{0.82}S_{0.18}$ layers (Table 3.3 and Figure 3.18). The reduction of QE can be attributed to reflection and recombination (surface, interface and low diffusion lengths).

3.5.3 Cell with $ZnO_{0.25}S_{0.75}$ Buffer Layer

Table 3.4: The Open Circuit Voltage (V_{OC}), fill factor (FF) and short circuit current (J_{SC}) results for a CdTe solar cell with a $ZnO_{0.25}S_{0.75}$ layer.

Sample ID		V_{OC} (mV)	FF (%)	J_{SC} (mA/cm^2)
R1153	5-19-1D-2	610	19.00%	2.03
	5-19-1D-3	640	18.80%	3.46

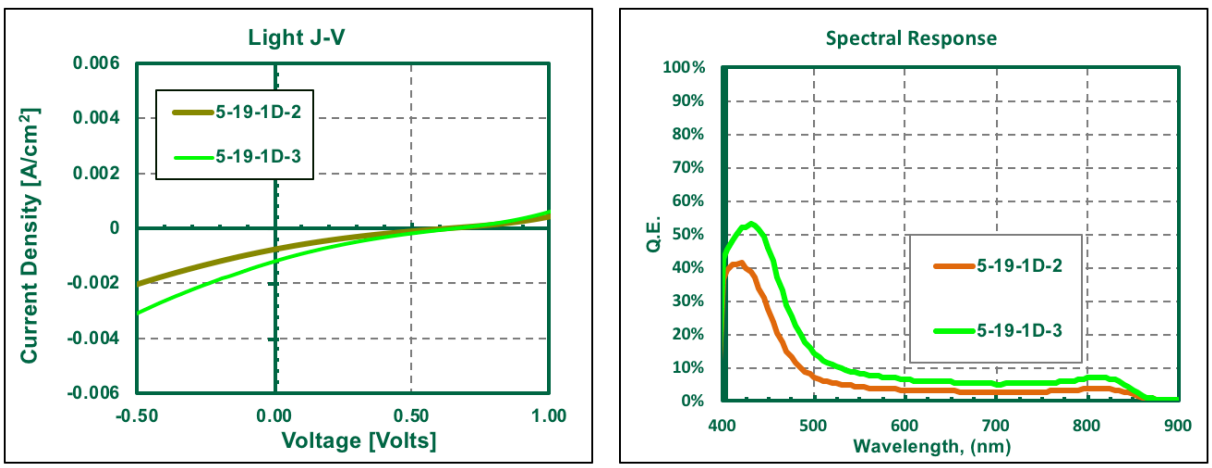

Figure 3.19: J-V (left) and Q.E. (right) results for solar cell with a $ZnO_{0.25}S_{0.75}$ layer.

For the two CdTe cells with a $ZnO_{0.25}S_{0.75}$ layer, the cell performance was found to be poor. In addition, the low V_{OC}, J_{SC}, FF values and poor QE indicate a stability issue with the $ZnO_{0.25}S_{0.75}$ layers (Table 3.4 and Figure 3.19). The degraded QE can be attributed to reflection and recombination (surface, interface and low diffusion lengths). It may be possible that inter diffusion between $ZnO_{0.25}S_{0.75}$ and CdTe has degraded the interface and thus causing poor cell performance.

3.5.4 Cell with $ZnO_{0.05}S_{0.90}$ Buffer Layer

Table 3.5: The Open Circuit Voltage (V_{OC}), fill factor (FF) and short circuit current (J_{SC}) results for a CdTe solar cell with a $ZnO_{0.05}S_{0.90}$ layer.

Sample ID		V_{OC} (mV)	FF (%)	J_{SC} (mA/cm^2)
R1150	5-22-2D-2	440	19.80%	13.84
	5-22-2D-3	440	20.00%	11.67

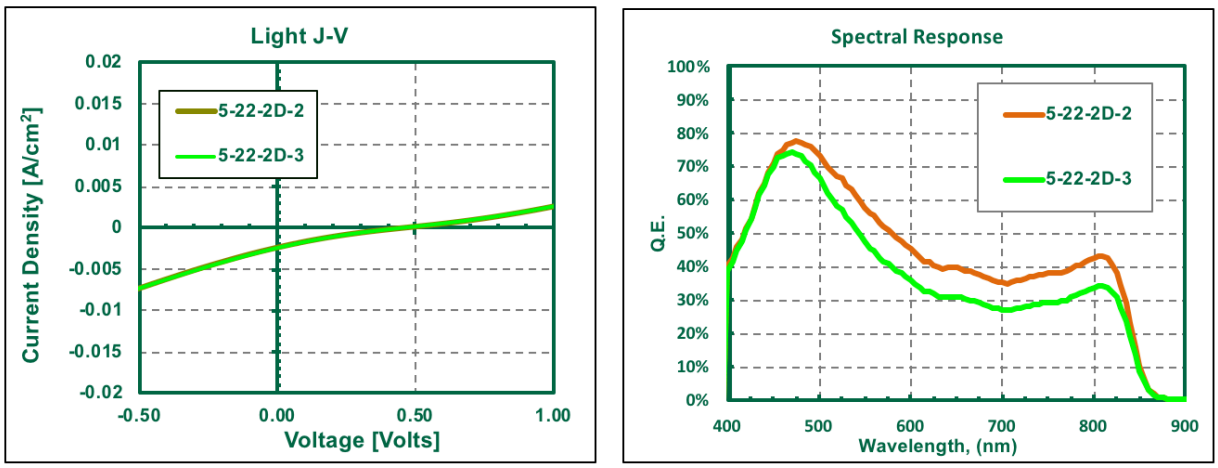

Figure 3.20: J-V (left) and Q.E. (right) results for solar cell with a $ZnO_{0.05}S_{0.90}$ layer.

For the two CdTe cells with a $ZnO_{0.05}S_{0.90}$ layer, the cell performance was found to be poor. In addition, the low V_{OC}, J_{SC}, FF values and poor QE indicate a stability issue with the $ZnO_{0.05}S_{0.90}$ layers (Table 3.5 and Figure 3.20). The degraded QE can be attributed to reflection and recombination (surface, interface and low diffusion lengths). It may be possible that inter diffusion between $ZnO_{0.05}S_{0.90}$ and CdTe has degraded the junction interface and thus causing poor cell performance.

3.5.5 Overall Cell Comparison

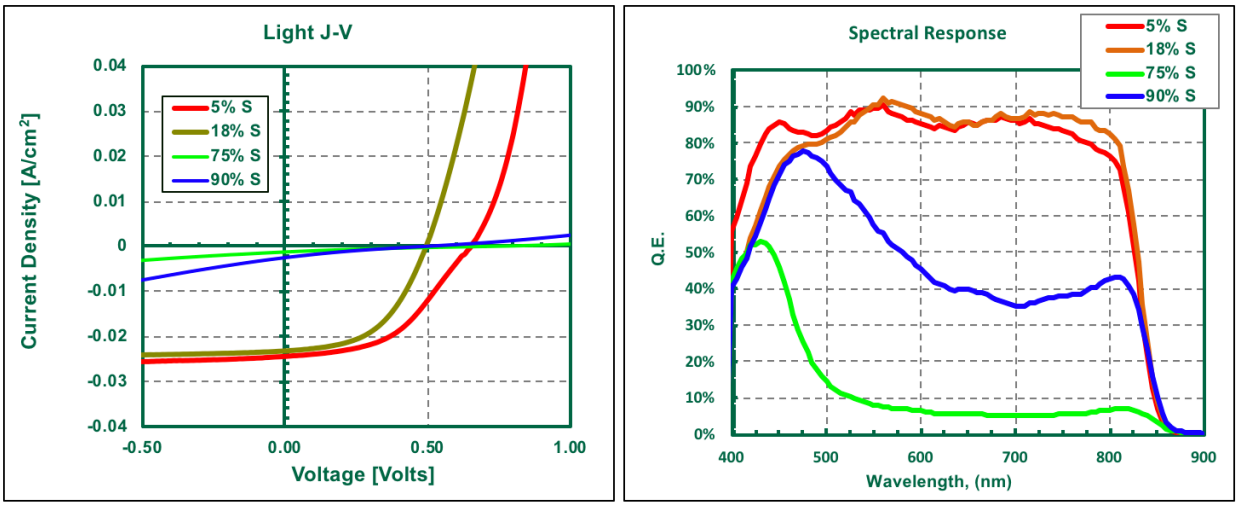

Figure 3.21: Overall J-V (left) and Q.E.(right) results. Using the best cell from every condition.

The cells with lower sulfur content layers (x=0.05 & x=0.18) had higher fill factors, open circuit voltages, short circuit currents, and better quantum efficiency than cells with higher sulfur content (x=0.75 & x=0.90) as shown in Figure 3.21. The trend that we obtained was opposite of what we were expecting. Films with x=0.75 and a bandgap of ~2.8 eV were calculated to have the CBE aligned to that of CdS with a bandgap of 2.4 eV. Films with a similar CBE to that of CdS were expected to be more efficient than films not matching the CBE of CdS. Similar band alignment to CdS and a larger bandgap was expected to allow more light to penetrate the absorber layer that can lead to an increase in efficiency as more light energy can be converted into electricity.

The world record CdTe cell from First Solar has a V_{oc}=0.8759 V, J_{sc} =30.25 mA/cm^2 and FF=79.4%[58]. For the record CZTS cell, V_{oc} =0.7083 V, J_{sc} = 21.77 mA/cm^2 and FF = 65.1 [58]. For the record CIGS cell, V_{oc}=0.744 V, J_{sc} =38.77 mA/cm^2 and FF=79.5% [58]. The solar cells in this work had significantly lower V_{oc}, J_{sc} and FF values compared to the record CdTe, CZTS, and CIGS solar cells, and it is mainly due to non-optimized processing. A comparison of the cells in this work compared to the record CdTe, CZTS and GIGS is shown in Table 3.6. Despite the poor cell performance, these fabricated solar cells were a first step in integrating these materials into devices and have demonstrated that additional studies are needed to improve the overall device.

Table 3.6: Overall cell comparison of cells fabricated in this work compared to the record CdTe, CZTS and CIGS cells [58].

Cell	V_{OC} (mV)	J_{SC} (mA/cm^2)	FF (%)
5% S	650	23.05	47%
18% S	500	23.09	54%
75% S	640	3.46	18.8%
90% S	440	13.84	19.8%
Record CdTe cell	875.9	30.25	79.4%
Record CZTS cell	708.3	21.77	65.1%
Record CIGS cell	744	38.77	79.5%

In order to understand what caused the poor performance of the solar cells with high sulfur content $ZnO_{1-x}S_x$ layers, it is important to study the junction interface, in this case the $ZnO_{1-x}S_x$ and CdTe interface. This will be able to determine if the high processing temperature above 600°C caused sulfur inter diffusion between the $ZnO_{1-x}S_x$ and the active layer. In addition, achieving n-type conductivity of these layers can potentially improve the carrier transport properties and aid in cell performance.

Chapter 4

4 $Ga_2(O,S)_3$ Material Synthesis

Silicon-based technology continues to be the leader in power electronics, communications and digital signal processing devices [59], [60] [61]. However, silicon faces limitations, particularly with scalability for power applications [59]. Silicon technologies in use today are already scaled close to the maximum operating voltages [61] that are limited by the maximum critical electric field strength. There has been a great deal of focus on wide bandgap semiconductors, especially SiC and GaN [62]-[66], leading to enormous progress in power switching and/or power amplifier applications. Further progress in this area requires new materials for devices that operate at higher voltages and higher energy density such as electrified vehicles [62]. The ultra-wide bandgap semiconductors such as diamond, high Al content AlGaN and Ga_2O_3 have shown promising device performance; yet, many challenges exist, including growth maturity, thermal management, cost, and reliability [62], [63], [67].

Gallium oxide is a material of great interest due to its large bandgap (4.8-5.0 eV) [3], [6], [7], [10]-[12] ideal for wide-band-gap optoelectronics, semiconducting lasers, and high-power electronics [62], [66] [68], [69]. Specifically, it will allow power electronic devices to be smaller, faster, more reliable and efficient than current silicon-based counterparts [61]. Baliga's figure of merit (BFOM), commonly used to compare materials for power semiconductor devices, is proportional to the cube of the breakdown field yet only linearly proportional to the electron mobility and dielectric constant [70], [71]. β-Ga_2O_3 has a high breakdown field estimated to be ~8 MV/cm, close to three times larger than those of 4H-SiC and GaN [59], [61], [62], [71], leading to a much higher BFOM.

Several techniques such as MOCVD [72]-[74], PLD [75]-[78] and MBE [71], [79]-[83] have been used for the epitaxial growth of Ga_2O_3-based materials on various substrates. In addition, the ability to obtain high quality bulk substrates from floating zone (FZ) and edge-defined film-fed growth (EFG) methods offer a potential for scalable, cost effective Ga_2O_3 technology which could compete with other high-power materials such as SiC, GaN and diamond [61], [62], [64], [13], [26].

Despite this promise of Ga_2O_3 as a wide band gap semiconductor, it lacks p-type conductivity necessary for most electronic device applications [84], [85]. Bandgap engineering by alloying may be a route to overcome this challenge. Previous alloying studies have been focused on alloying Ga_2O_3 with Al_2O_3 and In_2O_3. The alloying of Ga_2O_3 with Al_2O_3 has been shown to

increase the bandgap and has potential to be used in high-sensitive wavelength tunable photodetectors [86] and in addition further enhance the breakdown voltage [87]. Alloying Ga_2O_3 with In_2O_3 enables tuning of the bandgap to lower energies mainly attributed to shifts in the conduction band edge [88] also making them advantageous for solar blind photodetectors with tunable absorption edges [89]. The ability to form heterostructures and alloys greatly increase the range of potential applications for Ga_2O_3-based technologies; hence we report the alloying of Ga_2O_3 with Ga_2S_3. Alloying Ga_2O_3 with isolectronic anions are expected to have a drastic change in the electronic band structure analogous to various HMA such as $GaN_{1-x}As_x$

This chapter is focused on the growth of stoichiometric Gallium Oxide (Ga2O3) and Gallium Oxide Sulfide (Ga2(O,S)3) thin films by PLD. Section 4.1 focuses on the growth of Ga2O3 by PLD. Section 4.2 focuses on the growth of Ga2(O,S)3 alloys. Section 4.3 combines the results of the optical characterization with the band anticrossing model to explain the reduction in bandgap for the $Ga_2(O_{1-x}S_x)_3$ alloys. To the author's knowledge, this is the first report on the growth and characterization of $Ga_2(O_{1-x}S_x)_3$ alloys.

4.1 Growth of β-Ga_2O_3

The growth of β-Ga_2O_3 was first achieved before the growth of $Ga_2(O_{1-x}S_x)_3$ alloys. The films were targeted to grow stoichiometrically. This was accomplished with a background O_2 pressure of 7.4×10^{-4} Torr and a substrate to target distance of 20 mm. After obtaining stoichiometric films, the substrate temperature was varied to understand the effect of temperature on the crystallinity of the Ga_2O_3 films. Normal θ–2θ X-ray diffraction on three samples with varying substrate temperatures are shown in Figure 4.1. Consistent with previous reports [68] [73] the films were found to be (-2 0 1) oriented for growth with a substrate temperature of 650 °C with (-2 0 1) (2θ=18.9°), (-4 0 2) (2θ=38.3°) and (-6 0 3) (2θ=59°) . The film grown at 600 °C had an additional peak at (400) (2θ=30.45°), the structure of this film can be presumed to be polycrystalline with multi-orientations. These particular films were found to be insulating with a bandgap ~5 eV found by extrapolating α^2 to zero.

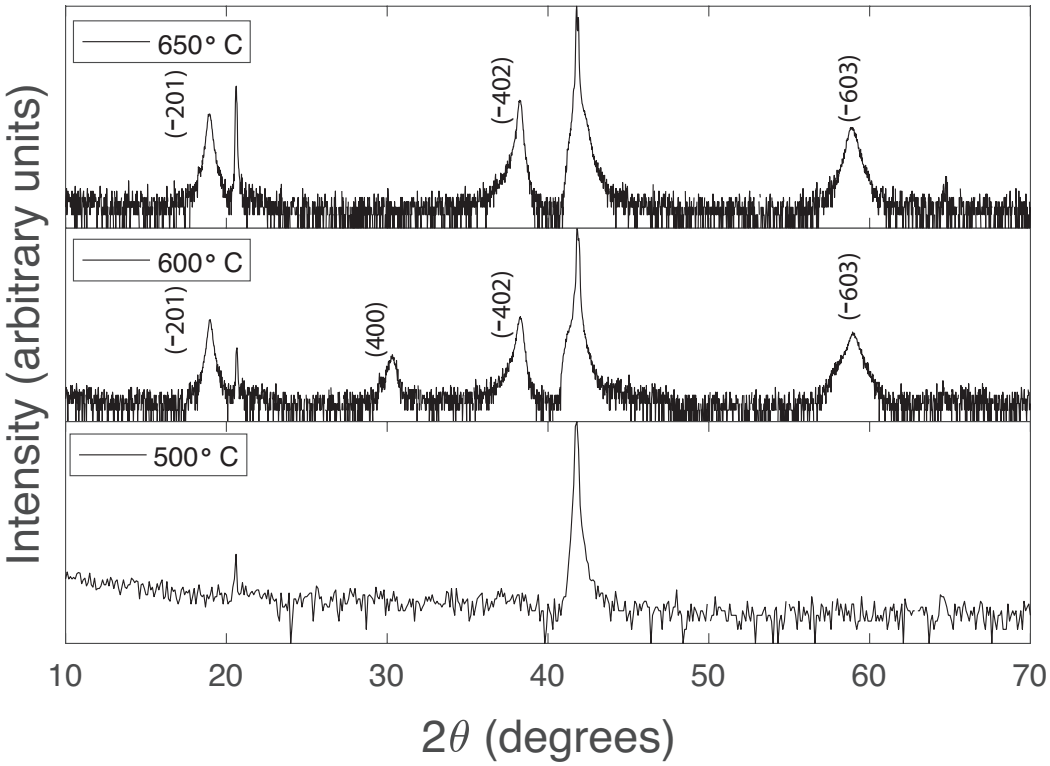

Figure 4.1: θ–2θ X-ray diffraction of Ga_2O_3 films grown at different substrate temperatures. Films at 650C were shown to be (-2 0 1) β-Ga_2O_3 films. All unlabeled peaks correspond to sapphire.

4.2 Growth of $Ga_2(O,S)_3$

The $Ga_2(O_{1-x}S_x)_3$ thin films were deposited on double-side polished, c-plane sapphire substrates by PLD using a KrF laser (λ = 248 nm) with a 20 ns laser pulse duration and a laser spot size of 6 mm^2 . The laser fluence used in this work was fixed at 2.3 J/cm^2 with a laser repetition rate of 1 Hz. Three $Ga_2(O_{1-x}S_x)_3$ PLD targets composed with varying S content were used in this study: x=0, 0.1, 0.4 and 0.5. The films were grown at various temperatures ranging from 450°C to 650 °C with a background gas environment of vacuum, O_2 and Ar. The film thickness and alloy composition were measured by RBS using a 3 MeV He^{2+} ion beam. The $Ga_2(O,S)_3$ alloys have been determined to be amorphous through XRD and TEM measurements. The absorption coefficient of the $Ga_2(O_{1-x}S_x)_3$ films was obtained from transmission and reflection measurements taken in the spectral range of 250 to 2500 nm. The bandgaps of the dilute-sulfur samples were determined by fitting the absorption coefficient spectra using a modified valence band anticrossing (BAC) model [12]-[15].

After achieving the growth of crystalline β-Ga_2O_3 films, the growth was focused on $Ga_2(O_{1-x}S_x)_3$ alloys. Cold-pressed powder targets with varying compositions of Ga_2O_3 and Ga_2S_3 were used. One major challenge of growing $Ga_2(O_{1-x}S_x)_3$ alloys was achieving stoichiometric films. The initial growths were found to be Ga-rich presumably due to sulfur high vapor pressure (i.e., low sticking coefficient) at temperatures above 600 °C [90] and this effect can be seen in Figure 4.2. Targets with an additional 7 at% of S led to stoichiometric $Ga_2(O_{1-x}S_x)_3$ films with sulfur ratios, [S]/([S]+[O]) from 0.013-0.35 measured through RBS and grown at various temperatures ranging from 450°C to 650 °C. In Figure 4.3, the ([S]+[O])/[Ga] ratio is shown to be close to 1.5 indicating that these films are stoichiometric.

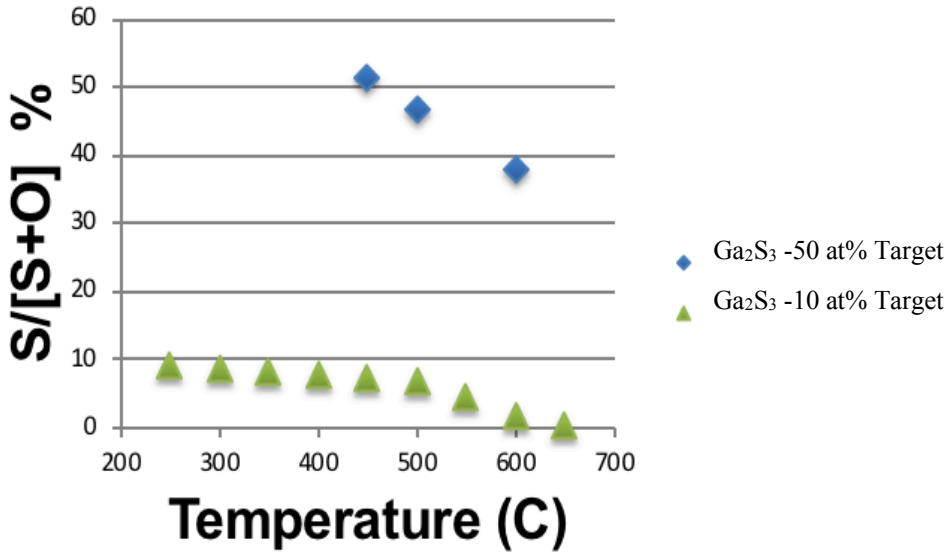

Figure 4.2: The sulfur ratio of films grown at varying substrate temperatures. As the substrate temperature increases the sulfur ratio decreases due to outgassing.

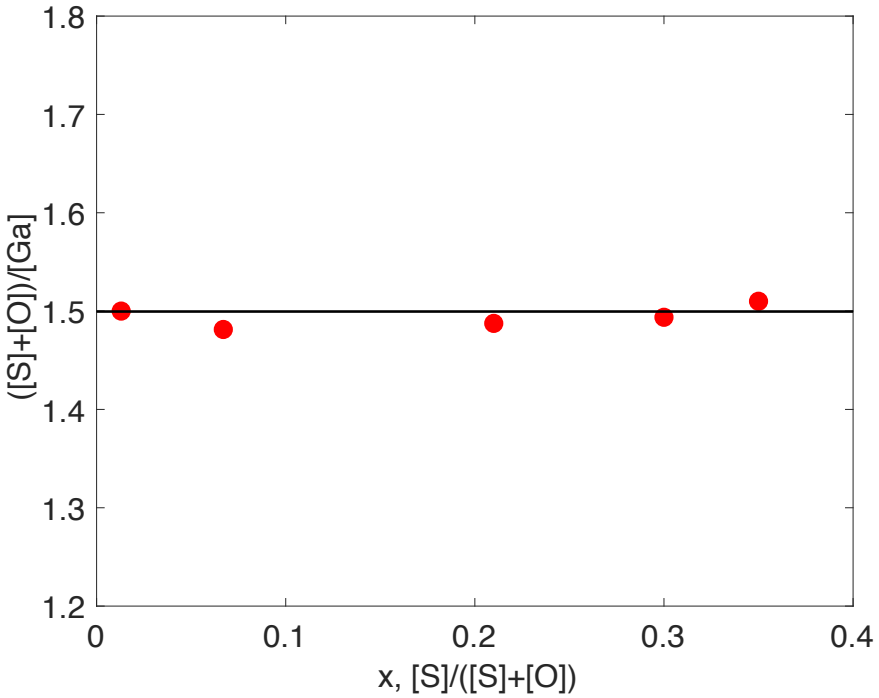

Figure 4.3: Shows the ([S]+[O])/[Ga] ratio is close to 1.5 indicating stoichiometric films. S, O and Ga quantities determined by RBS.

All $Ga_2(O_{1-x}S_x)_3$ films with x>0 were found to be amorphous via XRD. The θ–2θ X-ray diffraction pattern of a (-2 0 1) β-Ga_2O_3 film is shown in Figure 4.4 alongside two $Ga_2(O_{1-x}S_x)_3$ films shown to be amorphous via XRD. Figure 4.5(a) shows a HR-TEM image of a $Ga_2(O_{1-x}S_x)_3$ film with x= 0.013 and a thickness of 65 nm with the chromium (Cr) layer, $Ga_2(O_{1-x}S_x)_3$ film and sapphire substrate indicated in the image. The image was taken with a TEAM microscope with single atom sensitivity. Figure 4.5(b) presents a fast Fourier transform (FFT) that is a diffused ring pattern of the $Ga_2(O_{1-x}S_x)_3$ layer indicating that the film is amorphous. The red arrows indicate dots in the FFT that are from adjacent crystalline layers. Additional shapes in the FFT are from residual aberration parameters.

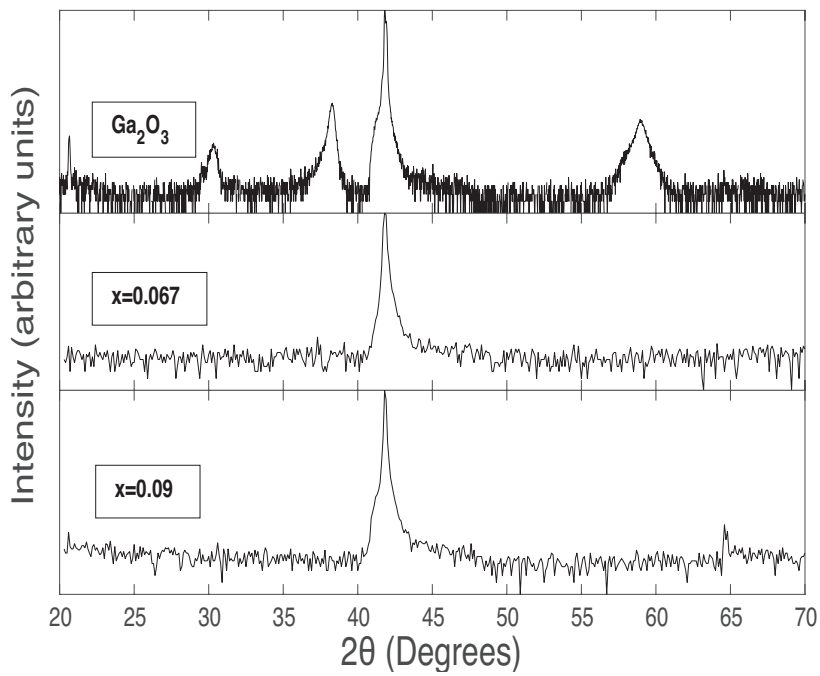

Figure 4.4: θ–2θ X-ray diffraction patterns of a (-2 0 1) β-Ga_2O_3 film compared to two $Ga_2(O_{1-x}S_x)_3$ films shown to be amorphous via XRD.

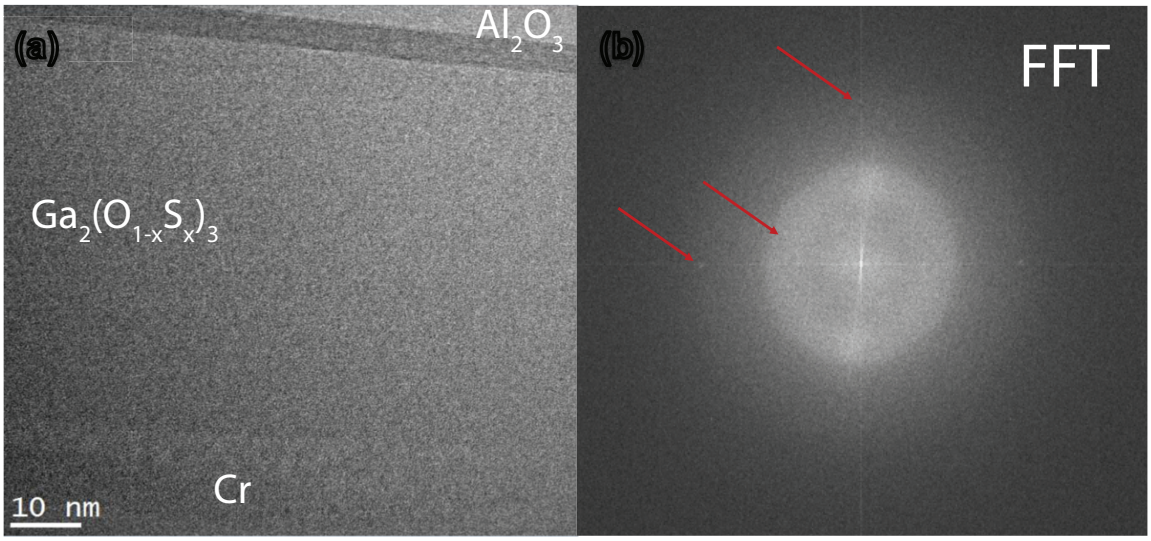

Figure 4.5: a) HR-TEM image of a $Ga_2(O_{1-x}S_x)_3$ film with x= 0.013 and a thickness of 65 nm. Three layers are indicated in the image. b) Fast Fourier Transform (FFT) that shows a diffused ring pattern of the $Ga_2(O_{1-x}S_x)_3$ layer indicating that film is indeed amorphous. The red lines indicate dots in the FFT that are from adjacent crystalline layers.

The absorption spectra for samples with sulfur x<0.35 films are shown in Figure 4.6. Despite the amorphous structure all the samples show very well-defined optical absorption edges that shift abruptly to lower energies upon S incorporation. This is similar to the amorphous HMA GaNAs system where replacement of N with As atoms results in a rapid reduction of the optical bandgap [10], [11]. The shift of the bandgap is especially rapid at low S content; as is seen in Fig. 4.6, replacing O with only 1 % S reduces the absorption energy by almost 1 eV indicating that, similarly to the GaNAs alloy system, the band structure of $Ga_2(O_{1-x}S_x)_3$ alloys is determined by the anticrossing interaction between localized S level and the bands of the Ga_2O_3 host matrix [10], [11].

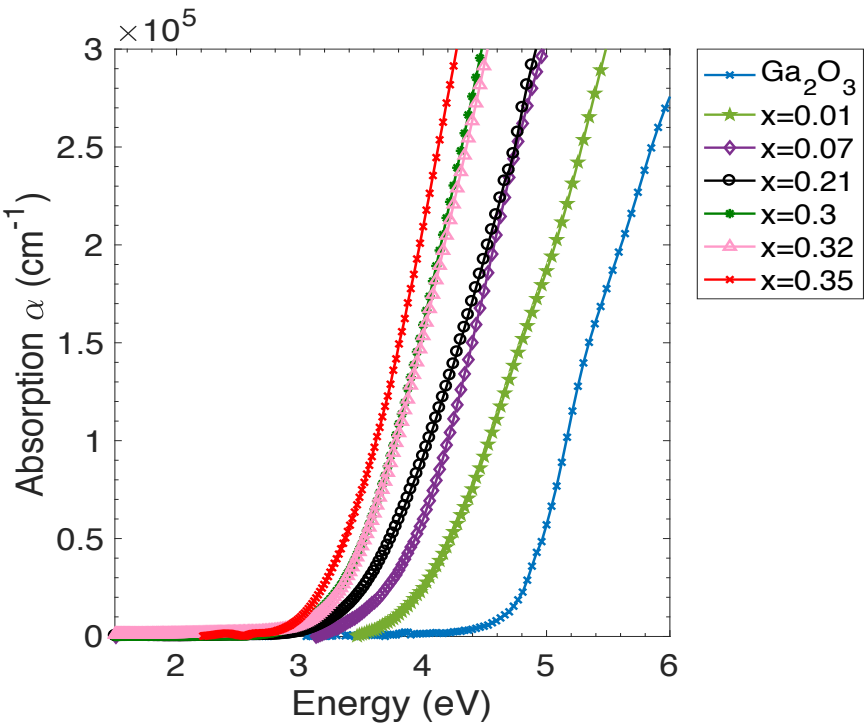

Figure 4.6: Absorption coefficient for various $Ga_2(O_{1-x}S_x)_3$ with x<0.35.

4.3 Band Anticrossing in $Ga_2(O_{1-x}S_x)_3$

In the BAC model, the substitution of O with less electronegative S introduces a localized level above the valence band edge of Ga_2O_3 host. The interaction of the localized S level with the extended valence-band states of Ga_2O_3 results in a splitting of the valence band into two subbands ($E_+$and E_-). At the dilute sulfur compositions, the valence BAC (VBAC) effect produces a narrow, non-parabolic S-derived band with the total number of states dependent on the S content. In a simplified version of the VBAC model the dispersion relations for the $E_+(k)$ and $E_-(k)$ subbands are given by Equation 1.4. Here E_d refers to the S localized level, $E_V(k)$ corresponds to the dispersion relation of the band that is undergoing an anticrossing effect (i.e. valence band of Ga_2O_3), C_S is the coupling parameter which represents the coupling strength between the localized and delocalized states, and x is the S ratio.

As mentioned previously, the valence BAC effect occurs when S substitutes O in the Ga_2O_3 matrix. Previously reported deviations of the BAC fit in the midrange region were primarily due to the assumption of constant coupling parameters in the BAC calculations [15]. Here, we adopt a modified BAC model that uses composition dependent coupling parameters in which composition dependence is included within the virtual crystal approximation. The modified BAC model improved the fitting of experimental data in the mid-range region for the $GaN_{1-x}Sb_x$ and $ZnO_{1-x}Te_x$ systems [15], [17].

The VB and CB matrix band edges (i.e. wavevector k = 0), and effective masses are given by the linear interpolation between the end point compounds:

$$E_V = (1-x)E_{V,ZnO} + xE_{V,ZnS} \quad (4.1)$$

$$E_C = (1-x)E_{C,ZnO} + xE_{C,ZnS} \quad (4.2)$$

where $E_{V,ZnO}$ and $E_{V,ZnS}$ are the VBEs, and $E_{C,ZnO}$ and $E_{C,ZnS}$ are the CBE of ZnO and ZnS respectively. The effective masses are similarly written:

$$m_h^* = (1-x)m_{h,ZnO}^* + xm_{h,ZnS}^* \quad (4.3)$$

$$m_e^* = (1-x)m_{e,ZnO}^* + xm_{e,ZnS}^* \quad (4.4)$$

where m_h^* and m_e^* are the effective mass of holes and electrons respectively. Also the composition dependencies of the coupling parameter for $Ga_2(O_{1-x}S_x)_3$ is given by:

$$C_S(x) = (1-x)C_{S0} \quad (4.5)$$

where C_{S0} is the coupling constant determined in the dilute S composition limits [126][101].

This study has been intentionally limited to amorphous stoichiometric films which show relatively sharp and well-defined absorption edges. This can be understood in terms of the highly localized nature of the potentials responsible for the BAC interaction. Thus, as long as the coordination number of the O (S) site remains constant the energy levels of the localized states and their contribution to the anticrossing interaction are well defined. In contrast, for non-stoichiometric films, we found them to have absorption at much lower energies. We attribute this low energy absorption to possible variations in the coordination number of O (S) sites and thus also to a spread in the energy and the strength of the BAC interaction.

Since this work is focused on $Ga_2(O_{1-x}S_x)_3$ films with x<0.35, we adopt the simplified version of the valence BAC [24]. We take into consideration optical transitions from the various valence subbands to the conduction band. We also include optical transitions from the spin-orbit split S band to the conduction band with a spin-orbit splitting energy of 0.06 eV [91].

The calculated absorption for a $Ga_2(O_{1-x}S_x)_3$ alloy film consists of four optical transitions:

1. From S derived band (E_V^+) to matrix-like conduction band (E_C).
2. From S spin orbital band (E_{SO}^+) to matrix-like conduction band (E_C).
3. From S spin orbital band (E_{SO}^-) to matrix-like conduction band (E_C).
4. From matrix-like valence band (E_V^-) to matrix-like conduction band (E_C).

The optical joint density of states (JDOS) were convolved with a Gaussian function at each wave vector *k*, an approach used in [15], [16], [18], [24] to account for the broadening in the bands. The calculated absorption coefficient includes all four transitions and is denoted by:

$$\alpha(\hbar\omega) = \alpha_0 \left[\frac{2}{3} g_+(\hbar\omega) + \frac{1}{3} g_{+,so}(\hbar\omega) + \frac{1}{3} g_{-,so}(\hbar\omega) + \frac{2}{3} g_-(\hbar\omega)\right]. \quad (4.6)$$

The coupling parameter C_{S0} and E_S were found by fitting the measured absorption coefficient with the BAC calculations. The best-fit broadening parameters were found by minimizing the root-mean-square error between the experimental absorption curve and the calculated absorption. The broadening parameters (Δ_V^+, Δ_V^-, Δ_{SO}^+, Δ_{SO}^-) ranged from 0.01 eV to 0.6 eV.

Figure 4.7(a) shows the experimental result and the fitting of the absorption coefficient using the VBAC for the film with x=0.067 sulfur ratio whereas Figure 4.7(b) shows the contributions of different optical transitions to the total absorption. These fittings were done for all the dilute-S samples, and it was possible to extract the energy of the S level, E_S, at 1 eV above the valence-band edge of Ga_2O_3 and C_{S0} of 1.6 eV. The location of the sulfur energy level is consistent with previous reports on $ZnO_{1-x}S_x$ where the S level was found to be at 0.3 eV above the ZnO valence-band edge [18]. This translates to the S level being about 1.0 eV above the valence-band edge of Ga_2O_3 [92]as illustrated in Figure 4.8. Using the values of the coupling parameter and the S level energy, we calculate the band structure (Fig. 4.9) and determine the bandgap of the $Ga_2(O_{1-x}S_x)_3$ alloys given by the energy separation between the maximum of the E_+ subband and the conduction band minimum. The BAC calculations show that the reduction in the bandgap of O-rich $Ga_2(O_{1-x}S_x)_3$ films is mainly due to the upward movement of the highest valence-band edge.

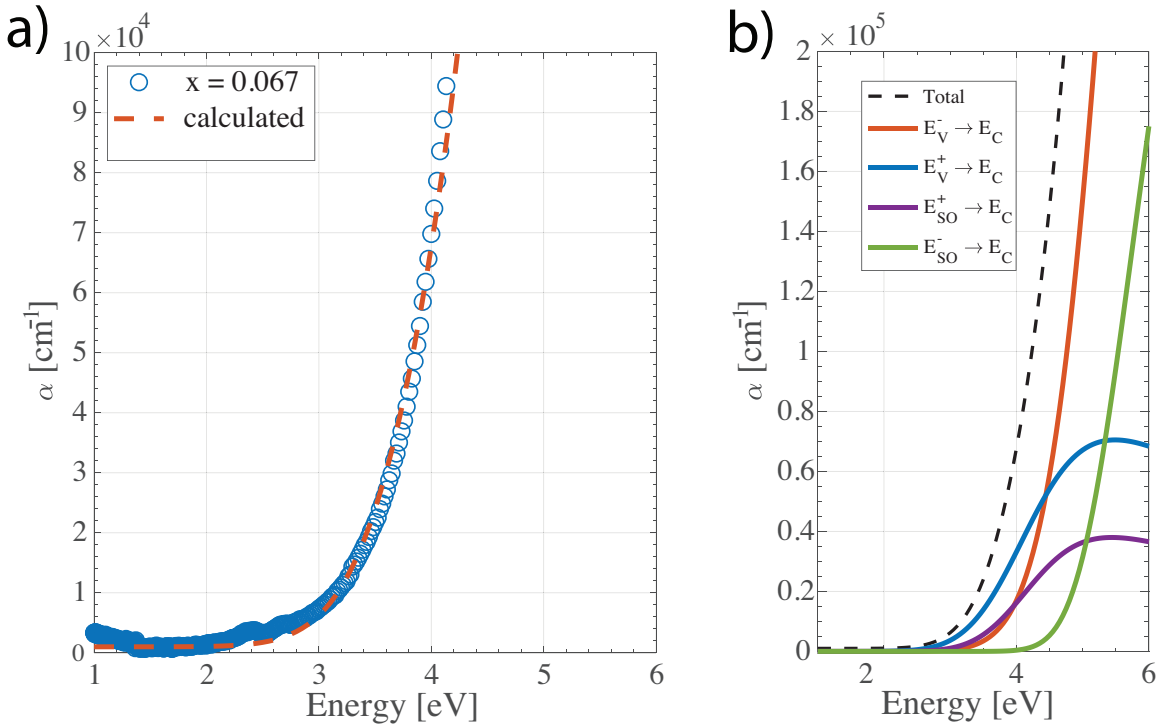

Figure 4.7: (a) Measured and calculated absorption coefficient for $Ga_2(O_{1-x}S_x)_3$ with x=0.067. The calculations were performed using the VBAC model. (b) Contributions of different optical transitions to the total calculated absorption coefficient (dashed line) using the VBAC. The sulfur level is located 1 eV above the Ga_2O_3 valence band and the coupling parameter, $C_S(x=0)$, is 1.8 eV.

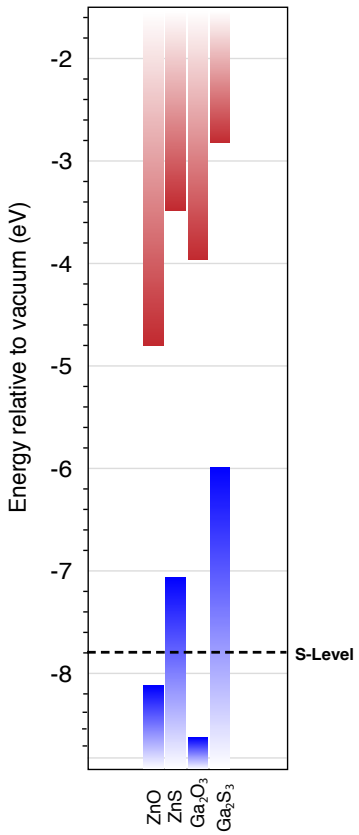

Figure 4.8: Band edges of ZnO, ZnS, Ga_2O_3 [92]and Ga_2S_3 [93]relative to vacuum with the sulfur level found to be consistent with previous $ZnO_{1-x}S_x$ work [18].

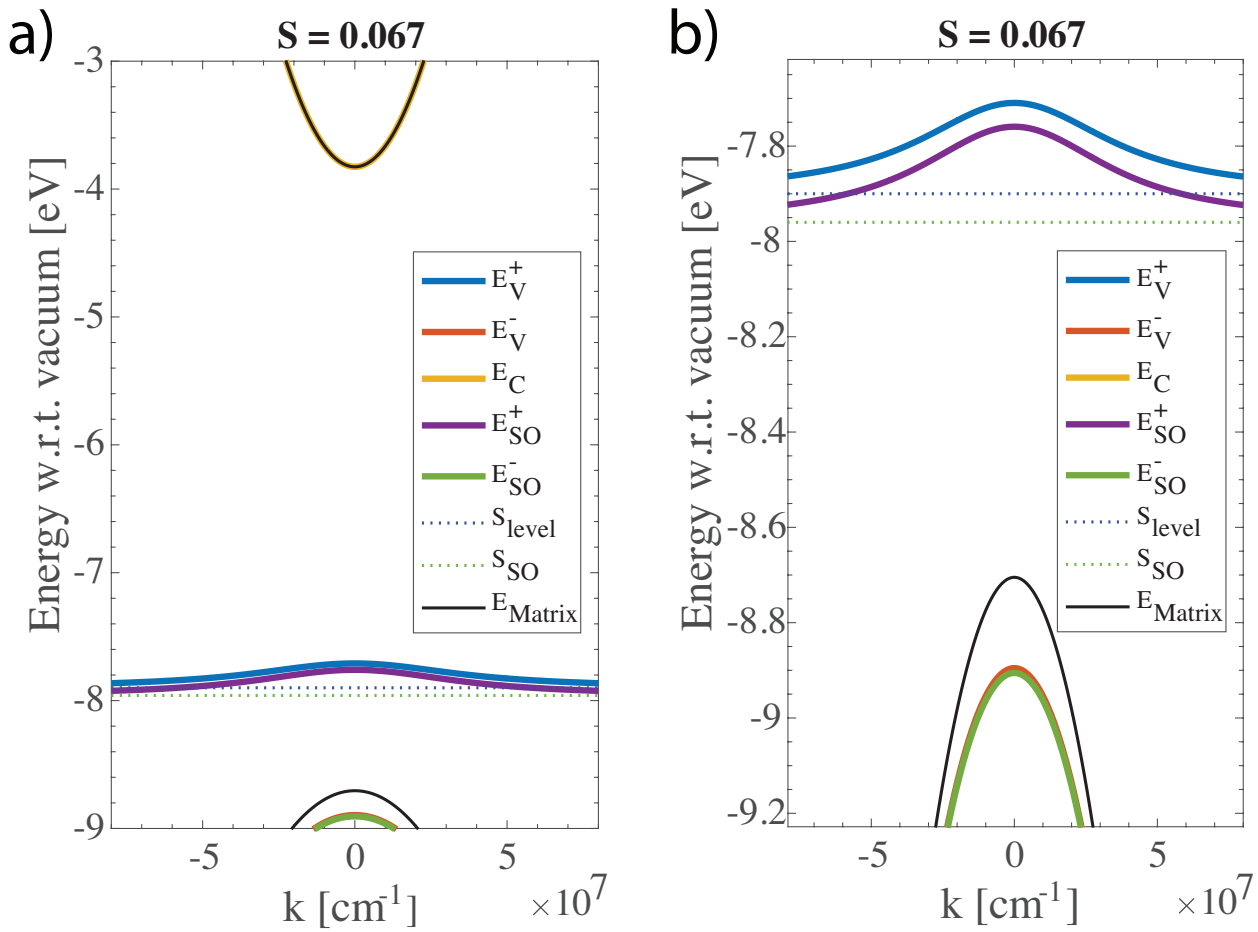

Figure 4.9: (a) Calculated BAC electronic band structure of a $Ga_2(O_{1-x}S_x)_3$ film with x=0.067 sulfur ratio. It shows the various valence bands that resulted from the interaction of the S states with the matrix valence band. (b) The (a) zoomed in to illustrate the details of valence band structure.

Using the values of E_S, and C_S obtained in this work we also calculated the dependence of the conduction band and valence band edges of the O-rich $Ga_2(O_{1-x}S_x)_3$ films with x<0.51. These calculations were performed using the compositional weighting method proposed in [11], [12], [15]-[18], [24]. In Fig. 4.10(a), the bandgaps calculated from the absorption fitting using valence BAC for samples with sulfur x< 0.35 are shown as blue unfilled circles. The compositional weighting method is labeled as BAC since it utilizes the values E_S, and C_S determined through the absorption fittings described earlier. It is seen in Fig. 4.10(a) that the BAC model provides a very good description of the composition dependence of the bandgap of the alloy including an initial abrupt reduction. Figure 4.10(b) shows the dependence of the conduction band edge and valence band edge as a function of sulfur ratio. As the sulfur ratio increases the reduction in bandgap is shown to be due to an upward shift of the upper valence band.

The amphoteric defect model has been used to predict maximum free carrier concentration attained through doping [94]. Additionally, the model relates the location of the band edges relative to the Fermi-level stabilization (E_{FS}~4.9eV below vacuum level) to the doping concentration and type [95]. In the case of Ga_2O_3 , the conduction band edge lies very close to E_{FS} while the valence band edge is far below E_{FS}, indicating the ease of n-type doping and difficulty in p-type doping respectively. Therefore the ability to shift the valence band edge towards E_{FS} may enable p-type doping in Ga_2O_3-based technologies.

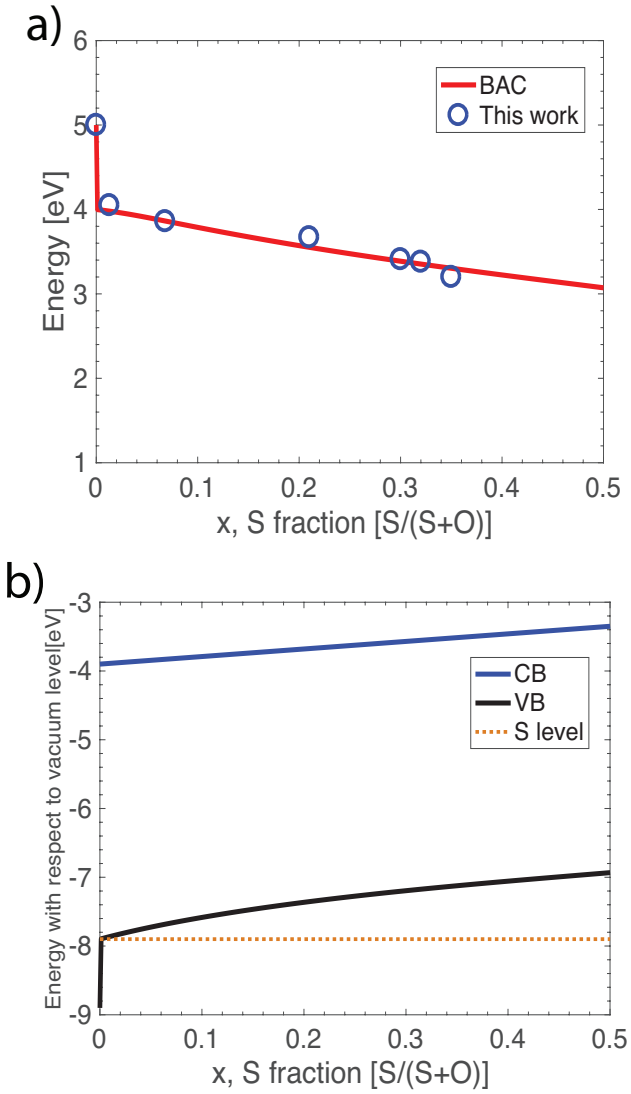

Figure 4.10: Composition dependence of the bandgap of $Ga_2(O_{1-x}S_x)_3$ alloys. BAC bandgap was determined by subtracting the calculated valence band edge from the calculated conduction band edge shown in (b).

$Ga_2(O_{1-x}S_x)_3$ stoichiometric amorphous films were synthesized with $x \leq 0.35$ using PLD. All deposited films, even with very small S content, were found to be amorphous. Despite being amorphous, these alloys $Ga_2(O_{1-x}S_x)_3$ show relatively sharp absorption edges that could be tuned from 5 eV down to 3 eV by changing S content in the range $0 \leq x \leq 0.35$. The absorption properties of the alloy are well explained by the band anticrossing model. Fitting the absorption coefficient of this alloy system yields the coupling parameters and the location of the localized level of S relative to the valence-band edge of the Ga_2O_3 host matrix. The results show that replacing a small amount of O with S produces a large upward shift of the valence-band edge. The effect could be used to control band offsets of this alloy with other oxides.

Chapter 5

5 Conclusion and Future Work

5.1 $ZnO_{1-x}S$ Conclusions

ZnO_xS_{1-x} films were synthesized over the whole composition range using radio frequency magnetron sputtering and PLD. ZnO and ZnS are miscible and alloys from them are likely isocrystalline (wurtzite) for all compositions. The bandgap of $ZnO_{1-x}S_x$ was tuned from 3.7 eV down to 2.6 eV, and the band anticrossing model explains these optical results. Fitting the absorption coefficient of this system, the coupling parameters and the S localized level within the ZnO bandgap were found. These values were used to predict the energies of the conduction-band and the valence-band edges relative to the vacuum level. The $ZnO_{1-x}S_x$ sample with x~0.75 sulfur has a band gap of 2.8 eV, and from model calculations its conduction band edge is aligned to that of cadmium sulfide (CdS)-a material used as the buffer/n-type layer in thin film solar cells with a bandgap of 2.4 eV. The x=0.75 sulfur $ZnO_{1-x}S_x$ layer can help make thin film solar cells more efficient due to the larger bandgap that will allow more light to reach the absorber layer underneath to generate more electricity and the proper band alignment that can aid in better charge transfer.

5.1.1 Future Work

Before these films can be used in a device, the film properties have to be fully understood throughout the entire composition range. Since the band edges are important for implementing semiconducting materials in devices, it is vital to experimentally determine the valence-band and conduction-band edges through techniques such X-ray absorption spectroscopy (XAS) and X-ray emission spectroscopy (XES). This will also experimentally validate the valence-band and conduction-band edges calculated with the BAC model.

The films deposited were all highly resistive; therefore, achieving n-type doping of these alloys will aid in understanding how to modify the electrical properties of $ZnO_{1-x}S_x$ alloys through either material synthesis (adding dopants during the growth) or post-processing methods (e.g. implantation, annealing). This will also aid in creating alternative indium-free transparent conducting oxides to reduce costs in several optoelectronic devices.

In order to understand what caused the poor performance of the solar cells with high sulfur content $ZnO_{1-x}S_x$ layers, it is important to study the junction interface, in this case the $ZnO_{1-x}S_x$ and CdTe interface. This will be able to determine if the high processing temperature above 600°C caused sulfur inter diffusion between the $ZnO_{1-x}S_x$ layer and the absorber layer.

5.2 $Ga(O,S)_3$ Conclusions

$Ga_2(O_xS_{1-x})_3$ stoichiometric amorphous films were synthesized with $x \leq 0.35$ using PLD. All deposited films, even with very small S content, were found to be amorphous. Despite being amorphous, these alloys $Ga_2(O_xS_{1-x})_3$ show relatively sharp absorption edges that could be tuned from 5 eV down to 3 eV by changing S content in the range $0 \leq x \leq 0.35$. The absorption properties of the alloy are well explained by the band anticrossing model. Fitting the absorption coefficient of this alloy system yields the coupling parameters and the location of the localized level of S relative to the valence-band edge of the Ga_2O_3 host matrix. The results show that replacing a small amount of O with S produces a large upward shift of the valence-band edge. The effect could be used to control band offsets of this alloy with other oxides.

5.2.1 Future Work

One method that can address the challenge of synthesizing crystalline $Ga_2(O,S)_3$ films is by utilizing a buffer layer of crystalline β-Ga_2O_3 to minimize the lattice mismatch between the substrate and $Ga_2(O,S)_3$ film which will encourage the formation of a crystalline film. XRD, S/TEM (scanning TEM and TEM) techniques are vital for studying the film microstructure such as crystallinity, growth orientation and defects. Energy dispersive spectroscopy (EDS) and electron energy loss spectroscopy (EELS) commonly found in S/TEM systems provide the ability to examine the local chemical composition to determine if the alloys are homogeneous.

The $Ga_2(O,S)_3$ films were highly insulating, therefore, studying the role of defects and doping of these alloys to enable high electrical conductivity is of importance to be able to utilize them in devices. Pure Ga_2O_3 can be doped n-type with Si and Sn; therefore, attempting to introduce dopants through materials synthesis and post-processing methods (e.g. rapid thermal annealing, annealing) will be of importance.

Using a similar approach to explore band structure engineering in other oxide materials such as alloys of gallium oxide with other group VI (Se and Te) elements to form $Ga_2(O,VI)_3$ alloys would be very interesting as there is few if any literature regarding these alloys. Therefore, being able to investigate the fundamental materials properties of these alloys will determine if these materials can find useful applications. In addition, quaternary alloys of gallium oxide with Al_2O_3 and In_2O_3 to form $(Ga,Al)_2(O,VI)_3$ and $(Ga,In)_2(O,VI)_3$ alloys will allow the ability control both conduction-band and valence-band edges simultaneously. Being able to tune the conduction band and valence band edges is ideal for designing new device concepts with these materials.

5.3 Overall Conclusions

In both ZnO and Ga_2O_3 the introduction of S causes an abrupt reduction in the optical bandgap which has been attributed to an upward shift of the valence band. In both cases, the BAC model works in similar fashion despite the different crystallographic structure. All ZnO_xS_{1-x} were found to be miscible and crystalline throughout the entire composition. On the other hand, all $Ga_2(O_xS_{1-x})_3$ films (with the exception of β-Ga_2O_3) were found to be amorphous. Despite the amorphous nature, stoichiometric $Ga_2(O_xS_{1-x})_3$ films show relatively sharp absorption edges. Applying the band anticrossing model to both systems resulted in a sulfur level located at ~ -7.8 eV with respect to vacuum (~0.3 eV above the VB of ZnO and ~1 eV above the VB of Ga_2O_3).

Appendix A

A.1 Band Offsets of Various Semiconductors

The band offsets of various semiconductors compiled from various references [96]-[99], are shown in Figure A.1. The position of cation d donor and acceptor levels is included from Vesely and Langer [98].

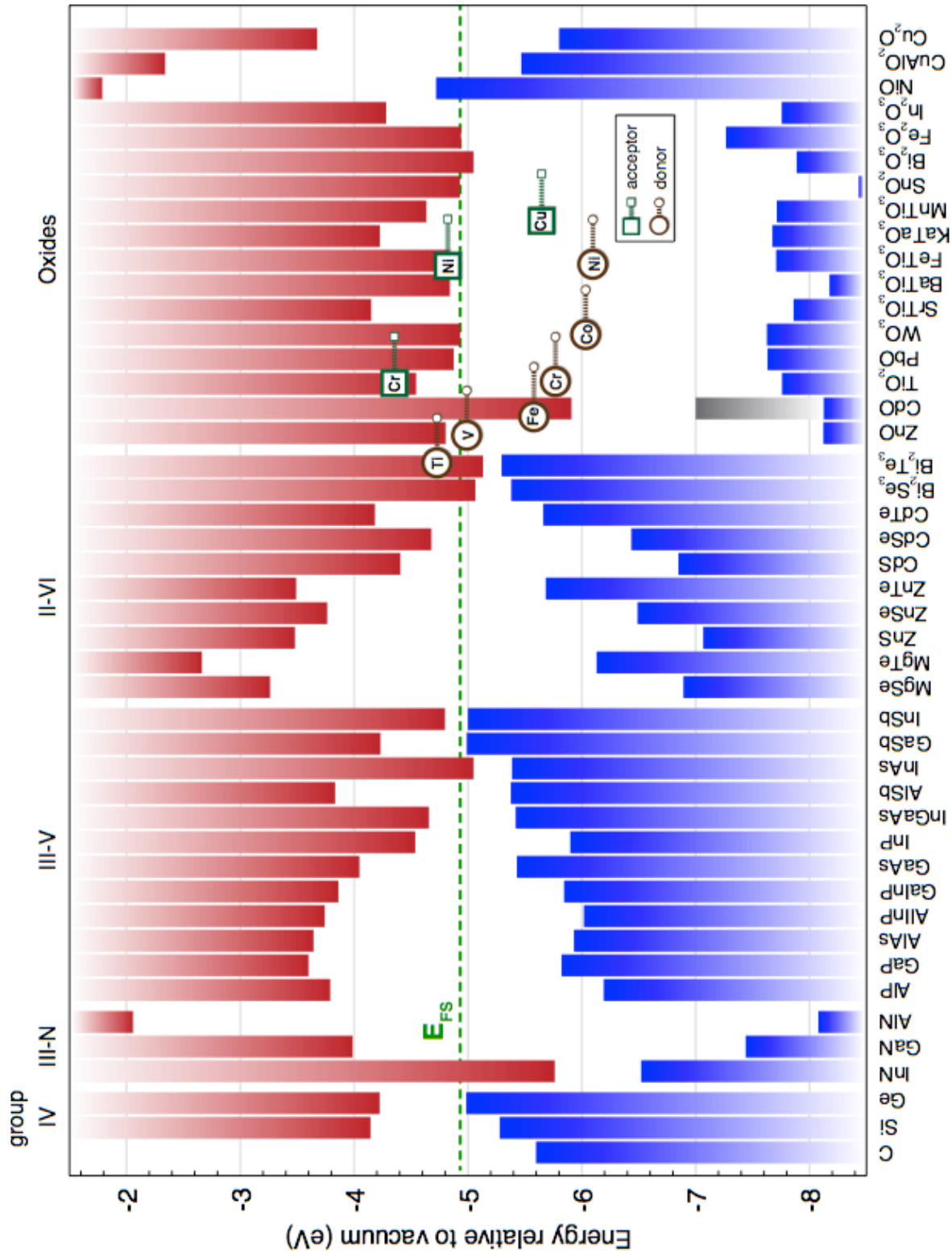

Figure A.2: Band offsets of various semiconductors along with the position of cation d levels. Compiled from Refs. [96]-[99].

References

[1] I. M. Englewood, U. States, and M. H. Crawford, *The Internet of Things: A movement, not a market*.

[2] L. Doman, *EIA projects 28% increase in world energy use by 2040*.

[3] G. E. Moore, "Cramming more components onto integrated circuits, Reprinted from Electronics, volume 38, number 8, April 19, 1965, pp.114 ff.," *IEEE Solid-State Circuits Soc. Newsl.*, vol. 11, no. 3, pp. 33–35.

[4] Y. Wu, *Nanocrystalline Oxide Semiconductors for Dye-Sensitized Solar Cells*. WORLD SCIENTIFIC, 2011, pp. 127–173.

[5] M. Jaroniec, "Silicon beyond the valley," *Nature Chemistry*, vol. 1, no. 2, pp. 166–166, May 2009.

[6] *Copper Indium Gallium Diselenide Solar Cells*.

[7] A. Chirilă, S. Buecheler, F. Pianezzi, P. Bloesch, C. Gretener, A. R. Uhl, C. Fella, L. Kranz, J. Perrenoud, S. Seyrling, R. Verma, S. Nishiwaki, Y. E. Romanyuk, G. Bilger, and A. N. Tiwari, "Highly efficient Cu(In,Ga)Se₂ solar cells grown on flexible polymer films," *Nature Materials*, vol. 10, no. 11, pp. 857–861, Nov. 2011.

[8] L. Vegard, "Die Konstitution der Mischkristalle und die Raumfüllung der Atome," *Zeitschrift für Physik*, vol. 5, no. 1, pp. 17–26, 1921.

[9] L. Nordheim, "Zur Elektronentheorie der Metalle. I," *Annalen der Physik*, vol. 401, no. 5, pp. 607–640, Jan. 1931.

[10] K. M. Yu, S. V. Novikov, R. Broesler, Z. Liliental-Weber, A. X. Levander, V. M. Kao, O. D. Dubon, J. Wu, W. Walukiewicz, and C. T. Foxon, "Low gap amorphous $GaN_{1-x}As_x$ alloys grown on glass substrate," *Appl. Phys. Lett.*, vol. 97, no. 10, p. 101906, Sep. 2010.

[11] K. M. Yu, S. V. Novikov, R. Broesler, I. N. Demchenko, J. D. Denlinger, Z. Liliental-Weber, F. Luckert, R. W. Martin, W. Walukiewicz, and C. T. Foxon, "Highly mismatched crystalline and amorphous $GaN_{1-x}As_x$ alloys in the whole composition range," *Journal of Applied Physics*, vol. 106, no. 10, p. 103709, Nov. 2009.

[12] J. Wu, W. Shan, and W. Walukiewicz, "Band anticrossing in highly mismatched III V semiconductor alloys," *Semiconductor Science and Technology*, vol. 17, no. 8, pp. 860–869, Jul. 2002.

[13] W. Shan, W. Walukiewicz, J. W. Ager, E. E. Haller, J. F. Geisz, D. J. Friedman, J. M. Olson, and S. R. Kurtz, "Band Anticrossing in GaInNAs Alloys," *Phys. Rev. Lett.*, vol. 82, no. 6, pp. 1221–1224, Feb. 1999.

[14] M. Wełna, R. Kudrawiec, Y. N. Semiconductor, and S. Muller, "Effects of a semiconductor matrix on the band anticrossing in dilute group II-VI oxides," *iopscience.iop.org*.

[15] N. Segercrantz, K. M. Yu, M. Ting, W. L. Sarney, S. P. Svensson, S. V. Novikov, C. T. Foxon, and W. Walukiewicz, "Electronic band structure of highly mismatched $GaN_{1-x}Sb_x$ alloys in a broad composition range," *Appl. Phys. Lett.*, vol. 107, no. 14, p. 142104, Oct. 2015.

[16] M. Ting, R. dos Reis, M. Jaquez, O. D. Dubon, S. S. Mao, K. M. Yu, and W. Walukiewicz, "Electronic band structure of ZnO-rich highly mismatched $ZnO_{1-x}Te_x$ alloys," *Appl. Phys. Lett.*, vol. 106, no. 9, p. 092101, Mar. 2015.

[17] M. Ting, K. M. Yu, M. Jaquez, I. D. Sharp, Y. Ye, N. Segercrantz, R. Greif, S. S. Mao, C. P. Liu, and W. Walukiewicz, "ZnO1−xTex highly mismatched alloys beyond the dilute alloy limit: Synthesis and electronic band structure," *Journal of Applied Physics*, vol. 125, no. 15, p. 155702, Apr. 2019.

[18] M. Jaquez, K. M. Yu, M. Ting, M. Hettick, J. F. Sánchez-Royo, M. Wełna, A. Javey, O. D. Dubon, and W. Walukiewicz, "Growth and characterization of $ZnO_{1-x}S_x$ highly mismatched alloys over the entire composition," *Journal of Applied Physics*, vol. 118, no. 21, pp. 215702–8, Dec. 2015.

[19] Y. Zhang, A. Mascarenhas, H. P. Xin, and C. W. Tu, "Scaling of band-gap reduction in heavily nitrogen doped GaAs," *Phys. Rev. B*, vol. 63, no. 16, p. 161303, Apr. 2001.

[20] N. G. Szwacki and P. Bogusławski, "GaAs:N vs GaAs:B alloys: Symmetry-induced effects," *Phys. Rev. B*, vol. 64, no. 16, p. 161201, Sep. 2001.

[21] J. Wu, *Band Anticrossing Effects in Highly Mismatched Semiconductor Alloys*. 2002.

[22] K. Alberi, *Valence Band Anticrossing in Highly Mismatched Alloys*. 2008.

[23] K. Alberi, J. Wu, W. Walukiewicz, K. M. Yu, O. D. Dubon, S. P. Watkins, C. X. Wang, X. Liu, Y. J. Cho, and J. Furdyna, "Valence-band anticrossing in mismatched III-V semiconductor alloys," *Phys. Rev. B*, vol. 75, no. 4, p. 045203, Jan. 2007.

[24] M. A. Mayer, D. T. Speaks, K. M. Yu, S. S. Mao, E. E. Haller, and W. Walukiewicz, "Band structure engineering of $ZnO_{1-x}Se_x$ alloys," *Appl. Phys. Lett.*, vol. 97, no. 2, p. 022104, Jul. 2010.

[25] W. Shan, W. Walukiewicz, J. W. Ager III, K. M. Yu, J. Wu, E. E. Haller, Y. Nabetani, T. Mukawa, Y. Ito, and T. Matsumoto, "Effect of oxygen on the electronic band structure in ZnOxSe1−x alloys," *Appl. Phys. Lett.*, vol. 83, no. 2, pp. 299–301, Jul. 2003.

[26] T. Tanaka, S. Kusaba, T. Mochinaga, K. Saito, Q. Guo, M. Nishio, K. M. Yu, and W. Walukiewicz, "Molecular beam epitaxial growth and optical properties of highly mismatched ZnTe 1−xO xalloys," *Appl. Phys. Lett.*, vol. 100, no. 1, p. 011905, Jan. 2012.

[27] OSHA, "Cadmium." [Online]. Available: https://www.osha.gov/SLTC/cadmium/. [Accessed: 07-Jul-2019].

[28] M. Ravindiran, C. P. R. A. S. Energy, 2018, "Status review and the future prospects of CZTS based solar cell–A novel approach on the device structure and material modeling for CZTS based photovoltaic device," *Vacuum*, vol. 94, pp. 317–329, Oct. 2018.

[29] A. Kojima, K. Teshima, Y. Shirai, and T. Miyasaka, "Organometal Halide Perovskites as Visible-Light Sensitizers for Photovoltaic Cells," *J. Am. Chem. Soc.*, vol. 131, no. 17, pp. 6050–6051, May 2009.

[30] W. S. Yang, B.-W. Park, E. H. Jung, N. J. Jeon, Y. C. Kim, D. U. Lee, S. S. Shin, J. Seo, E. K. Kim, J. H. Noh, and S. I. Seok, "Iodide management in formamidinium-lead-halide–based perovskite layers for efficient solar cells," *Science*, vol. 356, no. 6345, pp. 1376–1379, Jun. 2017.

[31] T. C. Sum and N. Mathews, “Advancements in perovskite solar cells: photophysics behind the photovoltaics,” *Energy Environ. Sci.*, vol. 7, no. 8, pp. 2518–2534, 2014.

[32] H. J. Snaith, “Perovskites: The Emergence of a New Era for Low-Cost, High-Efficiency Solar Cells,” *J. Phys. Chem. Lett.*, vol. 4, no. 21, pp. 3623–3630, Nov. 2013.

[33] H. S. Jung and N. G. Park, “Perovskite Solar Cells: From Materials to Devices,” *Small*, vol. 11, no. 1, pp. 10–25, Oct. 2014.

[34] J. M. Ball and A. Petrozza, “Defects in perovskite-halides and their effects in solar cells,” *Nat. Energy*, vol. 1, no. 11, pp. 16149–13, Oct. 2016.

[35] M. A. Green, A. Ho-Baillie, and H. J. Snaith, “The emergence of perovskite solar cells,” *Nature Photonics*, vol. 8, no. 7, pp. 506–514, Jul. 2014.

[36] T. M. Brenner, D. A. Egger, L. Kronik, G. Hodes, and D. Cahen, “Hybrid organic—inorganic perovskites: low-cost semiconductors with intriguing charge-transport properties,” *Nature Reviews Materials*, vol. 1, no. 1, p. 15007, 2016.

[37] M. D. McCluskey and S. J. Jokela, “Defects in ZnO,” *Journal of Applied Physics*, vol. 106, no. 7, p. 071101, Oct. 2009.

[38] H. L. Pan, T. Yang, B. Yao, R. Deng, R. Y. Sui, L. L. Gao, and D. Z. Shen, “Characterization and properties of ZnO1−xSx alloy films fabricated by radio-frequency magnetron sputtering,” *Applied Surface Science*, vol. 256, no. 14, pp. 4621–4625, 2010.

[39] D. M. Detert, K. B. Tom, C. Battaglia, J. D. Denlinger, S. H. N. Lim, A. Javey, A. Anders, O. D. Dubon, K. M. Yu, and W. Walukiewicz, “Fermi level stabilization and band edge energies in Cd xZn 1−xO alloys,” *Journal of Applied Physics*, vol. 115, no. 23, pp. 233708–7, Jun. 2014.

[40] M. A. Mayer, D. T. Speaks, K. M. Yu, S. S. Mao, E. E. Haller, and W. Walukiewicz, “Band structure engineering of ZnO1−xSex alloys,” *Appl. Phys. Lett.*, vol. 97, no. 2, p. 022104, Jul. 2010.

[41] K. M. Yu, W. Walukiewicz, W. Shan, J. Wu, J. W. Beeman, M. A. Scarpulla, O. D. Dubon, and P. Becla, “Synthesis and optical properties of II-O-VI highly mismatched alloys,” *Journal of Applied Physics*, vol. 95, no. 11, pp. 6232–6238, Jun. 2004.

[42] P. Roy, J. R. Ota, and S. K. Srivastava, “Crystalline ZnS thin films by chemical bath deposition method and its characterization,” *Thin Solid Films*, vol. 515, no. 4, pp. 1912–1917, 2006.

[43] X. F. Fan, Z. X. Shen, Y. M. Lu, and J.-L. Kuo, “A theoretical study of thermal stability and electronic properties of wurtzite and zincblende ZnO xS 1− x,” *New Journal of Physics*, vol. 11, no. 9, p. 093008, Sep. 2009.

[44] B. K. Meyer, A. Polity, B. Farangis, Y. He, D. Hasselkamp, T. Krämer, and C. Wang, “Structural properties and bandgap bowing of ZnO1−xSx thin films deposited by reactive sputtering,” *Appl. Phys. Lett.*, vol. 85, no. 21, pp. 4929–4931, Nov. 2004.

[45] T. Minemoto, A. Okamoto, and H. Takakura, “Sputtered ZnO-based buffer layer for band offset control in Cu(In,Ga)Se2 solar cells,” *Thin Solid Films*, vol. 519, no. 21, pp. 7568–7571, Aug. 2011.

[46] A. Okamoto, T. Minemoto, and H. Takakura, "Application of Sputtered ZnO1-xSx Buffer Layers for Cu(In,Ga)Se2 Solar Cells," *Jpn. J. Appl. Phys.*, vol. 50, no. 4, p. 04DP10, Apr. 2011.

[47] S. Sharbati, J. S. I. J. O. photovoltaics, 2014, "Impact of the Band Offset for n-Zn(O,S)/p-Cu(In,Ga)Se Solar Cells," *ieeexplore.ieee.org*.

[48] Y. Z. Yoo, Z.-W. Jin, T. Chikyow, T. Fukumura, M. Kawasaki, and H. Koinuma, "S doping in ZnO film by supplying ZnS species with pulsed-laser-deposition method," *Appl. Phys. Lett.*, vol. 81, no. 20, pp. 3798–3800, Nov. 2002.

[49] C. Persson, C. Platzer-Björkman, J. Malmström, T. Törndahl, and M. Edoff, "Strong Valence-Band Offset Bowing of $ZnO_{1-x}S_x$ Enchances *p*-Type Nitrogen Doping of ZnO-like Alloys," *Physical Review Letters*, vol. 97, no. 14, p. 146403, Oct. 2006.

[50] M. Kriisa, R. Sáez-Araoz, C.-H. Fischer, T. Köhler, E. Kärber, Y. Fu, F. Hergert, M. C. Lux-Steiner, and M. Krunks, "Study of Zn(O,S) films grown by aerosol assisted chemical vapour deposition and their application as buffer layers in Cu(In,Ga)(S,Se)2 solar cells," *Solar Energy*, vol. 115, pp. 562–568, 2015.

[51] M. Ohring, *Materials Science of Thin Films*. Academic Press, 2002.

[52] D. B. Chrisey and G. K. Hubler, *Pulsed Laser Deposition of Thin Films*. Wiley-Interscience, 1994.

[53] K. Ramanathan, J. Mann, S. G. 2. 3. IEEE, and Z.-C. Feng, "A comparative study of Zn (O, S) buffer layers and CIGS solar cells fabricated by CBD, ALD, and sputtering," *ieeexplore.ieee.org*.

[54] R. Broesler, E. E. Haller, W. Walukiewicz, T. Muranaka, T. Matsumoto, and Y. Nabetani, "Temperature dependence of the band gap of ZnSe1−xOx," *Appl. Phys. Lett.*, vol. 95, no. 15, p. 151907, Oct. 2009.

[55] M. Welna, R. Kudrawiec, Y. Nabetani, and W. Walukiewicz, "Band anticrossing in ZnOSe highly mismatched alloy," *Appl. Phys. Express*, vol. 7, no. 7, p. 071202, Jul. 2014.

[56] D. Aspnes, "Third-derivative modulation spectroscopy with low-field electroreflectance," *surface science*, vol. 37, pp. 418–442, Jun. 1973.

[57] P. Swift, "Adventitious carbon—the panacea for energy referencing?," *Surface and Interface Analysis*, vol. 4, no. 2, pp. 47–51, Apr. 1982.

[58] M. A. Green, Y. Hishikawa, E. Dunlop, D. H. Levi, J. Hohl-Ebinger, M. Yoshita, and A. W. Y. Ho-Baillie, "Solar cell efficiency tables (version 53)," *Prog Photovolt Res Appl.*, no. 27, pp. 3–12, 2019.

[59] H. Amano, Y. Baines, E. Beam, M. Borga, T. Bouchet, P. R. Chalker, M. Charles, K. J. Chen, N. Chowdhury, R. Chu, C. De Santi, M. M. De Souza, S. Decoutere, L. Di Cioccio, B. Eckardt, T. Egawa, P. Fay, J. J. Freedsman, L. Guido, O. Häberlen, G. Haynes, T. Heckel, D. Hemakumara, P. Houston, J. Hu, M. Hua, Q. Huang, A. Huang, S. Jiang, H. Kawai, D. Kinzer, M. Kuball, A. Kumar, K. B. Lee, X. Li, D. Marcon, M. März, R. McCarthy, G. Meneghesso, M. Meneghini, E. Morvan, A. Nakajima, E. M. S. Narayanan, S. Oliver, T. Palacios, D. Piedra, M. Plissonnier, R. Reddy, M. Sun, I. Thayne, A. Torres, N. Trivellin, V. Unni, M. J. Uren, M. Van Hove, D. J. Wallis, J. Wang, J. Xie, S. Yagi, S. Yang, C. Youtsey, R. Yu, E. Zanoni, S. Zeltner, and Y. Zhang, "The 2018 GaN power electronics roadmap," *Journal of Physics D: Applied Physics*, vol. 51, no. 16, p. 163001, Apr. 2018.

[60] S. J. Pearton, J. Yang, P. H. Cary IV, F. Ren, J. Kim, M. J. Tadjer, and M. A. Mastro, "A review of Ga_2O_3 materials, processing, and devices," *Applied Physics Reviews*, vol. 5, no. 1, pp. 011301–57, Mar. 2018.

[61] M. Higashiwaki and G. H. Jessen, "Guest Editorial: The dawn of gallium oxide microelectronics," *Appl. Phys. Lett.*, vol. 112, no. 6, p. 060401, Feb. 2018.

[62] S. J. Pearton, F. Ren, M. Tadjer, and J. Kim, "Perspective: Ga_2O_3 for ultra-high power rectifiers and MOSFETS," *Journal of Applied Physics*, vol. 124, no. 22, p. 220901, Dec. 2018.

[63] J. Y. Tsao, S. Chowdhury, M. A. Hollis, D. Jena, N. M. Johnson, K. A. Jones, R. J. Kaplar, S. Rajan, C. G. Van de Walle, E. Bellotti, C. L. Chua, R. Collazo, M. E. Coltrin, J. A. Cooper, K. R. Evans, S. Graham, T. A. Grotjohn, E. R. Heller, M. Higashiwaki, M. S. Islam, P. W. Juodawlkis, M. A. Khan, A. D. Koehler, J. H. Leach, U. K. Mishra, R. J. Nemanich, R. C. N. P. Podgurski, J. B. Shealy, Z. Sitar, M. J. Tadjer, A. F. Witulski, M. Wraback, and J. A. Simmons, "Ultrawide-Bandgap Semiconductors: Research Opportunities and Challenges," *Adv. Electron. Mater.*, vol. 4, no. 1, p. 1600501, Jan. 2018.

[64] M. Orita, H. Hiramatsu, H. Ohta, and M. Hirano, "Preparation of highly conductive, deep ultraviolet transparent β-Ga_2O_3 thin film at low deposition temperatures," *Thin Solid Films*, vol. 411, pp. 134–139, May 2002.

[65] T. Onuma, S. Saito, K. Sasaki, T. Masui, S. Muller, T. Honda, and M. Higashiwaki, "Valence band ordering in β-Ga_2O_3 studied by polarized transmittance and reflectance spectroscopy," *Jpn. J. Appl. Phys.*, no. 54, p. 112601, 2015.

[66] F. B. Zhang, K. Saito, T. Tanaka, M. Nishio, Q. X. Guo, 2014, "Structural and optical properties of Ga_2O_3 films on sapphire substrates by pulsed laser deposition," *Journal of Crystal Growth*, vol. 387, pp. 96–100, Feb. 2014.

[67] R. J. Kaplar, A. A. Allerman, A. Armstrong, M. H. Crawford, J. R. Dickerson, A. J. Fischer, A. G. Baca, and E. A. Douglas, "Ultra-wide-bandgap AlGaN power electronic devices," *ECS J. Solid State Sci. Technol.*, vol. 2, no. 6, pp. Q3061–G3066, 2017.

[68] S. Nakagomi, Y. Kokubun, and Z.-C. Feng, "Crystal orientation of β-Ga_2O_3 thin films formed on c-plane and a-plane sapphire substrate," *Journal of Crystal Growth*, vol. 349, no. 1, pp. 12–18, Jun. 2012.

[69] J. B. Varley, J. R. Weber, A. Janotti, and C. G. Van de Walle, "Oxygen vacancies and donor impurities in β-Ga_2O_3," *Appl. Phys. Lett.*, vol. 97, no. 14, p. 142106, Oct. 2010.

[70] B. J. Baliga, "Gallium nitride devices for power electronic applications," *Semiconductor Science and Technology*, no. 28, p. 074011, 2013.

[71] K. Sasaki, M. Higashiwaki, A. Kuramata, T. Masui, and S. Yamakoshi, "MBE grown Ga_2O_3 and its power device applications," *Journal of Crystal Growth*, no. 378, pp. 591–595.

[72] G. Wagner, M. Baldini, D. Gogova, M. Schmidbauer, R. Schewski, M. Albrecht, Z. Galazka, D. Klimm, and R. Fornari, "Homoepitaxial growth of β-Ga_2O_3 layers by metal-organic vapor phase epitaxy," *Phys. Status Solidi A*, vol. 211, no. 1, pp. 27–33, Oct. 2013.

[73] Y. Lv, J. Ma, W. Mi, C. Luan, Z. Zhu, and H. Xiao, "Characterization of β-Ga_2O_3 thin films on sapphire (0001) using metal-organic chemical vapor deposition technique," *Vacuum*, vol. 86, no. 12, pp. 1850–1854, Jul. 2012.

[74] F. Mezzadri, G. Calestani, F. Boschi, D. Delmonte, M. Bosi, and R. Fornari, "Crystal Structure and Ferroelectric Properties of ε-Ga_2O_3 Films Grown on (0001)-Sapphire," *Inorg. Chem.*, vol. 55, no. 22, pp. 12079–12084, Nov. 2016.

[75] M. Orita, H. Ohta, M. Hirano, and H. Hosono, "Deep-ultraviolet transparent conductive β-Ga_2O_3 thin films," *Appl. Phys. Lett.*, vol. 77, no. 25, pp. 4166–4168, Dec. 2000.

[76] R. Wakabayashi, T. Oshima, M. Hattori, K. Sasaki, T. Masui, A. Kuramata, S. Yamakoshi, K. Yoshimatsu, and A. Ohtomo, "Oxygen-radical-assisted pulsed-laser deposition of β-Ga_2O_3 and β-$(Al_xGa_{1-x})_2O_3$ films," *Journal of Crystal Growth*, vol. 424, no. C, pp. 77–79, Aug. 2015.

[77] K. D. Leedy, K. D. Chabak, V. Vasilyev, D. C. Look, J. J. Boeckl, J. L. Brown, S. E. Tetlak, A. J. Green, N. A. Moser, A. Crespo, D. B. Thomson, R. C. Fitch, J. P. McCandless, and G. H. Jessen, "Highly conductive homoepitaxial Si-doped Ga_2O_3 films on (010) β-Ga_2O_3 by pulsed laser deposition," *Appl. Phys. Lett.*, vol. 111, no. 1, pp. 012103–5, Jul. 2017.

[78] S.-A. Lee, J.-Y. Hwang, J.-P. Kim, S.-Y. Jeong, and C.-R. Cho, "Dielectric characterization of transparent epitaxial Ga_2O_3 thin film on n-GaN⁄Al_2O_3 prepared by pulsed laser deposition," *Appl. Phys. Lett.*, vol. 89, no. 18, p. 182906, Nov. 2006.

[79] E. G. Víllora, K. Shimamura, K. Kitamura, and K. Aoki, "Rf-plasma-assisted molecular-beam epitaxy of β-Ga_2O_3," *Appl. Phys. Lett.*, vol. 88, no. 3, pp. 031105–4, Jan. 2006.

[80] T. Oshima, T. Okuno, and S. Fujita, "Ga_2O_3 Thin Film Growth on c-Plane Sapphire Substrates by Molecular Beam Epitaxy for Deep-Ultraviolet Photodetectors," *Jpn. J. Appl. Phys.*, vol. 46, no. 11, pp. 7217–7220, Nov. 2007.

[81] K. Sasaki, A. Kuramata, T. Masui, E. G. Víllora, K. Shimamura, and S. Yamakoshi, "Device-Quality β-Ga_2O_3 Epitaxial Films Fabricated by Ozone Molecular Beam Epitaxy," *Appl. Phys. Express*, vol. 5, no. 3, pp. 035502–4, Feb. 2012.

[82] S. W. Kaun, F. Wu, and J. S. Speck, "β-$(Al_xGa_{1-x})_2O_3$/Ga_2O_3 (010) heterostructures grown on β-Ga_2O_3 (010) substrates by plasma-assisted molecular beam epitaxy," *Journal of Vacuum Science & Technology A: Vacuum, Surfaces, and Films*, vol. 33, no. 4, pp. 041508–10, Jul. 2015.

[83] P. Vogt and O. Bierwagen, "Reaction kinetics and growth window for plasma-assisted molecular beam epitaxy of Ga_2O_3: Incorporation of Ga vs. Ga_2O desorption," *Appl. Phys. Lett.*, vol. 108, no. 7, pp. 072101–5, Feb. 2016.

[84] S. J. Pearton, J. Yang, P. H. Cary, F. Ren, J. Kim, M. J. Tadjer, and M. A. Mastro, "A review of Ga2O3 materials, processing, and devices," *Applied Physics Reviews*, vol. 5, no. 1, p. 011301, Mar. 2018.

[85] M. J. Tadjer, J. L. Lyons, N. Nepal, J. Jaime A Freitas, A. D. Koehler, and G. M. Foster, "Editors' Choice—Review—Theory and Characterization of Doping and Defects in β-Ga2O3," *ECS J. Solid State Sci. Technol.*, vol. 8, no. 7, pp. Q3187–Q3194, Jan. 2019.

[86] F. Zhang, K. Saito, T. Tanaka, M. Nishio, M. Arita, and Q. Guo, "Wide bandgap engineering of $(AlGa)_2O_3$ films," *Appl. Phys. Lett.*, vol. 105, no. 16, p. 162107, Oct. 2014.

[87] H. Okumura, Y. Kato, T. Oshima, and T. Palacios, "Demonstration of lateral field-effect transistors using Sn-doped β-$(AlGa)_2O_3$ (010)," *Jpn. J. Appl. Phys.*, no. 58, p. SBBD12, Apr. 2019.

[88] J. R. Weber, D. Steiauf, J. B. Varley, A. Janotti, and C. G. Van de Walle, "$(In_xGa_{1-x})_2O_3$ alloys for transparent electronics," *Phys. Rev. B*, no. 92, p. 085206, 2015.

[89] H. Von Wenckstern, D. Splith, A. Werner, S. Muller, and M. Grundmann, "Properties of Schottky Barrier Diodes on $(In_xGa_{1-x})_2O_3$ for $0.01 \leq x \leq 0.85$ Determined by a Combinatorial Approach," *ACS Combinatorial Science*, vol. 17, no. 12, pp. 710–715, Dec. 2015.

[90] A. M. Diamond, L. Corbellini, K. R. Balasubramaniam, S. Chen, S. Wang, T. S. Matthews, L.-W. Wang, R. Ramesh, and J. W. Ager, "Copper-alloyed ZnS as a p-type transparent conducting material," *Phys. Status Solidi A*, vol. 209, no. 11, pp. 2101–2107, Aug. 2012.

[91] J. E. Peralta, J. Heyd, G. E. Scuseria, and R. L. Martin, "Spin-orbit splittings and energy band gaps calculated with the Heyd-Scuseria-Ernzerhof screened hybrid functional," *Phys. Rev. B*, vol. 74, no. 7, p. 073101, Aug. 2006.

[92] W. Wei, Z. Qin, S. Fan, Z. Li, K. Shi, Q. Zhu, and G. Zhang, "Valence band offset of β-Ga_2O_3/wurtzite GaN heterostructure measured by X-ray photoelectron spectroscopy," *Nanoscale Research Letters*, vol. 7, no. 1, p. 562, 2012.

[93] S. E. Al Garni and A. F. Qasrawi, "Design and Characterization of the Ge/Ga_2S_3 Heterojunction," *Journal of Elec Materi*, vol. 46, no. 8, pp. 4848–4856, Mar. 2017.

[94] W. Walukiewicz, "Amphoteric native defects in semiconductors," *Appl. Phys. Lett.*, vol. 54, no. 21, pp. 2094–2096, Dec. 1998.

[95] K. M. Yu, W. Walukiewicz, W. Shan, J. W. I. Ager, J. Wu, E. E. Haller, J. F. Geisz, D. J. Friedman, and J. M. Olson, "Nitrogen-induced increase of the maximum electron concentration in group III-N-V alloys," *Physical Review B (Condensed Matter and Materials Physics)*, vol. 61, no. 2, pp. R13337–R13340, May 2000.

[96] D. T. Speaks, M. A. Mayer, K. M. Yu, S. S. Mao, E. E. Haller, and W. Walukiewicz, "Fermi level stabilization energy in cadmium oxide," *Journal of Applied Physics*, vol. 107, no. 11, p. 113706, Jun. 2010.

[97] W. Walukiewicz, "Intrinsic limitations to the doping of wide-gap semiconductors," *Physica B: Physics of Condensed Matter*, vol. 302, pp. 123–134, Jan. 2001.

[98] C. J. Vesely and D. W. Langer, "Electronic Core Levels of the II*B*-VI*A* Compounds," *Phys. Rev. B*, vol. 4, no. 2, pp. 451–462, Jul. 1971.

[99] S. X. Li, K. M. Yu, J. Wu, R. E. Jones, W. Walukiewicz, I. J W Ager, W. Shan, E. E. Haller, H. Lu, and W. J. Schaff, "Fermi-level stabilization energy in group III nitrides," *Phys. Rev. B*, vol. 71, no. 16, p. 161201, Apr. 2005.